Lab on a Chip Rare Cell Isolation Platform with Dielectrophoretic Smart Sample Focusing, Automated Whole Cell Tracking Analysis Script, and a Bioinspired On-chip Electroactive Polymer Micropump

Lisa Mae Anders

Thesis submitted to the faculty of the Virginia Polytechnic Institute and State University in partial fulfillment of the requirements for the degree of

Master of Science

In

Electrical Engineering

Rafael V. Davalos

Devi Parikh

Eva M. Schmelz

Chris L. Wyatt

June 19, 2014

Blacksburg, VA

Keywords: Dielectrophoresis, Contactless Dielectrophoresis, Lab on a Chip, Sample Enrichment, Tumor Initiating Cells

Lab on a Chip Rare Cell Isolation Platform with Dielectrophoretic Smart Sample Focusing, Automated Whole Cell Tracking Analysis Script, and a Bioinspired On-chip Electroactive Polymer Micropump

Lisa Mae Anders

Abstract

Dielectrophoresis (DEP), an electrokinetic force, is the motion of a polarizable particle in a non-uniform electric field. Contactless DEP (cDEP) is a recently developed cell sorting and isolation technique that uses the DEP force by capacitavely coupling the electrodes across the channel. The cDEP platform sorts cells based on intrinsic biophysical properties, is inexpensive, maintains a sterile environment by using disposable chips, is a rapid process with minimal sample preparation, and allows for immediate downstream recovery. This platform is highly competitive compared to other cell sorting techniques and is one of the only platforms to sort cells based on phenotype, allowing for the isolation of unique cell populations not possible in other systems.

The original purpose of this work was to determine differences in the bioelectrical fingerprint between several critical cancer types. Results demonstrate a difference between Tumor Initiating Cells, Multiple Drug Resistant Cells, and their bulk populations for experiments conducted on three prostate cancer cell lines and treated and untreated MOSE cells. However, three significant issues confounded these experiments and challenged the use of the cDEP platform. The purpose of this work then became the development of solutions to these barriers and presenting a more commercializable cDEP platform.

An improved analysis script was first developed that performs whole cell detection and cell tracking with an accuracy of 93.5%. Second, a loading system for doing smart sample handling, specifically cell focusing, was developed using a new in-house system and validated. Experimental results validated the model and showed that cells were successfully focused into a tight band in the middle of the channel. Finally, a proof of concept for an on-chip micropump is presented and achieved 4.5% in-plane deformation. When bonded over a microchannel, fluid flow was induced and measured.

These solutions present a stronger, more versatile cDEP platform and make for a more competitive commercial product. However, these solutions are not just limited to the cDEP platform and may be applicable to multitudes of other microfluidic devices and applications.

Acknowledgements

"I am, and ever will be, a white-socks, pocket-protector, nerdy engineer, born under the second law of thermodynamics, steeped in steam tables, in love with free-body diagrams, transformed by Laplace and propelled by compressible flow." – *Neil Armstrong*

My acknowledgements begin back in 2009 when I first visited Dr. Davalos' lab as part of the Bioinformatics and Biomedical Summer Institute REU program as an undergraduate student and was mentored by Paulo Garcia and Mike Sano. They inspired me to continue on this path and apply to graduate school and ultimately end up back in Dr. Davalos' lab. Their guidance and mentorship continues to inspire me.

I need to thank Dr. Davalos for making me a part of his lab, twice now, and his unfaltering support and motivating advice. It has been my privilege to be a part of the BioElectroMechanical systems laboratory and I want to thank each and every member of the BEMS lab that I have had the pleasure of working with and interacting with. In particular I want to thank Elizabeth Elvington for taking me under her wing and teaching me the fundamentals of scientific research and being a graduate student, Mohammad Bonakdar for sharing his expertise in fabrication systems, and Jaka Cemazar for his invaluable mentorship and guidance.

I want to thank my MultiSTEPS crew especially Andrea, Adwoa, Ray, Renee, and Dan for sharing their senses of humor while thriving in this interdisciplinary program.

My undergraduate students, Kruthika and Philip, are two of the most enthusiastic and hard-working people I have ever met. It has been an honor to mentor you and be inspired by you both and I look forward to following your great achievements.

Collaboration is the cornerstone of research and I have had the pleasure of working with many extraordinary people. Special thanks to Adwoa for help in acquiring SEM images, Vivek Jayabalan and Sai Ma for our work quantifying the performance of 3D printed master molds, Jaka and Dr. Cramer's lab for collaborating on the prostate cancer cell line experiments, Kru, Behrouz, Dr. Socha, and Dr. Holmes for collaborating on the micropump project, Philip, Dr. Schmelz, and Dr. Roberts for collaborating on the MOSE project, and Dr. Parikh for collaborating on the development of analysis software.

To my family I want to express my deepest gratitude. I want to thank my brother for encouraging me to be spontaneous and embrace adventure in life. To my mom I want to express my gratitude for her never ending support, unconditional love, and patience. I want to thank my dad for being my engineering inspiration and role model.

Finally I want to thank Kristoffer Dixon for going on this 4,500 mile journey with me and supporting me through the good times and the stressful times. I would not have been able to do this without you and I can't wait to see what the future has in store for us!

Table of Contents

Table of Figures

List of Tables

List of Abbreviations

Carbon Black (CB)

Contactless Dielectrophoresis (cDEP)

Claussius-Mosotti Factor (CM)

Circulating Tumor Cells (CTC's)

Dielectric Elastomer (DE)

Dielectrophoresis (DEP)

Electric field (E)

Lab on a Chip (LOC)

Multiple Drug Resistance (MDR)

Negative Dielectrophoresis (nDEP)

Positive Dielectrophoresis (pDEP)

Reynolds number (Re)

Tumor Initiating Cells (TIC's)

Chapter 1: Introduction

1.1 Cancer

1.1.1 Cancer Background

A recent development in the understanding of cancer tumorigenesis and how cancer is different from normal cell progression was the establishment of the hallmarks of cancer [1, 2]. Cancer cells are able to sustain proliferative signaling. In addition cancer cells are capable of evading growth suppressors that would limit normal cells. Cell to cell contact is different where cancer cells are not regulated by contact inhibition whereas normal, healthy, cells are limited in growth by their surrounding neighbors. Recent work on studying the proliferative ability of cancer cells has revealed the activation of the epithelial-to-mesenchymal transition which has been associated with high-grade malignancy traits [3-6]. Cancer cells resist apoptosis, the otherwise natural barrier to cancer development. Cancer cells essentially achieve replicative immortality in order to generate macroscopic tumors. Cancer cells have also been shown to develop their own vasculature, called angiogenesis, in order to sustain its expanding growths. Cancer cells also undergo what is referred to as the invasion-metastasis cascade which is a series of cell-biologic changes to reach full metastatic ability [7] [1, 2].

Metastasis is when cancer cells break away from the bulk of the tumor and are shed into the surrounding tumor to propagate. Once reaching the blood stream of lymphatic vessels the cancer cells are able to reach other areas of the body and grow in other tissues. Metastasis is considered to be the cause of most cancer related deaths [8].

Cancer is a challenging disease to treat due to the variety of ways in which it can abnormally develop [9]. For example brain cancer will typically present itself as cells that resemble neurons and glia [10] and teratocarcinomas will often resemble cartilage and bone [11]. The parallels between somatic stem cells and cancer cells, their ability to self-renew and differentiate, gave rise to the concepts of cancer stem cells and improving cancer treatment by applying concepts learned from stem cell research [11].

1.1.2 Cancer's Impact

Cancer is the second most common cause of death in the United States accounting for one out of every four deaths. In 2007, according to the World Health Organization (WHO), 24.6 million people were diagnosed with cancer and 7.9 million of those died due to cancer. In 2008 the overall healthcare cost due to cancer was 228.1 billion dollars based on the American Cancer Society's (ACS) Facts and Figures. Projections show that the number of diagnoses and the number of deaths will increase with 12 million people dying due to cancer in 2030. In order to reduce the impact that this disease has on society developing methods for early detection and targeted treatment is critical. It has been estimated that if all cancers were detected and treated in early that one third of all cancer cases could be cured. This demonstrates the importance of early detection in improving patient prognosis.

Epithelial ovarian cancer is the leading cause of death from gynecological malignancies in the world. 125,226 women worldwide are diagnosed and 75,724 die annually. The high mortality rate can be attributed to a lack of routine screening methods and subsequent late detection. The 5 year survival rate for those diagnosed with ovarian cancer drops dramatically from over 90% if caught at an early stage down to under 30% at a late stage. It is worth noting that only 20% of ovarian cancer cases are diagnosed at an early stage.

Prostate cancer is the most commonly cancer detected in men with 238,590 new cases estimated to have been detected in 2013 which accounts for 28% of all detected cancers detected in men. It is the second most common cause of death due to cancer in men with 29,720 estimated deaths in 2013 which accounts for 10% of all deaths due to cancer in men [12].

1.1.3 Tumor Initiating Cells, Circulating Tumor Cells, and Multidrug Resistance

There are three cell groups that are thought to be the most dangerous and are responsible for the bulk of a cancer's tumorigenicity. Methods for isolating these three types of cells are critical to develop in order to research targeted treatments. The three types, discussed below, are Tumor Initiating Cells (TIC's), Circulating Tumor Cells (CTC's), and multidrug resistant cancer cells.

The first of these three types are Cancer Stem Cells (CSC's) or Tumor Initiating Cells (TIC'S). They are a subpopulation of cancer cells that have unregulated self-renewal [13]. They are referred to as TIC's due to their ability for one cell to transplant an entirely new tumor [14] and CSC's because of their stem-like properties and ability to differentiate. They are thought to be putatively responsible for the metastatic potential of tumors. Treatments targeting these cells are critical for improving cancer diagnostic prognosis. In order to develop targeted treatments methods for isolating this cell population must be developed. A major critical issue in current cancer treatment methods is that a fraction of malignant cells survive chemotherapy and radiation. There is evidence suggesting that these surviving cells possess tumor initiating capabilities responsible for their therapeutic resistance [15]. Normal stem cells and cancer cells possess similar attributes that suggest a common origin (reviewed in [14]). Like normal stem cells, cancer cells possess self-renewal capabilities. Additionally, some data suggest that the bulk of a tumor is generated from a finite number of cells that possess extended replicative capacity. Some of the crucial biological applications of TICs include development of animal models of carcinogenesis and understanding metastasis and other key biological processes [15]. Literature suggests that such TIC cells are capable of surviving chemotherapy and contribute to recurrent disease [16].

Tumor cells that are spontaneously circulating throughout the body are referred to as Circulating Tumor Cells (CTC's) and is considered to be a hallmark of cancer's invasive behavior [17]. Detection is challenging due to the high degree of sensitivity required, in early stages there can be as little as a few CTC cells per 10mL of blood. Some diagnostic techniques have reached the market however they are time intensive requiring centrifugation steps. However studies conducted measuring the level of CTC's in human trials have shown that the level of CTC's can predict survival [18] [19] [20]. Fast, cheap, and highly sensitive diagnostic tests for doing CTC level detection will be crucial to determining the invasive properties of cancer.

The final group of cancer cells that will be addressed in this work are multidrug resistant cancer cells (MDR). The current most effective treatment of metastatic cancers is chemotherapy. Some portion of a cancer tumor can gain a resistance to anticancer drugs. This can be due to a number of factors, most commonly cited are variations in chemical absorption and differences in cellular metabolism [21]. There are three main mechanisms through which a cancer cell might gain multidrug resistance. Namely, (1) decreased uptake of water-soluble chemicals, which decreases uptake of drugs reliant upon transporters to enter the cell such as the commonly used chemotherapeutic drug cisplatin, (2) changes in the cell such as cell cycle changes, better repair of DNA damage, metabolism changes, and reduced apoptosis that will reduce the ability of cytotoxic drugs to target the cell, and (3) increased efflux of hydrophobic cytotoxic drugs that otherwise could easily enter the cells by diffusion across the plasma membrane [21]. It is inarguable that MDR accounts for a significant number of cancer treatment failures [22].

New, inexpensive, diagnostic tests that screen for TIC's, CTC's, and MDR are critical to develop in order to catch cancer in its earliest stages and move towards personalized treatment plans. This will drastically improve patient outcomes.

1.2 Limitations of Mainstream Techniques for Cell Isolation and Characterization

Isolating these cells to discover treatment pathways for targeted ablation is critical however current techniques rely on superficial means of tagging cells, such as using markers.

Current techniques for characterizing, selecting, or purifying cell populations are flow cytometry or magnetic bead coupling. Both techniques are labor intensive, require specialized training and resources, and involve irreversibly altering the surface of the cell thus changing its properties [23]. These techniques use surface markers which rely on association with expression of proteins in a cell population. These techniques have been shown to have serious limitations with efficacy [24]. The attachment of the probes to the target cells can also influence cell behavior, possibly having dramatic effects on long term studies [25].

In addition to markers being based on bonding to external proteins rather than being a true measure of intrinsic cell properties for many of the popular and widely used markers there is controversy over whether or not they even are good at isolating a subpopulation of cells. The ALDH marker is one example of this where, despite being widely used for CSC isolation, [24] found there to be no link between ALDH and CSC but instead with more tumorigenic cells.

Another way of isolating TIC's is to culture them in a specific environment , as demonstrated in [26]. This technique is much better at isolating a subpopulation of cells thought to be CSC's. However it is very time consuming as you must culture several generations of a cell line in order to obtain a pure sample.

Current methods for isolation or enrichment of TIC's base on intrinsic characteristics [27-29] haven't been able to achieve a rapid process and high throughput output that is good enough for clinical studies. To date there is no existing technique capable of fast and efficient isolation of CSC's.

1.3 Dielectrophoresis

1.3.1 Early Development of Dielectrophoresis

Dielectrophoresis (DEP) is the motion of a dielectric, or polarizable, particle in an electric field. It was first described in 1951by Pohl and Hawk, used in 1966 to sort live and dead cell, and the theory was published in Pohl's book in 1978 [30]. It is a technique that uses a non-uniform electric field to induce motion of a polarizable particle in a suspending mixture, allowing for characterization.

A neutral particle, when placed in an electric field, will polarize and a dipole will form. In a uniform electric field the particle will remain suspended in its original location. In a non-uniform field the force will be uneven due to the unbalanced electrostatic forces at each pole of the particle [31, 32]. The particle, then, will be experience a force in a particular direction either towards or away from areas of dense electric field gradients.

The direction of the force the particle experiences is dependent upon the Claussius-Mossotti (CM) factor. [33, 34]. The CM factor essentially is an expression of the ratio of the conductivity of the particle to the conductivity of the surrounding medium. When the CM factor is positive the particle experiences what is referred to as a positive DEP force toward regions of high electric field intensity. When the CM factor is negative the particle experiences a DEP force away from areas of high electric field intensity or towards areas with low electric field intensity. When the CM factor is zero the particle will experience an even force in both directions and the particle will experience no net force and therefore no movement. Essentially this can be explained as the path that the electric field follows through the chamber – when the particles are more conductive than the medium the electric field will penetrate the particles whereas when the particles are less conductive than the surrounding medium they will essentially act as insulators in the system and the electric field will go around them.

The most crucial components, then, to induce the DEP force are the electrode geometry and the conductivity of the suspending fluid. In early experiments needles were used to create the non-uniform electric field [35]. Since then the electrodes in traditional DEP devices are created by patterning metal on glass or Pyrex. Typically these electrodes are based on an array of thin-film interdigitated electrodes and either a glass or polymer cover is placed over the electrodes to act as the chamber through which the sample is passed [36] [37].

Dielectrophoresis includes many different electrode configurations in addition to the traditional interdigitated design. This includes travelling wave DEP where the force is created by a dipole lag in a travelling electric field [38, 39], electrorotation where quadropole electrodes are used to induce the DEP force by rotating the electric field [40-42], pearl chaining where dipole-dipole interactions between particles cause them to chain together [43-47], field flow fractionation where the balance between gravity and the DEP force is used to separate cells [48], and insulating DEP where insulating obstacles in the sample channel create the non-uniform electric field [49] [50-54]. Traditional DEP has been shown to be effective at isolating and characterizing cells, detecting pathogens, and even manipulating viruses and macromolecules [46, 55-62]. Because it has been shown that DEP concentrates and differentiates cells based on their intrinsic properties such as size, shape, internal structure, conductivity, and polarizability and it leaves no effects or residues on a sample it is considered to be an efficient and non-invasive technique with a lot of promise [33, 34].

DEP has also been applied to conducting stem cell studies both for characterizing normal stem cells and investigating TIC's. Differentiation in neural stem cell populations has been predicted using DEP even before antigens could be used [63] and preliminary work into isolating and characterizing TIC's has been published [25, 63-66].

Traditional DEP devices, where the electrode is printed in metal on a glass or Pyrex substrate, have several main drawbacks. They are susceptible to electrode fouling and delamination and require expensive and elaborate fabrication procedures [35]. As the sample is not isolated from the electrodes biological cross contamination is a problem and devices can be difficult to sterilize due to encapsulation. The electronics, as they are located in a single plane on the bottom of the device, limit the range of the electrode field which makes high throughput very difficult. Sample volumes are typically in the nL range which is much lower than the mL required for clinical studies.

1.3.2 Foundations of Contactless Dielectrophoresis

Lately the technique of DEP has experienced a boom due to the development of inexpensive fabrication techniques. One such recent development has been contactless Dielectrophoresis (cDEP) [67]. The electrodes are separated from the channel by a thin insulating membrane which acts to capacitatively couple the electric field with the channel. Removing contact between the sample and the electrodes allows the sample to remain sterile for culturing off chip, helps to prevent bubble formation due to hydrolysis, prevents electrode delamination, and allows for a cheaper method of fabrication [23].

cDEP was first used to isolate living cells from dead cells [68]. It was then used to examine the different cell types found in whole blood samples [69], isolation of cancer cells from a blood sample [70], and was used to mix particles in a microfluidic device [71]. It has also been expanded to isolate prostate tumor cells based on their bioelectrical signature [53].

Eventually a way to apply cDEP at low frequencies (below 100kHz) was developed [23] which paved the way for the characterization of cells and proved to be the foundation for many of the devices designed and validated in this work.

The development of improved cancer models has enabled research into the bioelectrical differences between otherwise similar groups of cells. Use of the Mouse Ovarian Surface Epithelial cell line derived

from C57BL6 mice was developed at Virginia Tech to study the sequence of events that lead to the development of ovarian cancer[72] [73]. cDEP has been used to differentiate between MOSE cells, macrophages, and fibroblasts [74], four different cancer stages in the MOSE cell line [75], and distinguish between MOSE cells left untreated and MOSE cells treated with sphingolipid metabolites [76]. Based on these results we can hypothesize that the drug resistant phenotype of cells will impart a unique bioelectrical fingerprint. It may also be possible to exploit these unique bioelectrical fingerprints to monitor the development of MDR and tumor recurrence.

These works laid the foundation for further exploration into how various drug treatments affect the bioelectrical fingerprint of cancer cells. These works also spurred further interest into developing better methods for isolating TIC's.

1.3.3 Relationship to Biophysical Traits in Cells

It has been well established that cells undergo biophysical changes as they progress through cancer stages. In this section I will outline some of those changes. These biophysical differences are crucial to understand in order to use those intrinsic properties to separate different cell types and subpopulations.

It can be shown that the shape, size, and properties of the cell membrane, are the dominating characteristics for the first crossover frequency, can drastically change the dielectric properties of a cell. For example, with all other properties remaining the same, a larger cell will experience a lower first crossover frequency than a smaller cell. Factors such as nucleus to cytoplasm ratio, permittivity, and cytoplasmic conductivity are thought to play a more dominating role in the value of the second crossover frequency [25].

There have been extensive studies showing differences between healthy cells and cancerous cells. [77] proposed that normal cells become malignant when they acquire chromosomal abnormalities like aneuploidy or hyperploidy. The CD47 marker has also been recently established as a major pathway in cancer immune invasion as summarized by [78]. [79] revealed that the second crossover frequency should be sensitive to internal dielectric properties of the cell, specifically finding that those properties were sensitive to the osmolarity and the temperature of the cell suspending medium.

Differences have been found between normal cancer cells and cancer cells that have developed multi drug resistance and/or drug sensitivity. [80] found that drug sensitivity is associated with low ionic conductance in a breast cancer cell model. Significant differences between cell lines with and without multi-drug resistance in their cytoplasmic conductivities have been found [81].

Even in noncancerous cells certain biophysical properties have been noted. In [82] they found that only the whole cell membrane capacitance reflected and predicted the neurogenic potential of human and mouse neural stem cells, not the membrane conductance. In [13] they found that normal stem cells have a higher natural resistance to chemotherapeutic treatment. This further supports the theory that TIC's and CSC's are the same cancer subpopulation.

TIC cells have been found to have several unique biophysical differences than normal cancer cells. The first, and most dramatic, of which is their potential for unregulated self-renewal as described by [13]. These cells are also capable of forming tumor spheres in a particular environment where normal cancer cells, even those that are highly tumorigenic, are not able to as shown in [26]. [83] showed that they could distinguish from cell's with differences in differentiation, tumorigenicity, and malignancy based on its mitochondrial membrane potential. [25] discussed some of the parameters that they expected to be lower in CSC's than in the differentiated progeny, namely; nucleus to cytoplasm ratio and a higher internal complexity due to there being a larger presence and number of organelles.

Circulating tumor cells also have distinguishing characteristics. [84] found size to be a distinguishing feature as CTC's could be separated from other blood components by using filters with varying geometry.

CTC's and CSC's have been linked as the process of epithelial-mesenchymal transition is very similar, suggesting the observed differences for CSC"s are the same as those for CTC's, as discussed by [85].

1.4 Contributions

The original purpose of this work was to determine differences in the bioelectrical fingerprint between several critical cancer types. Results shown in Chapter 2 illustrate a difference between Tumor Initiating Cells, Multiple Drug Resistant Cells, and their bulk populations for experiments conducted on three prostate cancer cell lines and treated and untreated MOSE cells. However, three significant issues confounded these experiments and challenged the use of the cDEP platform. The purpose of this work then became the development of solutions to these barriers and presenting a more commercializable cDEP platform. These large limitations hindered the cDEP platforms efficacy at manipulating cells and working as a lab on a chip (LOC) system. Those limitations have been identified and solutions are presented in individual chapters.These limitations hindered the cDEP platforms effectiveness at manipulating cells and working as a lab on a chip (LOC) system. Those barriers were identified and solutions were developed as presented below in individual chapters for each solution.

The first limitation was a lack of intuitive device performance analysis tools. The preexisting data analysis script added a significant amount of error and was incapable of morphological measurements as well as individual cell tracking. An improved analysis script, presented in **Chapter 4**, was developed that performed whole cell detection, morphology measurements, and cell tracking with an accuracy of 93.5%.

The second limitation was a need for smart sample handling. A loading system for performing smart sample handling, specifically cell focusing, was developed using a new in-house system and validated and is presented in **Chapter 5**. Experimental results validated the model and showed that cells were successfully focused into a tight band in the middle of the channel.

The third and final limitation was the use of a large pump that made the system bulky, expensive, non-transportable, and struggled with low sample volumes. Too often LOC technologies are not able to reach a truly commercial market due to the amount of expertise required to operate the system and the large and expensive systems needed to drive the chip. An effective pump capable of handling nL and µL flow volumes is one of those critical technologies that needs to be developed in order to minimize the overall footprint of the system. This was addressed by developing an on-chip micropump, presented in **Chapter 6**, and achieved 4.5% in-plane deformation. When bonded over a microchannel, fluid flow was induced at 157.5 nL/hour.

With these solutions the cDEP platform is ultimately stronger and more versatile. It will now be possible to move into more intensive and elaborate experimental studies. Further research into isolating TIC's should prove incredibly fruitful. This will bring the competitive cDEP platform to a point where it is ready for commercialization. In addition these solutions will improve other commercializable microfluidic platforms.

Chapter 2 Dielectrophoresis and Microfluidics Theory

2.1 Microfluidic Theory and Notes on Scaling Laws

Systems designed on the microfluidic scale present interesting design advantages and challenges. The main advantages will be presented in the methods section and includes such items as decreased manufacture cost, easy disposal, and reduced consumption of reagents. The main challenge to adopting microfluidic diagnostic technologies are due to their scale and the change in governing laws.

Movement in a microscale world is very different than in a macroscale world. Imagine being shrunk down to a very small size, several microns tall. Movements that are easy on the macroscale are going to be ineffective on the microscale. On the microscale the fluid is going to behave more viscously, for example more similar to honey or molasses. Moving your arms back and forth will be challenging and will produce no movement whereas "corkscrewing" movements will be more effective and will produce movement.

The Reynolds number,

$$Re = \frac{\rho v L}{\mu} \quad (1)$$

where *Re* is the Reynolds number, density of the fluidρ, kinematic viscosity *v*, dynamic viscosityμ, and the characteristic linear dimension *L*, a dimensionless number that is used to predict fluid motion on different scales. It is the ratio of inertial forces to viscous forces. Essentially it tells us which forces are dominant in a system. At large Reynolds number values, *Re*>>2300, inertial forces prevail and turbulent flow is present, characterized by eddies, vortices, and flow instabilities. At small Reynolds numbers, *Re*<<1, viscous forces prevail and laminar flow is present, characterized as smooth fluid flow with no mixing or disruption between fluid flow layers.

This means that on a microscale fluid streams will run parallel to each other with little to no mixing. This is called laminar flow. Motion will be highly predictable; however it will be counterintuitive to what we are used to encountering in our day to day lives.

That particle, being pushed through a microfluidic channel, experiences Stokes Force,

$$\boldsymbol{m}\frac{\boldsymbol{du}}{\boldsymbol{dt}} = -\boldsymbol{\gamma}(\boldsymbol{u} - \boldsymbol{v}) + \boldsymbol{F} \quad (2)$$

Where *m* is the particles mass, particle velocity *u*, fluid velocity *v*, γ friction factor, and constant force *F*. Stokes flow makes several assumptions. It assumes a low Reynolds number and laminar flow, spherical particle geometry, homogenous surface texture, and that particles move independently and do not interact or interfere with each other (adapted from [86]).

For a spherical particle

$$\boldsymbol{\gamma} = \boldsymbol{6\pi\eta a} \quad (3)$$

Where a is the particle radius and η, in this case, is the dynamic viscosity of the medium. This allows us to find the particle velocity given a constant force as (adapted from [86])

$$\boldsymbol{u} = \left(\boldsymbol{u_0} - \boldsymbol{v} - \frac{\boldsymbol{F}}{\boldsymbol{\gamma}}\right)\boldsymbol{e}^{-(\gamma/m)t} + \boldsymbol{v} + \frac{\boldsymbol{F}}{\boldsymbol{\gamma}} \quad (4)$$

where u_0 is the particles initial velocity.

At the terminal velocity the particle velocity is equal to the fluid velocity. We can find the terminal velocity by knowing that the characteristic time of acceleration, $\tau_a = m/\gamma$ is very small, less than 1 second. The terminal velocity, then, is (adapted from [86])

$$\boldsymbol{u = v + \frac{F}{\gamma}} \quad \textbf{(5)}$$

Gravity, while still an external force, plays a different role than that which we are used to on the macroscale. The gravitational force on a spherical particle can be described as (adapted from [86])

$$\boldsymbol{F_g = v(\rho_P - \rho_m)g} \quad \textbf{(6)}$$

for a particle of mass density ρ_P, fluid density ρ_m, particle volume v, and gravity g. We can then estimate the magnitude of the velocity by making the assumption that $|\rho_P - \rho_m|$ is on the order of ρ_m as being (adapted from [86])

$$\boldsymbol{u_g = \frac{v|\rho_P - \rho_m|g}{f} = \frac{2}{9}\frac{a^2|\rho_P - \rho_m|g}{\eta} \sim 0.2\frac{a^2\rho_m g}{\eta}} \quad \textbf{(7)}$$

Flow through a microfluidic device follows a parabolic curve due to the no slip boundary conditions along the walls of the microfluidic device. We can find the horizontal drag due to the cell being in contact with the wall as ([87]

$$\boldsymbol{F_{horizontal} \sim 6\pi c r \eta(v_m - v_p)} \quad \textbf{(8)}$$

where η is the dynamic viscosity of the suspending medium, v_m is the velocity of the fluid medium, v_p is the velocity of the particle, and $c = 1.7v_m$ is the fluid velocity at the center of the particle and follows a parabolic profile. We can solve for ([87]

$$\boldsymbol{v_m = 6v\frac{x}{w}(1 - \frac{x}{w})} \quad \textbf{(9)}$$

where v refers to the mean velocity of the suspending medium, w is the wall spacing from top to bottom, and x is the distance of the particle from the chamber bottom.

2.2 Dielectrophoresis

2.2.1 Electric Field and Dipole Theory

It is important to be able to predict cell motion through a microfluidic cDEP device. Its motion can be considered to be a balance between all forces present. Here I determine the external forces acting on the cell and determine the DEP force that the cell feels.

The application of a voltage across dielectric and conductive materials will induce an electric field described by

$$\boldsymbol{\vec{E} = -\nabla\phi} \quad \textbf{(10)}$$

where ϕ is the applied voltage.

That particle will polarize and form a dipole. We can describe the net electrical force *F* acting on the dipole as

$$\boldsymbol{F = qE(r + d) - qE(r)} \quad \textbf{(11)}$$

where *d* is the distance between both poles, *q* is the particles charge, particle radius *r*. To simplify we can make the assumption that the distance between poles on the particle is negligible compared to the particle dimensions and electrode dimensions [88, 89].

Using Taylor series expansion we can find (adapted from [90])

$$\boldsymbol{f(x) \sim \frac{f(a)}{0!} + \frac{f'(a)}{1!}(x - a) + \frac{f''(a)}{2!}(x - a)^2 + \cdots + \frac{f^n(a)}{n!}(x - a)^n} \quad \textbf{(12)}$$

Specifically we can find the Taylor series expansion for $E(r + d)$ as (adapted from [90])

$$\boldsymbol{E(r + d) = \sum_{j=0}^{\infty}\left[\frac{1}{j!}(d \cdot \nabla)^j E(r)\right]} \quad \textbf{(13)}$$

Simplified, by assuming negligible d, we can approximate the expansion with the first two terms as (adapted from [90])

$$\boldsymbol{E(r+d) \sim E(r) + (d \cdot \nabla) E(r)} \tag{14}$$

Recall that a spherical particle in viscous flow experiences drag force described by the Stokes drag equation

$$\vec{\boldsymbol{F}}_{\boldsymbol{drag}} = \boldsymbol{6\eta r\pi}\left(\boldsymbol{u_p - u_f}\right) \tag{15}$$

where u_p is the velocity of the particle and u_f is the velocity of the fluid.

We can use the above two equations to find the net force on a dipole of infinitesimally small size

$$\boldsymbol{F_{dipole} = [qE(r) + q\big((d \cdot \nabla) E(r)\big] - qE(r) = q(d \cdot \nabla) E(r) = (p \cdot \nabla) E(r)} \tag{16}$$

2.2.2 Claussius-Mossotti Factor and Dielectrophoresis Theory

Half the induced dipole moment of the charged spherical particle is described as

$$\boldsymbol{\gamma_{DEP} = 2\pi \epsilon_m r^3 Re[K(\omega)]} \tag{17}$$

where the radius of the cell is r, ϵ_m is the relative permeability of the suspending medium, and $Re[K(\omega)]$ is the real portion of the Clausius-Mosotti factor. The Claussius-Mossotti factor reveals the direction of the DEP force applied to a particle and is theoretically bound between 0.5 and 1. Essentially it describes the effective polarizability of the cell in a suspending medium. It is described by

$$\boldsymbol{[K(\omega)] = \frac{\epsilon_p^* - \epsilon_m^*}{\epsilon_p^* + 2\epsilon_m^*}} \tag{18}$$

$$\boldsymbol{\epsilon^* = \epsilon + \frac{\sigma}{i\omega}} \tag{19}$$

where ϵ_p^* is the permeability of the particle and ϵ_m^* is the permeability of the medium. A polarized particle in a non-uniform electric field experiences a dielectrophoretic (DEP) force described by

$$\vec{\boldsymbol{F}}_{\boldsymbol{DEP}} = \boldsymbol{\gamma_{DEP} \nabla}\left(\vec{\boldsymbol{E}} \cdot \vec{\boldsymbol{E}}\right) \tag{20}$$

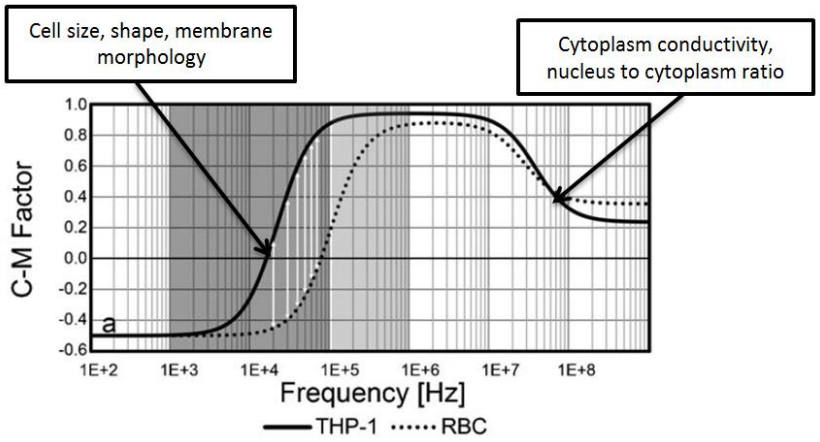

Figure 1: The Claussius-Mossotti curve for several different cells types. Overlaid text shows the dominant biophysical traits at the first and second crossover frequencies. In the area where the CM factor is between 0 and -0.5 the cells experience nDEP, in the 0 to 1 area the cells experience pDEP. Difference cells have different biophysical properties that will shift the CM curve as shown above by the difference curves. Displayed with permission from [69].

The DEP force, depending on the polarity of the electric field, either directs the cells towards or away from strong or weak electric field regions. This depends on the electrode and channel geometry. [87]

For a solid lossy spherical particle the DEP force can be written as

$$\boldsymbol{F_{DEP} = 2\pi a^3 \epsilon_m Re[K(\omega)] \nabla(\vec{E} \cdot \vec{E})} \quad \textbf{(21)}$$

We can define a particle independent DEP vector, based on [23], as

$$\boldsymbol{\vec{\Gamma}_{drag} = \frac{\vec{F}_{DEP}}{\gamma_{DEP}} = \nabla(\vec{E} \cdot \vec{E})} \quad \textbf{(22)}$$

The first crossover frequency, where the DEP force transitions from negative to positive, is dependent upon intrinsic cell characteristics, such as size, morphology, etc., that vary by cell type. In a lateral non-uniform field the particle will experience a DEP force in one direction. It is possible that for cells that possess dissimilar dielectric properties there is a region where one cell type will experience negative DEP and the other will experience positive DEP [87].

A commonly made next step is the DC approximation. However, above 1 MHz this assumption is no longer applicable. In order to predict the behavior of mammalian cells in high frequency regions, e.g. above 1 MHz, the multi-shell model, discussed below, can be applied and the equations re-derived. This is needed in order to predict the location of the second crossover frequency. The needed dielectric values are the nucleoplasm permittivity (ε_{np}), cytoplasm permittivity (ε_{cp}), nucleoplasm conductivity (σ_{np}), cytoplasm conductivity (σ_{cp}), and the nucleus volume fraction (nucleus volume to cell volume) (v). The development of the following equations shows a considerable advance in the theory and modeling of DEP [79].

$$\boldsymbol{f_{xo} = \frac{1}{2\pi}\sqrt{\frac{(\sigma_m - \sigma_c)(\sigma_c + 2\sigma_m)}{(\varepsilon_c - \varepsilon_m)(\varepsilon_c + 2\varepsilon_m)}}} \quad \textbf{(23)}$$

$$\boldsymbol{\varepsilon_c \approx \varepsilon_{cp} \frac{2(1-\nu) + \frac{\varepsilon_{np}}{\varepsilon_{cp}}(1+2\nu)}{(2+\nu) + (1-\nu)\frac{\varepsilon_{np}}{\varepsilon_{cp}}}} \quad \textbf{(24)}$$

$$\boldsymbol{\sigma_c \approx \sigma_{cp} \frac{2(1-\nu) + \frac{\varepsilon_{np}}{\varepsilon_{cp}}(1+2\nu)}{(2+\nu) + (1-\nu)\frac{\varepsilon_{np}}{\varepsilon_{cp}}} - \left(\frac{\varepsilon_{np}\sigma_{cp} - \varepsilon_{cp}\sigma_{np}}{\varepsilon_{cp}} \frac{9\nu}{\left[(2+\nu) + (1-\nu)\frac{\varepsilon_{np}}{\varepsilon_{cp}}\right]^2} \right)} \quad \textbf{(25)}$$

The changes that are undergone by a cell around the occurrence of the second crossover frequency had not been closely examined due to current commercial signal generator limitations. While the first crossover frequency had been shown to reveal the external properties of cells such as membrane capacitance, viability, and morphology, theory indicated that the second crossover frequency could reveal internal dielectric characteristics [79].

2.2.3 Single Shell and Multi Shell Models

Biological cells are often nonhomogeneous, made up of many smaller organelles, noncircular, with surface protrusions. This means that the assumptions that have been made up to this point do not always apply to working with cells. We can then modify the DEP model to take account of these differences [91].

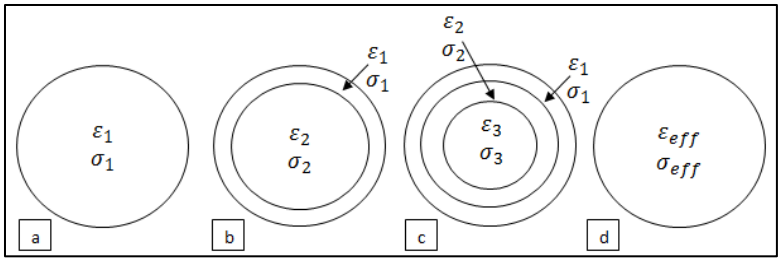

Figure 2: (a) model of a solid sphere, this represents particles like latex beads. (b) A single shell model with different permittivity and conductivity values in the two shell layers. (c) Multi-shell model where the outermost shell represents the outer membrane, middle shell layer represents the interior structures, and the innermost shell layer represents the nucleus. This process of adding more and more shell layers to represent individual organelles can be repeated infinitely. (d) The effective values of the permittivity and conductivity are found for the particle.

We can develop a model of cells with concentric shells to mimic the phospholipid bilayer membrane and the myriad of internal organelles such as the nucleus. The simplest shell model, the single shell model, uses a single shell layer to represent the cell membrane and an interior shell layer to represent the cell cytoplasm as shown in the figure above. We can find the effective permittivity as

$$\boldsymbol{\epsilon_{23}^* = \epsilon_2^* \left[\gamma_{12}^3 + 2\left(\frac{\epsilon_3^* - \epsilon_2^*}{\epsilon_3^* + 2\epsilon_2^*}\right)\right] / \left[\gamma_{12}^3 - \left(\frac{\epsilon_3^* - \epsilon_2^*}{\epsilon_3^* + 2\epsilon_2^*}\right)\right]} \quad \textbf{(26)}$$

where $\gamma_{12}^3 = a_1/a_2$ [90].

A more detailed model is the multishell model, as seen above. In it the outermost shell represents the membrane, the middle shell represents cytoplasm, and the innermost sphere represents the cell nucleus. We can modify the above equation to account for the interface between the cytoplasm and the nucleus.

$$\boldsymbol{\epsilon_{34}^* = \epsilon_3^* \left[\gamma_{23}^3 + 2\left(\frac{\epsilon_4^* - \epsilon_3^*}{\epsilon_4^* + 2\epsilon_3^*}\right)\right] / \left[\gamma_{12}^3 - \left(\frac{\epsilon_4^* - \epsilon_3^*}{\epsilon_4^* + 2\epsilon_3^*}\right)\right]} \quad \textbf{(27)}$$

where $\gamma_{23} = a_2/a_3$ [90].

Although the single-shell model has been successful for predicting the biophysical properties of cells, it sometimes deviates from the experimental results [92]since the real cellular structure is more complex than that assumed by the single-shell model. For instance, this model assumes cells have a thin and spherical membrane which surrounds a spherical homogeneous interior, and thus does not take into account membrane inhomogeneity and cytoplasm and nuclear structural features [93]. Consequently, this model cannot correlate specific membrane capacitance with membrane morphological complexity.

2.2.4 Non-Spherical Particles

In addition to often being nonhomogeneous, biological cells are very rarely ever perfectly spherical. It has been shown even a relatively simple change of a particles shape from a sphere to an ellipsoid can drastically change a particles dielectric properties and subsequent the DEP force that it experiences as shown in [94].

The dipole moment for a non-spherical particle will have a different dipole moment along each axis. This results in the largest axis being oriented parallel with the electric field at low frequencies as it exerts the greatest amount of torque on the particle. At higher frequencies the dipole along the long axis will start to disperse and it will rotate to align itself to be parallel with the electric field.

We can write out a term called the depolarization factor in order to account for differing polarization [33]

$$\boldsymbol{A_{j,\alpha} = \frac{a_j b_j c_j}{2} \int_0^\infty \frac{ds}{(s+i_\alpha^2)R} \text{ where } i_x = a,\ i_y = b, i_z = c,} \quad \textbf{(28)}$$

and $R = \sqrt{(s+a^2)+(s+b^2)+(s+c^2)}$

where the subscripts refer to the axis.

We can then modify the CM Factor to account for the charging being different along each axis [33].

$$\boldsymbol{[K(\omega)] = \frac{\epsilon_{eff}^* - \epsilon_m^*}{(\epsilon_{eff-}^* \epsilon_m^*)A_\alpha + \epsilon_m^*}} \quad \textbf{(29)}$$

Finally we can find the effective complex permittivity of the cell as a function of the depolarization factor. [33]

$$\boldsymbol{\epsilon_{eff,\alpha}^* = \epsilon_{mem}^* \frac{\epsilon_{mem}^* + (\epsilon_{cyto}^* - \epsilon_{mem}^*)[A_{2\alpha} + v(1 - A_{1\alpha})]}{\epsilon_{mem}^* + (\epsilon_{cyto}^* - \epsilon_{mem}^*)[A2_\alpha - vA_{1\alpha}]}} \quad \textbf{(30)}$$

where $v = r^2 c/[(r+d)^2(c+d)$ is the volume ratio of the cell exterior to interior and $A_{1\alpha}$ is the axial polarization from evaluating just inside the membrane out to infinity.

We can then find the final polarization factor for two common shapes, a prolate spheroid [33]

$$\boldsymbol{A_{j,b} = \frac{1-e_j^2}{2e_j^2}\left(ln\frac{1+e_j}{1-e_j} - 2e_j\right), j = 1, 2} \quad \textbf{(31)}$$

where $e_j = \sqrt{b_j^2 - a_j^2}/b_j$ is the eccentricity,

and an oblate spheroid for $b < a = c$ [33]

$$\boldsymbol{A_{j,b} = \frac{2e_j^2 - \pi\sqrt{a-2e_j^2}}{2e_j^3} + tan^{-1}\left(\sqrt{1-e_j^2}\right), j = 1, 2} \quad \textbf{(32)}$$

where $e_j = \sqrt{b_j^2 - a_j^2}/a_j$ is the eccentricity.

2.2.5 Electrorotation

As mathematically shown earlier, a particle in a non-uniform field will experience a dielectrophoretic force dependent upon the ratio of the permittivity of the medium to the permittivity of the particle, called the Claussius-Mossotti factor. The response of mammalian cells in an electromagnetic field changes across the frequency spectrum, which means that the force acting upon the cell will change as the frequency changes. A rotating field will induce particle electrorotation, a common characterization technique [87]. Electrorotation allows for the determination of biological properties of cells.

We can develop an intuitive understanding of the motion of a cell in a rotating field by considering the dipole equation developed earlier. In a uniform electric field the dipole experiences an equal force in all directions which causes it to align with the field. However it requires a finite amount of time for the particle to align itself in the field, meaning that as the frequency of the field is increased at some point the particle will no longer be able to move fast enough to align itself with the field. This movement of the cell aligning it's dipole with the surrounding field polarity makes it appear that the particle is rotating.

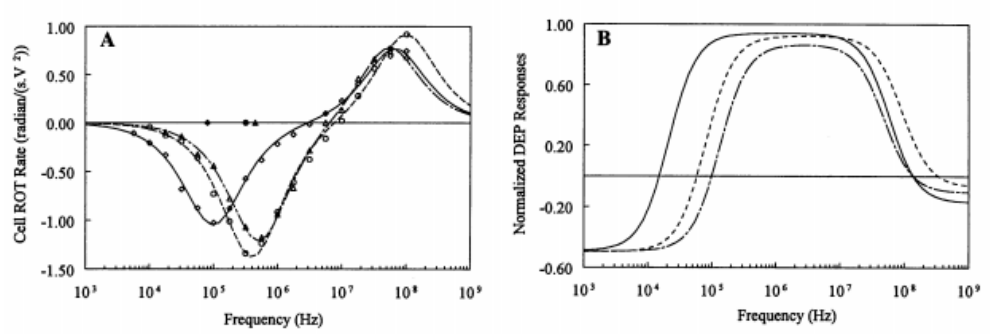

Figure 3: Left shows the electrorotation spectra (A) while on the right is the DEP spectra (B). Taken with permission from Mike Sano and Rafael Davalos [69].

Electrorotation can occur in any electrical field with a spatially independent phase. We can begin by developing the equations for the time-averaged first order torque on the particle as [95]

$$\boldsymbol{\Gamma_{ROT}} = \frac{1}{2}\mathbf{Re}[\boldsymbol{p} \times \boldsymbol{E}^*] = \frac{1}{2}\boldsymbol{v}\mathbf{Re}[\vec{\alpha}(\vec{E} \times \vec{E}^*)] = -\boldsymbol{v}\mathbf{Im}[\vec{\alpha}](\mathbf{Re}[\vec{E}] \times \mathbf{Im}[\vec{E}]) \quad \textbf{(33)}$$

In a field designed with a rotating field and four quadropole electrodes the particle will experience a constant torque. The direction of rotation will be with the field if the induced dipole moment of the particle lags behind the field. We can describe the torque, then, as [95]

$$\boldsymbol{\Gamma_{ROT}} = -\boldsymbol{v}\boldsymbol{Im}[\vec{\alpha}]|\boldsymbol{E}|^2 = -\boldsymbol{4\pi\epsilon_m a^3}\mathbf{Im}[\tfrac{\epsilon_p - \epsilon_m}{\epsilon_p + 2\epsilon_m}]|\boldsymbol{E}|^2 \quad \textbf{(34)}$$

Chapter 3: Motivation for an Improved Contactless Dielectrophoresis Platform

3.1 Hypothesis for Experiments

If it can be shown that TIC's, MDR cells, and their bulk populations have measurable differences, the usefulness of our isolation and sorting platform is expanded. These are cell populations that are very challenging to isolate, even using current commercial techniques. Isolating them would establish cDEP as a viable cell isolation platform. It was hypothesized that these experiments would yield two results:

- The trapping voltage will be different between prostate cancer TIC's, non-TIC's, and their bulk populations
- MOSE cells that have been treated to become TIC's or MDR will have a different crossover frequency

3.2 Handling of Biomaterials

3.2.1Cell Lines

For investigating the isolation of tumor initiating cells the commercial human cancer cell lines PC3, DU145, and LNCaP (ATCC) were used. All three are cancer cell lines isolated from the prostate and have different levels of tumorigenicity, which represents the complete spectrum of the disease. The presence of the ALDH marker, commonly used as a marker for TIC properties, was used to isolate the TIC's in order to characterize them.

The mouse ovarian surface epithelial (MOSE) cell line is a syngeneic cell line [73]. A common problem with human derived cell lines is that they are cultured from different patients and therefore may have genetic differences and present differently. In the MOSE model, because it is taken from mice, the different malignant stages were isolated and cultured allowing for comparison between stages without encountering inter-subject genetic differences. As paclitaxel and cisplatin are two of the most commonly administered drugs to treat ovarian cancer, a customized cell line with resistance to both chemotherapeutics was developed by Dr. Roberts and Dr. Schmelz labs from the MOSE cell line. In addition the TIC subpopulations were isolated by Dr. Roberts and Dr. Schmelz labs and cultured.

3.2.2 Cell Maintenance and Preparation

MOSE cells were cultured in high glucose DMEM (Sigma-Aldrich) that was supplemented with 4% FBS and 1% P/S (Sigma-Aldrich). DU145, PC3, and LNCAP cells were cultured in RPMI 1640 (1X) GIBCO (Life Technologies) media that was supplemented with 10% FBS (Sigma-Aldrich) and 1% P/S (Sigma-Aldrich). 3 to 4 days were allowed between passages.

Prior to experiments cells were removed from the flask by trypsinization. They were then washed with PBS and resuspended into low conductivity buffer. The low conductivity buffer is made in house and is a combination of 8.5% sucrose (w/v), 0.3% glucose (w/v), and .725% cell culture media (RPMI) (w/v) suspended in DI water. The fluid was made sterile by filtering. The cells are then stained with either Calcein-AM or Calcein red-orange (Molecular Probes Inc, Carlsbad, CA, USA) for 20 minutes at room temperature. The cells are then spun down at 1200 rpm for 5 minutes using a centrifuge and resuspended in the low conductivity buffer at 4 million cells per mL ratio. The final conductivity of the fluid with the cells added was between 90 and 110 µS/cm measured using a conductivity meter (Horiba Scientific).

Prior to experiments cell viability was assessed using either a hemocytometer or a cell count machine (Vi-Cell series, Beckman Coulter). Using the hemocytometer a cell sample of 10 µL was used and cells were counted at low magnification. Using the Vi-Cell machine a 1 mL sample was gathered and tested using trypan blue stock solution.

3.2.3 Flow Cytometry

Flow cytometry was used in some experiments in order to isolate a TIC baseline for characterization studies. Cells were dyed using the Aldefluor kit and according to their instructions (Stem Cell Technologies). Cells were kept on ice prior to being brought to the flow cytometry technician. The bottom 10-20% population and the top 10-20% populations based on brightness were returned separately. The cells were kept on ice as they were returned to lab. The cells were then resuspended and dyed.

3.2.4 Protospheres Culture

Spheroid formation capability was assessed by performing protosphere culture. Cells were plated in 10 cm low attachment dishes at 1 million cells per mL ratio. The media was composed of Endothelial Cell Basal Medium (EBM) (Lonza), with the addition of 2% B27 (Gibco) (w/v), 4 µg/mL insulin (Invitrogen), 20 ng/mL EGF (Fisher), and 20 ng/mL FGF (Invitrogen). For each plate 10 mL of EBM media with supplements was added.

After 14 to 20 days the spheres were collected and analyzed. This was done using a microscope at low magnification to count colonies. The number and size of colonies were recorded.

3.2.5 Thawing/Freezing Cells

Cell types were backed up by freezing and storing in liquid nitrogen. Cells were split into 1 million cells per mL ratio and resuspended into freezing media consisting of 10% DMSO, 20% FBS, and remaining growth media.

To thaw cells that had been backed up in liquid nitrogen the ampule is first removed. It was immediately placed in 37 degree C water bath and agitated to thaw quickly. The contents are then transferred to a centrifuge tube containing 5 mL PBS and spun at 1300 rpm for 5 minutes. The pellet is then resuspended and transferred to flasks.

3.3 Device Fabrication and Design

3.3.1 Single Layer Microfluidic Device Fabrication Method using DRIE

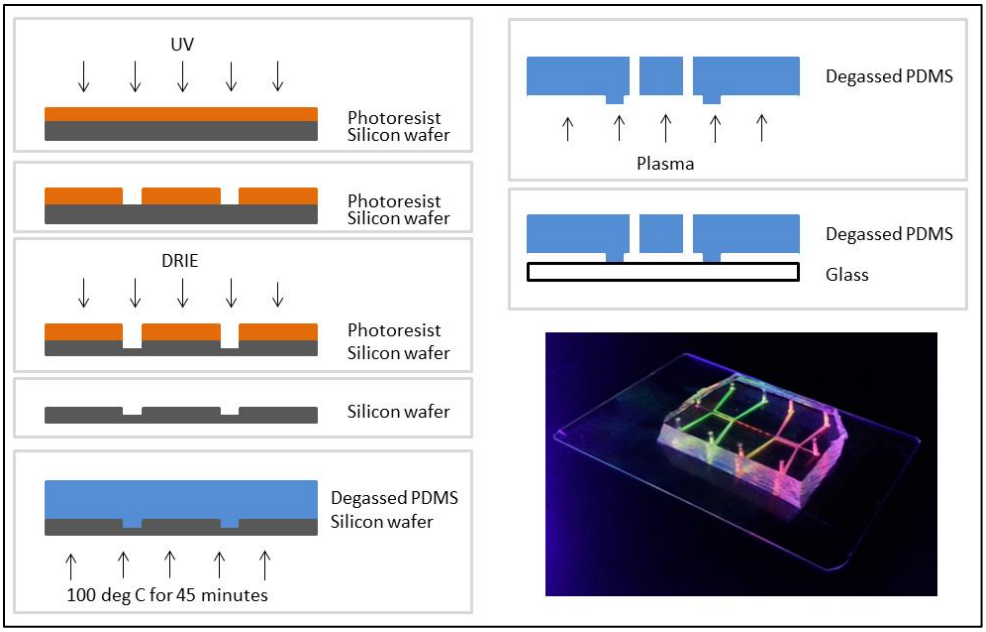

Figure 4: Overview of the single layer fabrication process using DRIE. The wafer is first cleaned and photolithography is performed in order to create a masking layer during the DRIE process. PDMS is cured using the wafer as a mold, punched, and then bonded to glass using a plasma cleaner.

The silicon master mold was fabricated using <100> silicon. The wafer is first cleaned by rinsing with acetone, isopropyl alcohol, and finally deionized water. Photoresist is spun and patterned by UV through a transparency mask (OutputCity). The photoresist is used to protect sections of the wafer from being etched during the Deep Reactive Ion Etching (DRIE) process where etching occurs due to the wafer being bombarded with reactive ions. The completed wafer is treated with Teflon in order to improve the removal of PMS and prevent the silicon from chipping.

PDMS (Sylgard 184, Dow Corning) is mixed at a 10:1 base to curing agent ratio and degassed. The PDMS is then poured onto the mold, using aluminum foil for containment, and cured at 100 C for 45 minutes. The PDMS is peeled off and holes are punched (Howard Electronic Instruments). The cleaned PDMS is treated with air plasma for 2 minutes and then bonded with a clean glass slide. Completed devices are stored under vacuum.

3.3.2 Numerical Modeling of Pre-existing Low Frequency Device Design

A two dimensional geometry had been previously created in AutoCAD (AutoCAD Mechanical 2010, Autodesk Inc., San Rafael, Ca, USA). The geometry was imported into Comsol Multiphysics (Version 4.3, COMSOL Inc., Burlington, MA, USA). To model the electric field the AC/DC module was used (electric currents) and to model Stokes drag the fluid flow module was used (laminar flow).

Edges of the electrode channels were modeled as a uniform potential of 200 V or 0V. The regions of the model were set to represent poly(dimethylsiloxane) (PDMS) (Sylgard 184, Dow Corning), phosphate buffer solution (PBS), or sample media. PDMS was modeled as having a conductivity of $0.83*10^{-12}$ S/m and a relative permeability of 2.65 as defined by data from the manufacturer. PBS was defined as having a conductivity of 1.4 S/m and a relative permeability of 80 from experimental measurements previously taken. The sample media was modeled as a sugar solution and assigned a conductivity of 100 µS/cm and

relative permeability of 80 as found from previous experimental measurements. The flow at the inlet was set to 0.000056 m/s.

In the frequency range where the Claussius-Mossotti factor is negative, the cells, or particles, are repelled from regions of the highest electric field gradient. As the frequency is increased, the Claussius-Mossotti factor becomes positive and the cells, or particles, will be attracted to the regions with the highest electric field gradient. It has been demonstrated that manipulation of particles or cells is possible when $\vec{\Gamma}_{drag}$ is 10^{-12} [23].

We can see that the DEP force felt in the channel is around 0.2×10^{12} m*kg^2/(s^6*A^2). In the sawtooth features, the DEP force increases to upwards of 1.8×10^{12} m*kg^2/(s^6*A^2). This means that the DEP force has the most impact in the sawtooth features. Due to the asymmetry of the device, the regions with the highest electrical field gradient are at the top of the sample channel. Therefore cells, or particles, will be attracted to the top of the sample channel when in the frequency range where the Claussius-Mossotti factor is positive and repelled from the top when the Claussius-Mossotti factor is negative. As the fluid enters the sawtooth features and the channel narrows its velocity increases from less than 0.0002 m/s to greater than .0014 m/s.

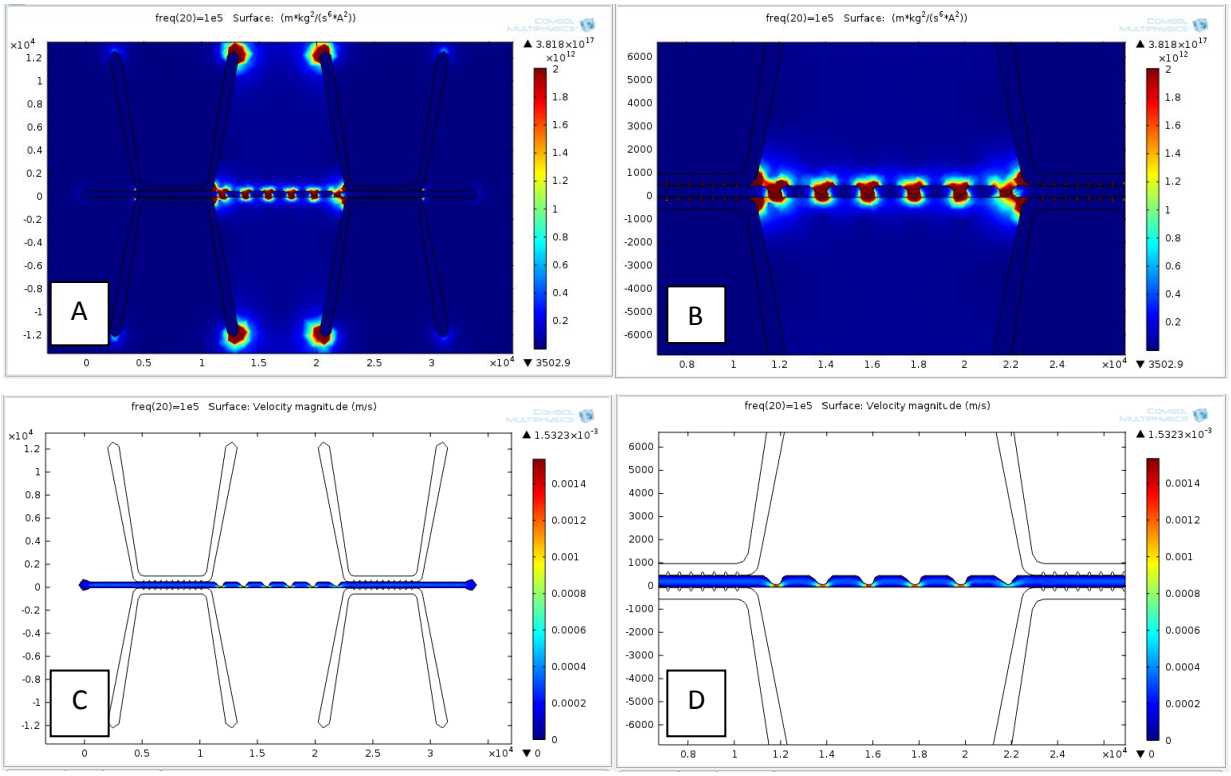

Figure 5: Resultant Comsol plots are shown. (A) shows the full model plot from the AC/DC (B) focuses on the sawtooth features from the AC/DC module (C) shows the full model plot from the Fluid Flow module (D) focuses on the sawtooth features from the Fluid Flow module

The results from the model show that the electric field gradient and resultant DEP force, as well as the fluid velocity, can be easily modeled and predicted. This is an important development for cell sorting technology. One flaw with this design is that the area where the DEP force has the most effect, in the

sawtooth features, is also where the fluid flow velocity is the highest, so the particle moves the most quickly through that section.

Many assumptions were made in creating the cDEP model that may limit its scope. The biggest limitation was the 2D assumption. It was assumed that propagation was infinitely possible along the z access in order to construct the model in 2D. This is a valid assumption for the electric field, however is not a valid assumption for fluid flow. For more complicated designs this can be addressed by extruding the model 20 μm in the z dimension to make it 3 dimensional and more realistic.

This model demonstrates how critical modeling is in developing devices for cDEP. In conclusion this model further allows for the prediction of the dielectrophoretic force in a sawtooth microfluidic device and its velocity profile, and will serve as the basis for the development of more sophisticated models and devices.

3.4 Experimental Methods and Data Analysis

3.4.1 Experimental Procedure for Low Frequency Characterization of MOSE Cells

Once prepared, the cell suspension fluid was kept on ice in order to maintain cell viability. PDMS devices were placed under vacuum for a minimum of 30 minutes prior to experiments in order to be able to prime the main channel with the cell suspension fluid. A syringe with a needle tip (Cole-Parmer Instruments Co.) was used to pump cell suspension into the main channel inlet through Teflon tubing. After priming the channel a syringe pump (Harvard Apparatus) was used to supply a low flow rate.

The electrode fluid channels and pipette tip reservoirs were filled with 10X PBS solution. Aluminum wires with exposed ends were inserted into the electrode fluid reservoirs and alligator clips were used to connect the output from the electronics to the wires.

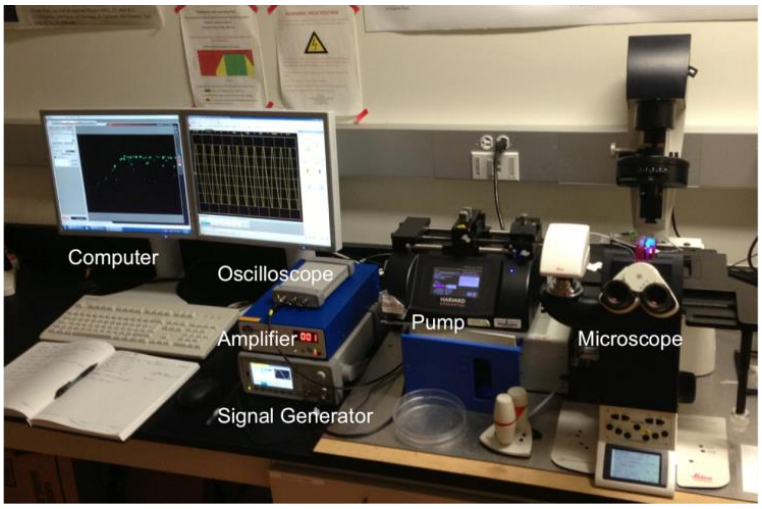

Figure 6: Picture showing the experimental setup with the pump, electronics, and microscope labelled.

There were two main electronics setups. Both setups used a function generator (GFG-3015, GW Instek) as the source signal. That signal was then amplified. The first of the two setups produces output voltages between 0-200 VRMS at frequencies between 5-100kHz and was referred to as the low frequency setup. The second pre-existing setup was designed and built in house with the final stage

connected to a step up transformer. It outputs voltages between 0-300 VRMS at frequencies between 100-600kHz. Voltage and frequency was monitored using an oscilloscope (TDS-1002B, Tektronics). An inverted light fluorescent microscope (Leica DMI 6000B, Leica Microsystems) was used for collecting videomicroscopy data. The Leica Application Suite 3.8 software (Leica Microsystems) was used for recording videos.

Once the videos were taken the results were analyzed using the above analysis script and statistical differences between different cell groups were established.

3.4.2 Method for Characterizing and Isolating TIC's from Prostate Cancer Cell Lines

Characterization studies were conducted to establish the trapping onset voltage, complete trapping voltage frequency for all three prostate cancer cells lines (DU145, PC3, and LNCaP) in addition to a non-prostate cell line – PANC1. In addition the two of the three prostate cell lines were sorted by FACS using the ALDH marker and the resultant ALDH+ and ALDH- subpopulations were assessed for the onset trapping voltage and the complete trapping voltage.

As part of a collaboration, our setup was also used to batch sort cells into the TIC and regular cancer cell populations. The voltage was increased until ~20% of the cells trapped on the posts in the device. The cells that flowed through were captured. After 30 minutes the sample channel was flushed with a buffer to remove any cells that were not trapped on posts, the electric field turned off and the cells released and captured downstream. The samples were then cultured in protosphere medium and the number and size of spheroid colonies were recorded in order to assess the number of TIC's that had been isolated.

This study used devices similar to those described in [53] for characterizing and batch sorting.

3.4.3 Data Analysis mMethods

For low frequency experiments a pre-existing analysis script was run using MATLAB (R2013a, MathWorks Inc.). Once the average cell position had been found the crossover frequency was found by linear interpolation.

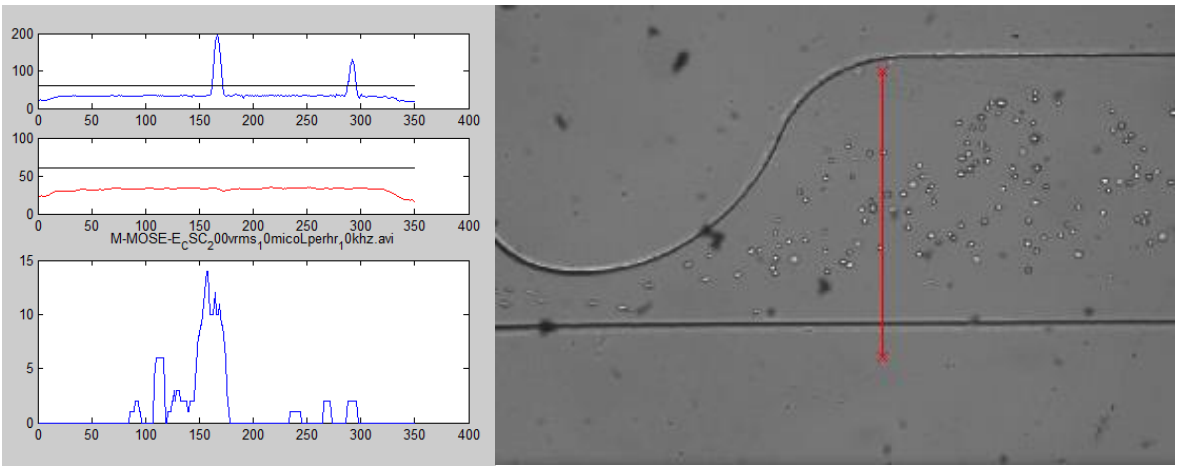

Figure 7: Images showing the results from the pre-existing data analysis script.

This pre-existing script had many limitations. It worked by counting pixels as they crossed a line that was entered in by the user. This introduces error both in that not all cells are the same size, so larger cells bias the data, and also from human error in placing the line.

The high frequency experiments were quantified by the user. For the frequencies 100, 200, 300, 400, 500, and 600kHz the voltages were noted at which 10% and 90% of the cells trapped on the posts.

In addition, when possible, the release voltage was also recorded for each frequency. In some cases this was not possible as the cells would stick to the posts in the microchannel and would only release when the channel was disturbed and the flow rate increased.

3.5 Detecting a Shift in Population Type of CSC from Prostate Cancer Cell Lines

Early characterization studies of the regular cell line, before any subpopulations were captured, showed similarities between all three prostate cancer cell lines and the pancreas cancer cell line.

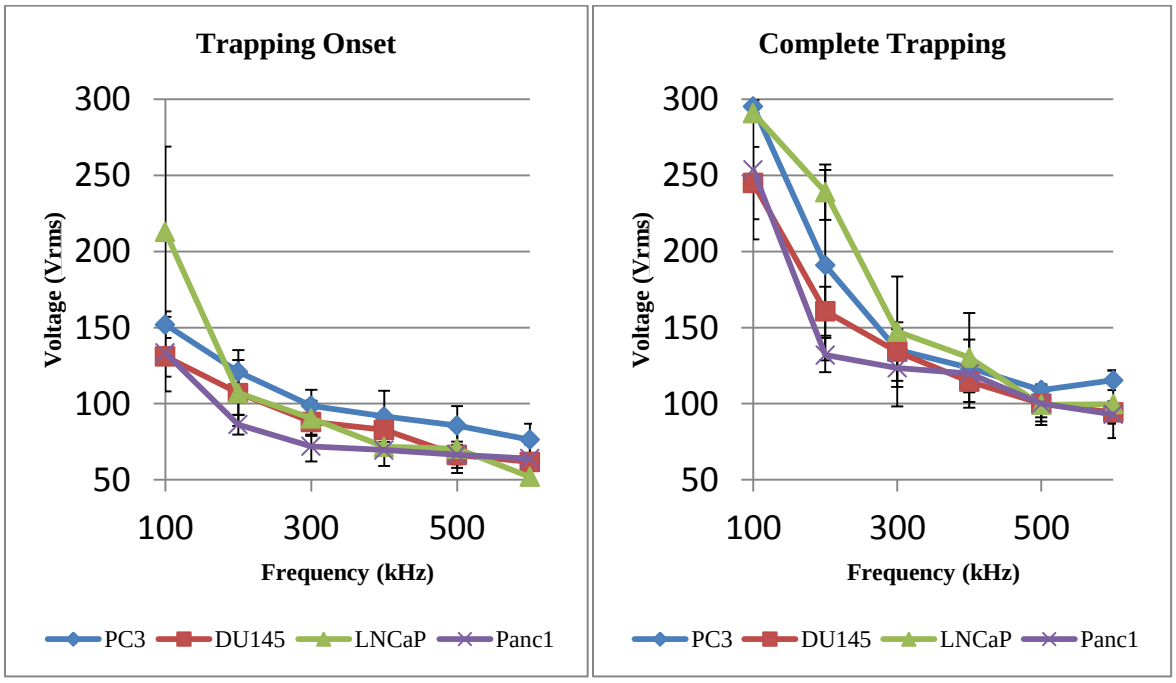

Figure 8: Preliminary comparison of cDEP on all three prostate cancer cell lines and a pancreatic cell line.

All three prostate cancer cell lines were stained. The cells were then sorted into subpopulations of cells with the highest ALDH expression (referred to as ALDH+) and those with the lowest ALDH expression (referred to as ALDH-). The representative percentage of cells that were considered to be ALDH+ and ALDH- were recorded. These values act as a baseline measurement for cells within each cell line that are considered to be TIC's using a current mainstream technique.

Table 1: ALDH+ subpopulations as detected by FACS for all three cell lines.

Cell line	Background	Sample	Resultant Subpopulation
PC3	.4%	25.1%	24.5%
DU 145	.5%	6.8%	6.3%
LN CaP	.8%	1.6%	.8%

The ALDH+ and – subpopulations for PC3 and DU145 cell lines, sorted and returned from FACS, were characterized. The LNCaP cell line, due to the incredibly low percentage of cells that are ALDH+, does not return enough ALDH+ cells to be characterized. A sample size of over 100,000 cells is required in order to perform characterization.

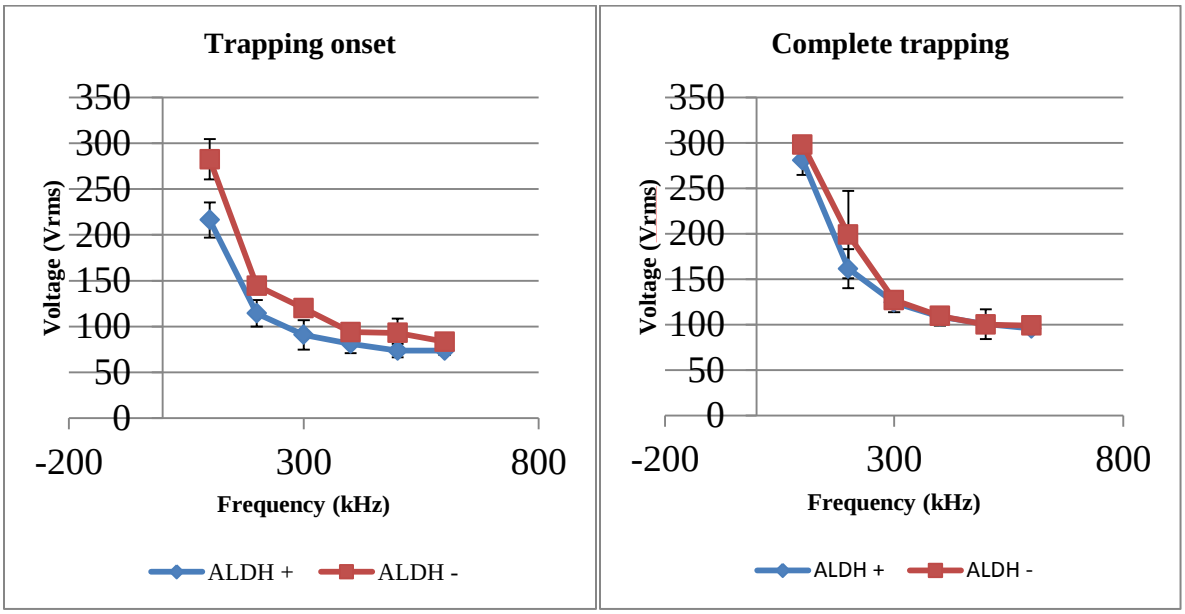

Figure 9: Preliminary results on PC3 cell line. N = 3.

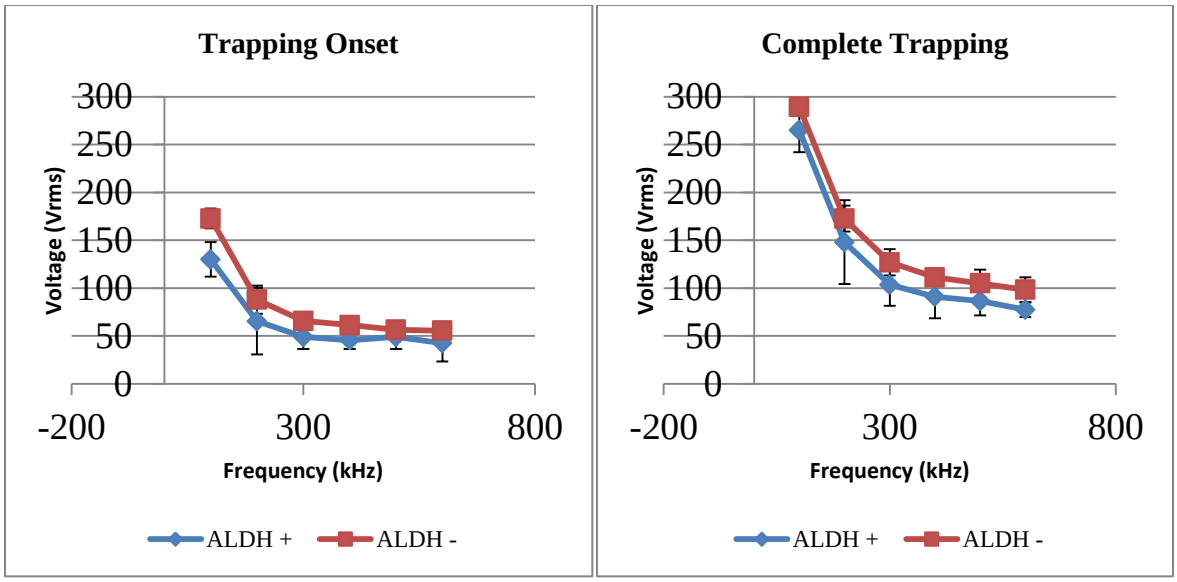

Figure 10: Preliminary results on the DU145 cell line. N = 3.

The results from characterizing the onset of trapping and complete trapping voltages for 100, 200, 300, 400, 500, and 600 kHz show that there is a difference between the ALDH+ and ALDH- subpopulations. The onset of trapping and complete trapping voltages were higher for ALDH- cells than ALDH+ cells. This preliminary work supported our hypothesis that it will be possible to use our setup to isolate TIC's and shows that future work will be viable.

DU145 and PC3 cells were then sorted using a trap-based cDEP device and verified the results by flow cytometry. From the above characterization studies we expected the cells trapped at lower voltages to possess TIC properties. Ultimately 80% purification for the DU145 line and 60% purification for the PC3 line for high ALDH+ expression was achieved by taking the populations sorted by cDEP, staining with ALDH, and analyzing using flow cytometry. Using spheroid formation we found that the sample sorted using cDEP for TIC properties was on average 4 times larger than an unsorted control, showing an enrichment of TIC cells, and 17 times larger than the cells sorted using cDEP for a lack of TIC properties.

3.6 Characterization of Subpopulations of Multiple Drug Resistant and TIC MOSE Cancer Cells

Taking advantage of the way cells react in an electric field due to their different bioelectrical properties allows for the extraction and identification of tumor initiating cell (TIC) populations. Using cDEP we have been able to characterize and compare the syngeneic Mouse Ovarian Surface Epithelial (MOSE) cell line to its TIC subpopulation and chemo resistant subpopulations. Characterizing and isolating these cells is the first step toward developing a drug regime. This could potentially be used to develop personalized treatment plans for patients with cancer, greatly improving their chances at fighting off the disease.

Low frequency experiments using the above modelled low frequency device were run to characterize MOSE cells in the sub 100 kHz range. The MOSE cell line was analyzed emphasis towards the chemoresistant and TIC subpopulations. The crossover frequency for the main cell lines (e.g. early, intermediate, and late) were analyzed in a previous study [96].

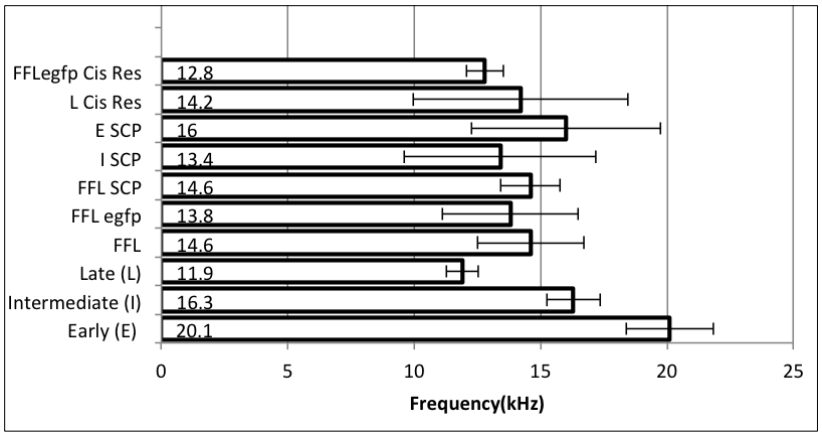

Legend	
E	Early
I	Intermediate
L	Late
FFL	Very Late
egfp	Added green fluorescent protein
SCP	Stem Cell Population/ TIC
Cis Res	Cisplatin Resistant

Figure 11: Preliminary data suggests change in the crossover frequency due to chemotherapeutic resistance. Analyzed using the original MATLAB script. Bottom three data points with permission from previous research [74] with N= 3. Remaining data points had between N = 2 to N = 6.

We determined the crossover frequency for each of the treated MOSE cell populations. Differences between the crossover frequencies for each of the cell populations show that each cell subpopulation has a different bioelectrical fingerprint. It also shows that treatments can affect the bioelectrical fingerprint of cell populations. These preliminary results show that changes in the bioelectrical properties of MOSE cells, an established in vitro model of ovarian cancer progression, are detectable and can be used to predict drug resistance and used to develop personalized medical treatments.

The MOSE cell experiments used the low frequency devices where the initial sample position is critical. Smart sample handling was missing from the device design and stood as a barrier increasing the amount of error because not all cells were starting from the same location. In addition errors due to data analysis and the large footprint served as obstacles that are overcome in the chapters below.

Once the above challenges have been addressed, as discussed in their own chapters below, it will be possible to move into more intensive and more elaborate experimental studies. Further research into isolating TIC's could prove incredibly fruitful.

Chapter 4: Creation of a High Level Data Analysis Script

4.1 Background on Cell Tracking

Microdevice design development is hampered by a lack of sophisticated analysis methods. One preexisting analysis technique counts pixels that are moving within a microchannel and does not count individual cells [97]. Establishing a single cell evaluation technique would allow for optimized device design and characterization of individual cells. Analyzing the motion of cells within microchannels is a way to characterize and monitor cell sorting and evaluate microdevice performance.

Most commercially available cell tracking tools, such as cellTrack, TLMTracker, and ImageJ, are used for doing time lapse images of the same cell as it undergoes cell events like mitosis. The tracking refers to tracking the nucleus and cell membrane as they change and deform. While a large amount of work has addressed segmentation and tracking of individual organs in a system [98, 99], relatively little effort has been devoted to cellular image and in particular imaging of moving cells. Most methods of this type have been used to study the movement of isolated cells that combine gradient image thresholding with tracking algorithms [100, 101]. These methods provide poor descriptions of the cellular shape and size and often fail to track multiple cells in a sequence.

The developed script is specifically for measuring the movement of cells as they flow through a microchannel. The goal in this project was to both dive into the algorithms behind these cell tracking techniques and also to tailor the script specifically to research where cell movement tracking, basic morphology measurements, and fast run times are critical. The presented software detects whole individual cells in order to perform analysis, which yields greater accuracy than the prior approach.

4.2 Pertinent Computer Vision Algorithms

There are a number of techniques in the field of computer vision that can be viably applied to performing cell tracking and segmentation.

4.2.1 Median and Mean Filters

Background subtraction is a very important in order to isolate and detect moving objects, in our case biological cells flowing through a microchannel. Techniques can range from simplistic to very complex with varying computational requirements. A temporal median filter which uses median values across some number of frames has the advantage of running very quickly and providing an adequate background image as long as enough frames are used. As more frames are used the stability of the resultant background increases. [97]

We can develop a median filter in order to do background subtraction of our channel from each frame. This allows us to find the mean image because the moving pixels, in this case cells, will be disregarded. This is an important technique for isolating moving, or active, pixels in an image from stationary ones. In this case it allows us to isolate moving cells in the channel.

$$\boldsymbol{B(x,y,t) = median(I(x,y,t-i))} \quad \textbf{(35)}$$

$$\boldsymbol{|I(x,y,t) - median(I(x,y,t-i))| > Th \; where \; i \in (0,\dots,n-1)} \quad \textbf{(36)}$$

where Th is some defined threshold value, i is each image, B is your background, and x,y,t refers to your coordinates in space and time.

We can also develop a mean filter. This is handy for visually finding the mean position of all movement in the channel.

$$\boldsymbol{B(x,y,t) = \frac{1}{n}\sum_{i=0}^{n-1} I(x,y,t-i)} \quad \textbf{(37)}$$

$$\boldsymbol{|I(x,y,t) - \frac{1}{n}\sum_{i=0}^{n-1} I(x,y,t-i)| > Th} \quad \textbf{(38)}$$

where n refers to the previous n frames.

4.2.2 Canny Edge Detection

Canny edge detection is a multi-stage edge detection algorithm applied to a grayscale image [98-100]. It uses a high threshold to start an edge and a low threshold to continue an edge in order to detect areas where pixel brightness sharply changes. It is used for detecting the regions in an image where the pixel brightness sharply changes. We can use it in the developed script for refining the image so that only the dominant features remain.

It works by following the steps below.

1. Smoothing by Gaussian convolution
2. For each gradient find magnitude and orientation
3. Perform non-maximal suppression (reduce all "edges" to the width of a single pixel)
4. Perform hysteresis (establish a high threshold to start and edge and a low threshold to continue it)

4.2.3 Hough Transform

In order to search through an image for specific shapes we can use the Hough Transform [101, 102]. The Hough Transform is an algorithm patented by Paul Hough in 1962 [103]. It is a method for detecting curves in an image by carrying out a voting procedure in parameter space where object candidates are counted as local maxima in an accumulator space [102]. The technique has also been expanded to detect arbitrary shapes [101].

The first shape we can use the Hough transform to detect are lines. By finding lines in the image we will be able to automatically detect the microchannel.

We can begin by recalling the slope-intercept equation for a line as

$$\boldsymbol{y = mx + b.} \quad \textbf{(39)}$$

In the case of vertical lines the $\boldsymbol{m}$ value will reach infinity which is not a value that a computer can process.

So instead we can transform the equation for the shape we are looking for into Hough space. Now each line is represented by a distance variable which is the distance of a line running from the origin to tangentially intercept our line and the angle at which that intercept occurs.

$$\boldsymbol{y = \left(-\frac{\cos\theta}{\sin\theta}\right)x + \left(\frac{r}{\sin\theta}\right)} \quad \textbf{(40)}$$

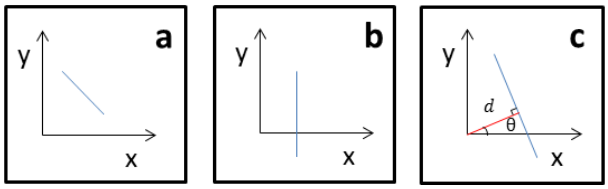

Figure 12: (a) shows a line in Cartesian coordinate space. (b) shows the case where using the slope-intercept equation will result in an infinity value that the computer is not able to process. (c) the line can then by represented in Hough space as a distance and an angle.

The way this practically works in an image is that for each edge detected, each pixel in the image, we know the distance from that edge from the origin but not the angle. We can therefore represent it as having all angles as a sin wave. Another point in the same line area we can represent the same way. The area where the two sin waves overlap yields the common angle. Each point that results in a specific angle counts as a vote for a line. We can then find the line with the most points, or the most votes, by taking the local maxima in the matrix used to accumulate and store votes.

We can also use the Hough transform to find all circles in the image. This time instead of using the equation for a line we can use the equation for a circle as cells are circular.

We can begin by recalling the equation for a circle as

$$(x_i - a)^2 + (y_i - b)^2 = r^2 \quad (41)$$

where the center of the circle is the coordinates (a,b) with radius r.

The Hough Transform, for every edge pixel (x,y), every possible radius value r, and every possible gradient direction θ will solve the following three equations

$$a = x - r\cos(\theta) \quad (42)$$

$$b = y + r\sin(\theta) \quad (43)$$

$$H[a, b, r] += 1 \quad (44)$$

Voting in the Hough Transform requires a good grid and discretization choice. It is a good choice as it processes all points independently, meaning that occlusions have very minimal impact. It can encounter challenges with complexity however.

4.2.4 Active Contours

There are many different algorithms for capturing an objects shape. One of the most elegant is called active contours. It is also referred to as snakes, deformable contours, or elastic band. Active contours is a powerful approach for finding object boundaries. It minimizes an external force called gradient vector flow (GVF) to move the contour into the boundary concavity [104-106]. The approach, in addition to being widely applied to computer vision applications, has been applied to tracking motile cells [107] and segmenting migrating cells for doing cell-based drug testing [108].

The idea behind the technique is to initialize a contour model near the desired object and then evolve the contour to exactly fit the object boundary. The most pertinent difference between this technique and the Hough Transform is that the Hough Transform in a single voting pass can detect multiple instances of an object whereas active contours in one optimization pass can fit a single contour and must be iteratively adjusted. The main components to consider are representation of the contours and definition and minimization of the energy function. We can begin by defining a set of 2D point positions for discrete representation of the contour as

$$\boldsymbol{v_i = (x_i, y_i), for\ i = 0, 1, \ldots n-1} \quad \textbf{(45)}$$

We then iteratively have the option to move each vertex to another location (or state) based on the energy function which we can define as

$$\boldsymbol{E_{total} = E_{internal} + \gamma E_{external}} \quad \textbf{(46)}$$

where delta and $\boldsymbol{\gamma}$ are weights on the internal and external energies. The internal energy ($E_{internal}$) encourages prior shape preference such as smoothness, elasticity, and a particular known shape, and the external energy ($E_{external}$) encourages contour fit on areas with edges. We can write out the external energy, the derivatives relative to position, for the whole curve as

$$\boldsymbol{E_{external} = -\sum_{i=0}^{n-1} |G_x(x_i, y_i)|^2 + |G_x(x_i, y_i)|^2} \quad \textbf{(47)}$$

$$\boldsymbol{E_{internal} = -\sum_{i=0}^{n-1} \alpha ||(v_{i+1} - v_i)||^2 + \beta ||(v_{i+1} - 2v_i + v_{i-1})||^2} \quad \textbf{(48)}$$

We can use the above to find the below equations to compare curvature

$$\boldsymbol{E_{curvature}(v_i) = ||(v_{i+1} - 2v_i + v_{i-1})||^2 = (x_{i+1} - 2x_i + x_{i-1})^2 + (y_{i+1} - 2y_i + y_{i-1})^2} \quad \textbf{(49)}$$

We can use dynamic programming to minimize the energy function. We start by rewriting them as a sum of pair-wise interaction potentials as

$$\boldsymbol{E_{total}(v_1, \ldots, v_n) = \sum_{i=1}^{n-1} E_i(v_i, v_{i+1})} \quad \textbf{(50)}$$

Rewriting the above we get

$$\boldsymbol{E_{total}(v_1, \ldots, v_n) = E_1(v_1, v_2) + E_2(v_2, v_3) + \cdots + E_{n-1}(v_{n-1}, v_n)} \quad \textbf{(51)}$$

where $\boldsymbol{E_i(v_i, v_{i+1}) = -||G(v_i)||^2 + \alpha ||v_{i+1} - v_i||^2}$

For a closed loop we introduce an additional term into the total energy equation.

$$\boldsymbol{E_{total}(v_1, \ldots, v_n) = E_1(v_1, v_2) + E_2(v_2, v_3) + \cdots + E_{n-1}(v_{n-1}, v_n) + E_n(v_n, v_1)} \quad \textbf{(52)}$$

We can then apply the Viterbi algorithm as described in [109] to iteratively determine the optimum position of the predecessor for each current possible position of self.

4.2.5 Nearest Neighbors

There are many different approaches for performing dynamic tracking. One of these is to use nearest neighbor [110]. It finds the closest measure to the predicted location [111] [112]. It is sometimes referred to as the Mahalanobis distance. It can be descried as

$$\boldsymbol{D(h_1, h_2) = \sqrt{\sum_{i=1}^{d} \frac{(h_1(i) - h_{2(i)})^2}{\sigma_i^2}}} \quad \textbf{(53)}$$

where D is our distance measure, h_1, h_2 refer to the coordinate space the value is in, σ_i is the standard deviation over the sample set.

4.2.6 Kalman Filter

Another approach for performing dynamic tracking is to use a Kalman filter, where the previous motion of a particle is recorded and used to estimate a resultant position. We can use image measurements to estimate and predict the motion of an object and find an object's motion pattern. It manages this by going through a recursive solution of the least-squares method [113].

The camera must be stationary in order for this to work. We can begin by developing a linear system dynamics model to describe a priori knowledge and represent the evolution of a state over time

$$x_t \sim N(Dx_{t-1}; \Sigma_d \quad) \tag{54}$$

We can also develop the measurement model which represents the noisy measurement of the state at every time step.

$$y_t \sim N(Mx_t; \Sigma_m) \tag{55}$$

We can then perform updates to the model for each cycle using a Kalman filter. This is best applied for tracking linear dynamics models with Gaussian noise and Gaussian predictions and corrections state distributions. We start by estimating the predicted distribution for the next state.

$$P(X_t | y_0, \dots, y_{t-1}) = N(\mu_t^-, (\sigma_t^-)^2) \tag{56}$$

where μ_t^- is the mean and $(\sigma_t^-)^2$ is the variance. We can then update the mean and the variance

$$\mu_t^- = d\mu_{t-1}^+ \tag{57}$$

$$(\sigma_t^-)^2 = \sigma_d^2 + (d\sigma_{t-1}^+)^2 \tag{58}$$

We can then update the distribution given the latest measurements by updating the mean and the variance as

$$\mu_t^+ = \frac{\mu_t^- \sigma_m^2 + m y_t (\sigma_t^-)^2}{\sigma_m^2 + m^2 (\sigma_t^-)^2} \tag{59}$$

$$(\sigma_t^+)^2 = \frac{\sigma_m^2 (\sigma_t^-)^2}{\sigma_m^2 + m^2 (\sigma_t^-)^2} \tag{60}$$

It is worth noting that if there is no prediction uncertainty $((\sigma_t^-)^2 = 0$ than the measurement is ignored and if there is no measurement uncertainty $\sigma_m = 0$ than the prediction is ignored.

4.3 Development of the First Generation Cell Tracking and Analysis Script Using Computer Vision Tools

A script had previously been developed in-house however it relied upon counting pixels as they crossed a line [114]. That approach was highly susceptible to variations in cell size and introduces inaccuracy into the results. A cell tracking script was developed in MATLAB (Mathworks) in order to improve accuracy and reliability. Specifically the first generation cell tracking software detected whole individual cells in order to perform analysis, which yields greater accuracy than the prior approach. It was developed to be capable of analyzing video results by tracking cell motion through a channel and calculated the average cell size, path, and position. The performance was quantified by comparing the first generation software to the original script.

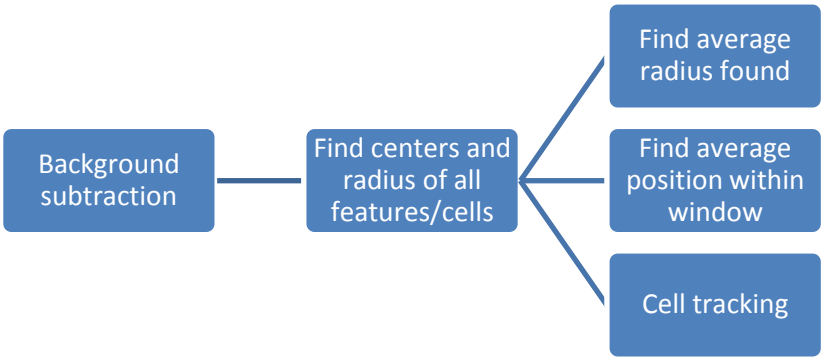

Figure 13: Schematic outline of the first generation implemented code after a cell video has been loaded.

Initially, heightening the contrast in pixel intensity was used for detecting the cells/features in the channel however this approach generated artifacts that the cell detection script would mistakenly recognize. The solution was to perform median background subtraction across all loaded frames to isolate the cells/features in the channel. Once the background image was determined it was converted to a binary image. This approach eliminated background noise, greatly improving the results from the circle finding function as shown below.

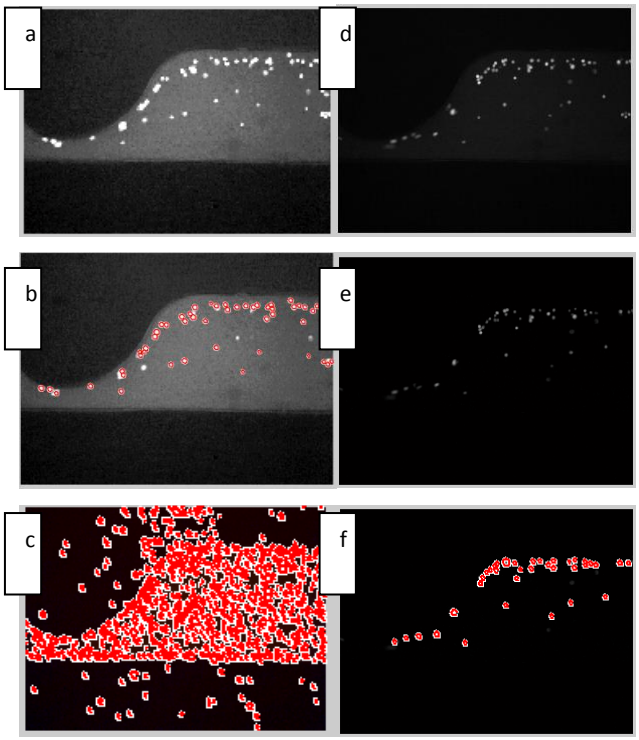

Figure 14: The results using a heightened contrast on the left. (a) heightened contrast image, (b) typical detected result, (c) an extreme failure case example of detected artifacts. Right shows the consistent results from using background subtraction prior to cell detection. (d) the raw black and white

image, (e) the results after the background has been subtracted and the features have been isolated, and (f) the detected cell circles.

The cell detection script uses the Hough Transform algorithm in order to find the cells/features. SIFT features were considered for detecting the cells however not chosen because cells spin as they move through the channel therefore there is no guarantee that the same features would be present between frames. As cells are highly circular the Hough Transform detects the cells and outputs the centers for all detected features/cells and the detected radius size (in microns). Because the videos are taken using a fluorescent microscope at 10X magnification it is trivial to convert from pixels to microns. The microscope is first calibrated and then used to measure a known distance on the screen. That distance provides the base to convert between pixels and microns.

Once the centers and radius information have been obtained there are several operations that are performed. The radii of all detected cells were recorded and the mean value and standard deviation were calculated. The positions of all cell centers that pass through a predetermined window were recorded and used to calculate the average cell position. The window was determined using prior knowledge about the system. This data is used to quantify cell motion and determine the amount of DEP force the cells experienced as well as giving critical characterization information. This was plotted over the mean image across all frames.

The locations of the cell centers for each frame were used to develop a cell tracking script. The similarity of the cells makes it impossible to used SIFT features, or other feature detection algorithms, for tracking cells. The cell tracking script relied on a "nearest neighbor" approach. The Euclidean distance between cell centers between two adjacent frames was used to determine the nearest neighbor. To visualize the results the frames were translated into the RGB color space where the previous frame was the red channel, and the next frame was the blue channel. The connections between frames were plotted as blue lines.

One challenge using nearest neighbor was that if the match wasn't detected (occlusions, etc.) the script would take the next nearest neighbor is, without regard to practicality. Implementing a threshold greatly improved the result. It was found that in any given frame less than 5% would be thresholded.

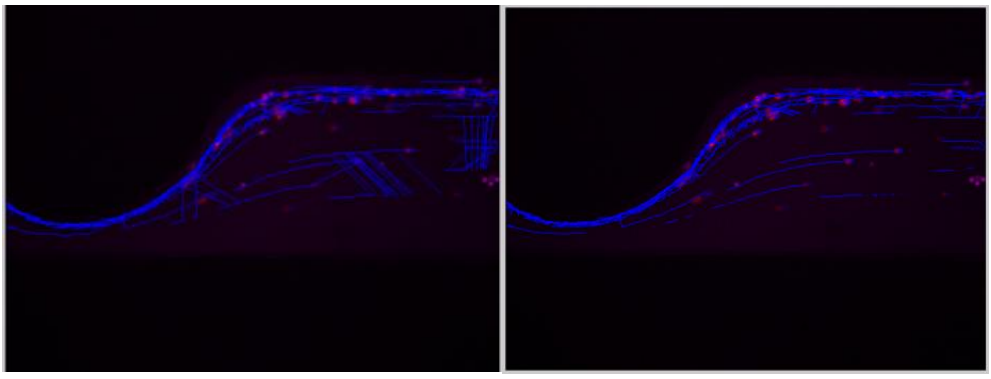

Figure 15: Visualization of the cell tracker script. When movement is very small the blue and the red will be overlaid, producing a purple coloring. Left shows implementation without threshold, right shows the improvement from adding a threshold distance.

4.4 Comparison of First Generation Cell Tracking and Analysis Script to Original Script Baseline

The performance of the first generation cell tracking and analysis script was quantified by evaluating each step in the approach. It was evaluated by establishing the elimination accuracy of background subtraction, cell size accuracy relative to biological data, and counting the number of missed tracks in the cell tracking script.

For the following figures a testing set of 100 frames was used. The video was acquired using MOSE TIC's at 200 Vrms and 40 kHz, meaning that the cells should be experiencing a positive DEP force pushing them towards the top of the microchannel. The flow rate was constant at 10 μL/hr.

The background subtraction script, using median pixel intensity across all 100 frames approach, performed well. This can be evaluated by measuring the number of cells it was able to remove compared to the number that it failed at removing. The background performed better at removing moving cells and isolating only the background as the number of input frames was increased, resulting in elimination of 83.3% of the moving objects.

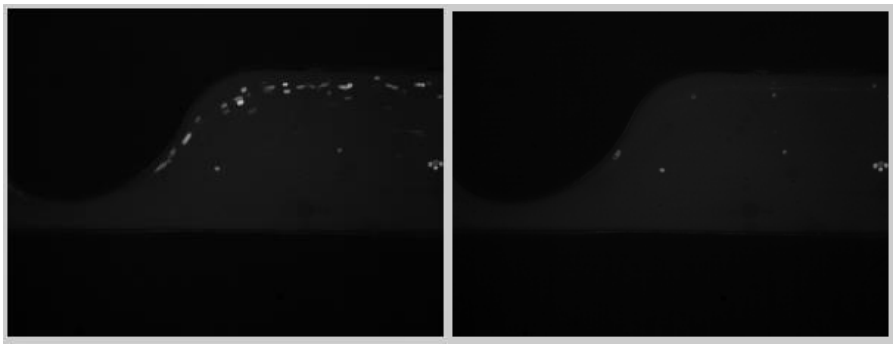

Figure 16: Background image using 10 frames shown on left, 100 frames shown on right. The elimination accuracy increased from 48.3% to 83.3%.

A Vicell machine (*Beckman Coulter*) was used to perform a baseline measurement prior to the video being taken. Vicell relies upon similar image measurements so its results, while the only other size measurement available, may not be representative of ground truth.

The cell size was found to be 18.47 microns. This yields an analysis error of 0.784 to 1.2156 microns, or within 20%, which is reasonable for biological data.

Table 2: Cell measurements taken using the video. Results are consistent when using different total number and skipped frame combinations.

Nth frame, X total frames	Average Diameter	Standard Deviation
N = 1, X = 10	19.2540	0.1130
N = 1, X = 100	19.6856	0.2078
N = 10, X = 10	19.8640	0.3078
N = 10, X = 100	19.4895	0.2355

The number of missed tracks were counted for a total of 5 pair frames. The accuracy of the matches was found to vary between 68.1% and 90.1% for an average of 80.6% accuracy. The greatest contributor

to the range in accuracy was the amount of movement between frame pairs. If the cells move more quickly through the channel, due to variations in the pumping speed, the distance the cell moves will be greater and it will be more difficult for the script to find an accurate match. The other issue was when two cells were very close. If two cells overlapped than the program would struggle with separating them.

Table 3: Results comparing cell tracking by hand versus the applied "nearest neighbor" approach.

Pairs in frame	Pairs missed	Accuracy
49	11	77.5%
52	5	90.1%
44	14	68.1%
49	7	85.7%
54	10	81.5%

The most successful measurement was cell trajectory and cell position.

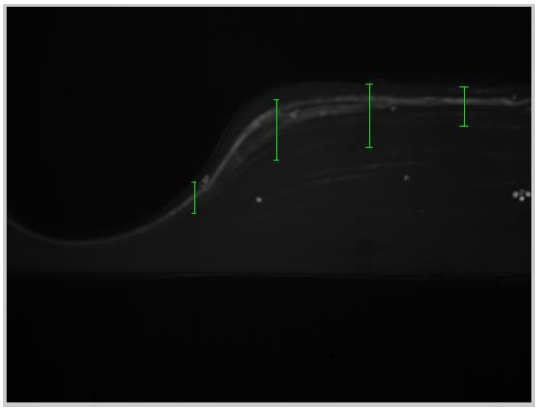

Figure 17: Calculated mean cell trajectory within a window between 700 and 760 pixels in the x direction plotted with standard deviation over the mean image of all frames that allows us to visualize the trajectory. In this case the mean position was (740,173) with a standard deviation of 41.5 along y. 503 cell centers were used to calculate.

The applied electric field induces a positive DEP response in the cells, pushing them towards the top of the channel. In Figure 6 the cell path has been overlaid to show that the cells are moving along the top of the channel. The position measurement also shows the mean cell path within the straight channel portion.

This script successfully quantified the position, size, and trajectory of the cells and showed that the cells were experiencing positive DEP pushing them to the top of the channel. This is important because it verifies that the cells are experiencing the positive DEP desired by the device and cell sorting would be

effective, meaning that this script can effectively be used to evaluate device performance and measure cell movement and morphology.

There are several assumptions that this script makes. The first is that the cells can be accurately represented as circles. We can make this assumption because cells contract into spheres when suspended in fluid. Another assumption is that all cells are moving at the same velocity and that the velocity is constant. This is a reasonable starting assumption as the micropump is fairly consistent.

4.5 Development of the Second Generation cell tracking and analysis script using Computer Vision tools

The second generation cell tracking and analysis script was an extension of the first generation. Several elements remained the same, background subtraction and use of the Hough Transform for cell detection and tracking. In order to increase functionality and applicability the script was expanded to be able to measure cell circularity using Active Contours, automatically detect the channel, use single step Kalman filter for tracking cells, and be able to perform dual analysis on two color channels (red and green). Red and green was chosen as those are the colors of the fluorescent dyes available for staining the cells.

There were many tools that were used in order to create this script.

Background subtraction is very important in order to isolate and detect moving objects, in our case biological cells flowing through a microchannel. Techniques can range from simplistic to very complex with varying computational requirements. A temporal median filter, where the median values across some number of frames is taken, has the advantage of running very quickly and provides an adequate background image as long as enough frames are used. As more frames are used the stability of the resultant background image increases. [97]

There are many different approaches for performing dynamic tracking. One of these is to use nearest neighbor, such as the one implemented in [110]. Another approach is to use a Kalman filter, where the motion of a particle is measured and used to predict future positions [113].

The Hough Transform is an algorithm patented by Paul Hough in 1962 [103]. It is a voting method for detecting specific shapes, most commonly lines or circles, where object candidates are counted and added to an accumulator space and the local maxima is used to find the bin with the most votes. The technique has also been expanded to detect arbitrary shapes [101].

Determining the circularity of an object can be very challenging. Active Contours is a powerful approach for finding object boundaries. It works by initializing a contour model near the desired object and then iteratively evolving the contour to exactly fit the object boundary. It does this by minimizing a defined energy function (Gradient Vector Flow is popular, where the field is computed as a spatial diffusion of the gradient of an edge map derived from the image). The internal energy encourages prior shape preference such as smoothness, elasticity, and a particular known shape, and the external energy encourages contour fit on areas with edges. The approach, in addition to being widely applied to computer vision applications has been applied to tracking motile cells [107] and segmenting migrating cells for doing cell-based drug testing [108]. The most pertinent difference between this technique and the Hough Transform is that the Hough Transform in a single voting pass can detect multiple instances of an object whereas Active Contours in one optimization pass can fit a single contour and must be iteratively adjusted.

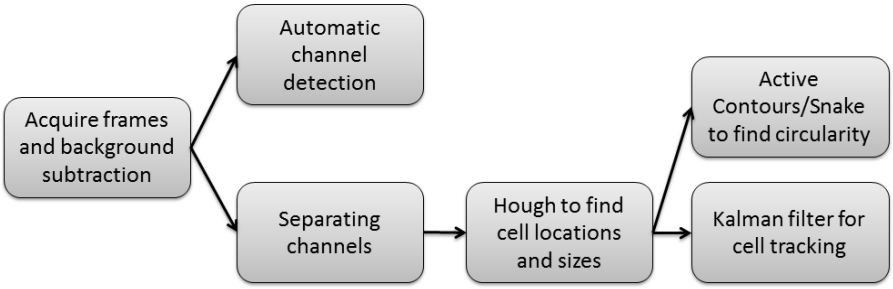

Figure 18: Schematic outline of the second generation implemented code after a cell video has been loaded.

A script was written in MATLAB (Mathworks). MATLAB was chosen for its analytical power and computer vision support. The above algorithms were applied to build the script.

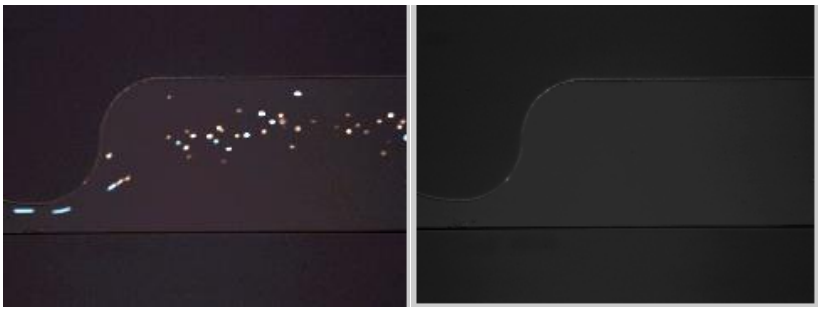

Figure 19: One, of 20 randomly selected, input frame used for calculating the background image using a median filter on left and resultant background image on right.

The script begins by reading in a video of cells taken at 10x magnification and performing background subtraction by applying a median filter across each RGB channel. This allows us to find the background image because the moving pixels, in this case cells, will be disregarded. The found background image is then subtracted from every frame to isolate the moving cells.

The channel is automatically detected by performing the Hough transform to find all lines in an image after canny edge detection has been performed. In particular it finds the top 20 lines that are detected and finds those lines that are parallel and a certain distance apart, set using the known width of the microchannel.

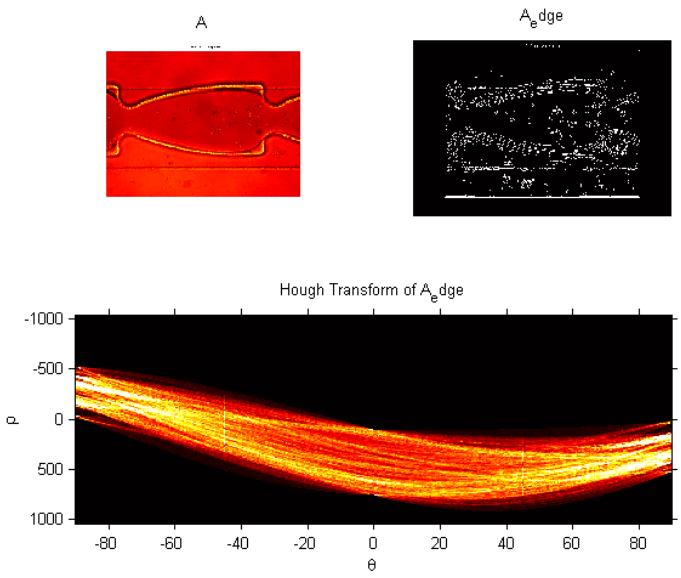

Figure 20: Input image top left, image after canny edge detection top right, and Hough transform of all lines in the image on the bottom.

The video is then separated into its red and green channels. Because the cells are fairly similar in color, meaning that the cells that have been dyed red do show up on the green RGB channel, simply separating the RGB channels isn't sophisticated enough to separate the cells. Instead the cell colors are separated by comparing pixel values. Those pixel values where the red RGB channel has a higher value than the green RGB channel are set to the red channel image, and vice versa.

Once the red channel images and the green channel images were determined they were converted to a binary image to threshold the image. This also had the advantage of removing from analysis cells/features which had a low intensity, which indicates non-viable cells.

Those individual channels are run through the Hough Transform to detect circles to find the cell locations and sizes. Once the centers and radius information have been obtained the average cell size, radius, and standard deviation for both channels are calculated and the number of cells that went into making those calculations are recorded.

The positions of all cell centers that pass through evenly spaced windows in the image were recorded and used to calculate the average cell position. This data allows us to determine the amount of DEP force the cells experienced and gives us critical characterization information. This was plotted over the mean image across all frames.

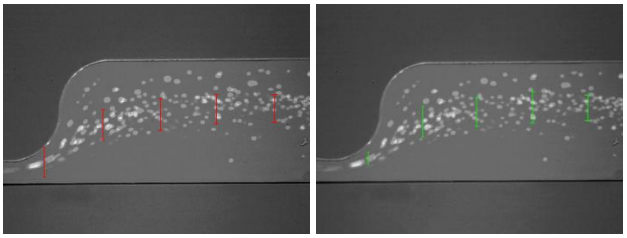

Figure 21: Calculated mean cell trajectory with evenly spaced windows and the standard deviation. Red channel, left, and the green channel on right.

Cell circularity was calculated by using the cell locations found by the Hough Transform to initialize the Active Contours script. 50 iterations per cell location were used to minimize the energy function.

The first generation script found the cell locations using nearest neighbor. It ran into problems with high cell densities and fast fluid flow rates. Dynamics were incorporated into tracking in order to improve tracking accuracy. Those locations found using Hough were used to developed a single step Kalman filter for tracking cells moving through the channel. To visualize the results the frames were translated into the RGB color space where the previous frame was the red channel, and the next frame was the blue channel. The connections between frames were plotted as blue lines.

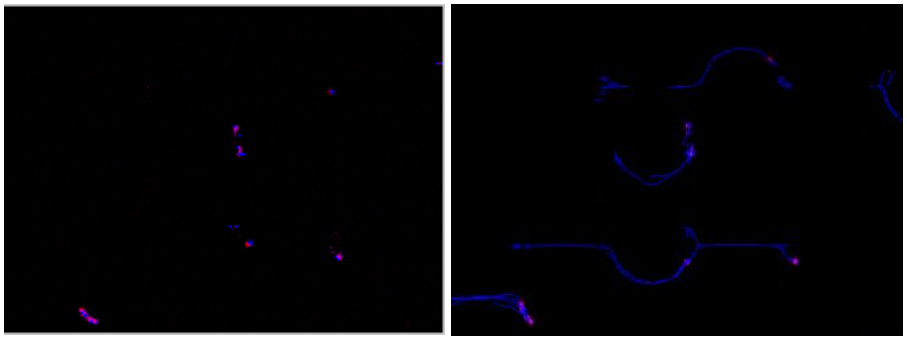

Figure 22: The Kalman filter worked on more complicated device geometries where the trajectory of the cells through the channel was less uniform such as a device with insulating posts in the channel. Left shows a match between two frames, right shows the resultant trajectory image.

4.6 Comparison of Second Generation Cell Tracking and Analysis Script to Baseline and Previous Work

For the following figures several testing videos with different geometries were used in order to illustrate the robustness of the newly developed script.

The background subtraction script using 20 randomly chosen frames performed well at removing all moving pixels. This result can be used to show how randomness helps the median filter because random frames have a low degree of correlation and ultimately result in better moving pixel elimination than using consecutive frames which have a higher degree of correlation.

The automatic channel detection script did a good job finding the main cell channel which always has a characteristic shape of two parallel lines that are a known distance apart. Performing Canny edge detection prior to the extraction of Hough lines was found to improve performance.

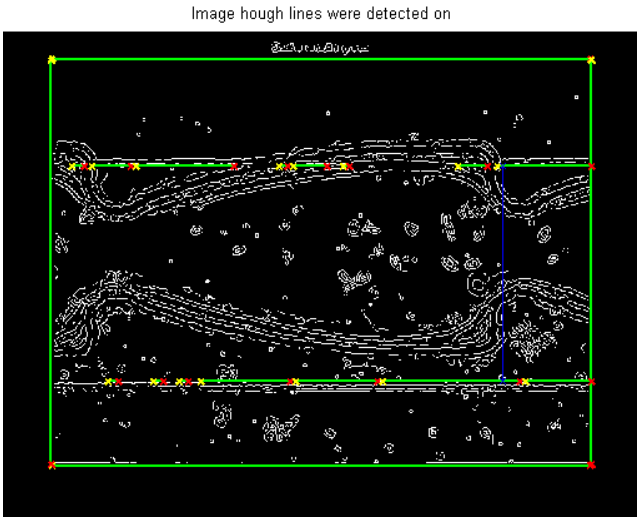

Figure 23: Example showing good performance of the automatic channel detection script. Green lines show the top 20 detected lines using Hough. Blue shows the ultimate detection of the channel.

The automatic channel detection script is sensitive to its presets and to debris in the channel. Therefore it is necessary to input the correct channel width requirements and for the background image to be sufficiently clean.

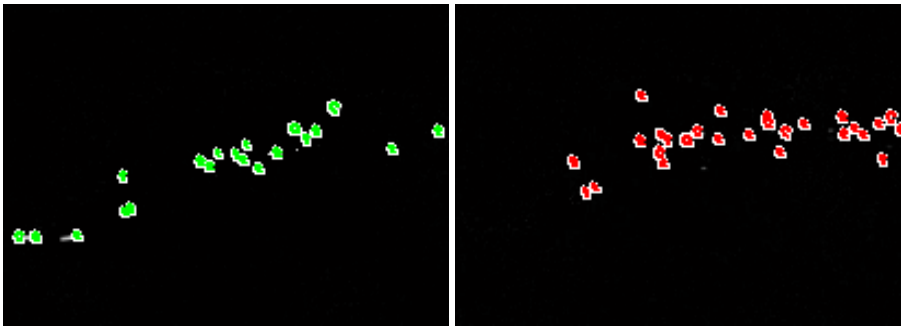

Figure 24: Images showing successful channel separation between the red and green channels which are two different cell lines dyed with red and green fluorescent dyes. The overlaid circles are the detected cells using the Hough Transform in Matlab.

A Vicell machine (*Beckman Coulter*) was used to perform a size and circularity measurement baseline on the cell lines used. The cell radius for the red channel was found to be 9.235 microns and 8.51 microns for the green channel. This yields an analysis error of 10.9% and 20.0% respectively, which is reasonable for biological data.

Table 4: Cell measurements taken using the developed script and a commonly used biology technique.

Cell type	Measured radius size (um)	Actual radius size (um)
MOSE-FFL (red)	10.2484 +- 1.4325 (298 cells)	9.235 (10.9% error)
MOSE-FFL chemo res (green)	10.2159 +- 1.4398 (252 cells)	8.51 (20.0% error)

The circularity measurements were found to have a greater difference from the Vicell baseline. Using Vicell (Beckman Coulter) the circularity measurements for both channels was found to be 88%. The measured circularity, using Active Contours was 99% for the red channel and 95% for the green channel. This error may be because the chosen script that was implemented was very sensitive to initialization and the contour had a tendency to "walk away" from the boundary despite parameter optimization. An algorithm such as one by Chan-Vese [115] where initialization is not required could be used as a basis for implementation.

The higher circularity measurements could also be due to the cells actually becoming more circular as the Vicell measurements were taken directly after trypsinization of the cells and removal from the media while the measurements using the script were taken after the cells had been in DEP buffer for around an hour possibly due to osmotic swelling.

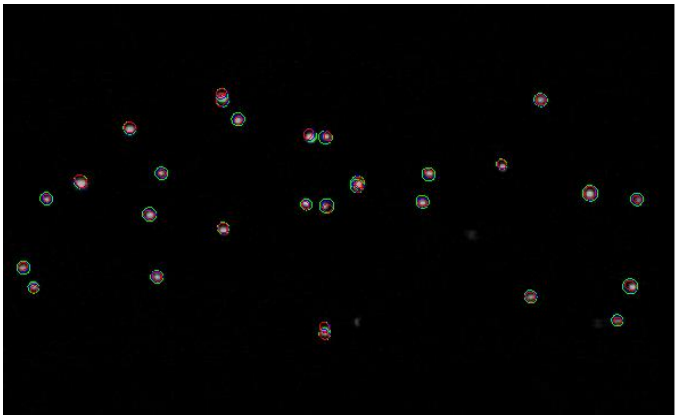

Figure 25: Results from implementation of active contours script on a frame with cells. The green lines show the initialized contour and the red line show the final contour.

Table 5: Results showing the circularity as measured by the developed script and a popular biology technique.

	MOSE-FFL (red)	MOSE-FFL chemo res (green)	Vicell measurement
Circularity	.9976	.9571	.88
Standard deviation	0.0021	0.0441	N/A
Number of cells	353	495	N/A

For 5 frames for each channel the correct pair matches and incorrect pair matches were recorded. Using the nearest neighbor approach the cell tracking script had an accuracy that varied between 68.1% to 90.1% with an average of 80.6%. The Kalman filter improved the accuracy to an average of 93%, a 13% improvement.

Table 6: Cell tracking results using the Kalman filter.

Red channel			**Green channel**		
Pairs in frame	**Pairs missed**	**Accuracy**	**Pairs in frame**	**Pairs missed**	**Accuracy**
14	1	92.8%	40	1	97.5%
14	0	100%	42	2	95.2%
13	1	92.3%	41	3	92.7%
15	0	100%	40	3	92.5%
15	2	86.7%	42	6	85.7%

It is worth noting that this script, while a huge improvement, does have some limitations. The largest of which is potential error due to the dilation step conducted in order to fill in miss-segmented cells.

This script has already been used to quantify performance and shows huge improvement over both the pre-existing script that had problems with inaccuracy and robustness and the first generation script that had limited scope. This is an important piece of analysis software not only because it allows for more accurate device performance evaluation and more robust experimental results but because it also moves cDEP towards a commercial technology where it would function as a critical component in an automated screening system.

4.7 Reanalysis of Data Using New Script

The original script only provided the average position measurement. The crossover frequency for the MOSE-L Cisplatin Resistant cells was 12.2 kHz and 18.75 kHz when measured using the pre-existing script. There is a significant difference between both measured values which shows the problem with the old analysis script and the lack of tools quantifying its measurement accuracy. The data was reanalyzed using the newly developed script and results are presented below.

Table 7: Results using the developed script.

	MOSE-L Cisplatin Resistant cells				
Frequency (kHz)	Control	10	12.5	15	15
Position (pixels)	315.2	309.0	383.39	390.3	390.2
Stdev (pixels)	55.1	64.7	42.8	48.0	47.9
Total cells	297	288	201	105	105
Number frames	50	50	50	50	50
Radius (µm)	10.1	9.8	9.7	9.8	9.7
Stdev (µm)	0.13	0.27	0.37	0.19	0.19

Reanalyzing the two experiments using the new scripts yields crossover frequencies of 10.4 kHz and 12.3 kHz for each set of experiments and additional morphological and statistics measurements. This results in an average of 11.3 kHz and a standard deviation of 1.34.

The measured values for the two experiments should be close in value and repeatable as the experimental procedure was the same for both sets. The lower standard deviation when using the newly presented script compared to the original shows an increase in precision. In addition the new script includes statistics (e.g. standard deviation for both position and size in addition to a total cell count) that lend validity to the results compared to the old script which was limited to only one output value.

Chapter 5: New Device Modelling, Fabrication, and Validation

5.1 Importance of Smart Sample Handling

Usually the first step before separating and sorting particles is to focus them [116]. Typically this is because separation is either determined based on vertical movement in a microchannel and having all cells start at the same location is critical, or because cells are being individually processed and it is important to have the cells in a single fluid line reaching the detection zone one at a time. Another added benefit is that focusing cells into a narrow beam means that the cells are all moving at the same rate. Flow in a microchannel is slower at the sides or the walls of the channels. Focusing cells in the center moves cells to a region where the flow rate is homogenous. Focusing also prevents the particles from sticking to or being absorbed by the microchannel walls [117].

In flow cytometry cells are analyzed by shining light at each individual cell and measuring the scattered light and fluorescent emissions at several different angles. This process is high speed, requiring a highly accurate single-file stream of focused cells [118]. Particle focusing can also be critical in continuous flow separation devices [119]. Typically this is achieved using hydrodynamic focusing [120]. Using microfluidic networks, because they are typically designed as single layer systems, typically fail at focusing the particles along the z axis. There has been significant work into developing 3D hydrodynamic focusing systems that would overcome these problems [121-124]. These systems still encounter challenges inherent to using fluid streams to focus particles such as multiple particles encountering the detection area at the same time, particles hitting the sensor at different heights, and issues with fabrication complexity.

Electrokinetics can also be used to focus cells [116, 125-128]. This can be done by either using electrokinetic sheath flows to focus particles by pinching the suspending medium [117], or by moving particles to an equilibrium position by applying an external force field (e.g. optical, acoustic, electrophoretic, or dielectrophoretic) [116].

Dielectrophoretic focusing involves creating electrode areas that constrict electric fields [116, 129-131]. The particles then move in order to align themselves within the field. In order to effectively manipulate particle positions the electric field needs to be sufficiently large and have a large enough gradient. Traditional DEP devices encounter issues with particle clogging and chip fouling. Because in traditional DEP devices the electrodes are in direct contact with the sample, challenges such as Joule heating, electrolysis, and delamination offer occur [131]. Many of these challenges can be resolved by designing a focusing device using cDEP.

In a microfluidic device fluid flow typically follows a parabolic profile where the flow is faster in the middle and slower on the sides where it comes in contact with the walls, ceiling, and bottom of the device [95]. This profile results from pressure gradients in the microchannel and is referred to as Poiseuille flow [132]. The interface between the fluid and the walls is what causes the difference in velocity and is material dependent [133]. Just focusing the cells to the middle 75% of the channel would make it so that the flow rate is more consistent across the cell sample.

5.2 Microfabrication

There are many ways to fabricate microfluidic devices. The defining features are cost and feature size/resolution.

Table 8: Summary of three different fabrication techniques. This shows the practical minimum feature size and largest aspect ratio that I was able to create.

Type of fabrication method	Minimum feature size	Largest aspect ratio achievable
SU-8	>40 microns	2:1
DRIE	>25 microns	12:1
3D printed	>150-200 microns	N/A

Three in-house procedures have been developed. The first is for creation of "single layered" devices where PDMS is poured over a master mold and allowed to cure. That layer is then carefully removed and bonded to glass. This technique is described in detail above and is a pre-existing technique [67, 134]. This technique is the best for very small resolution devices with large aspect ratios. For example the minimum resolution required for the single layer device was 25 microns. With a channel depth of 300 microns that results in a 12 to 1 ratio between channel height to width ratio.

The second in-house procedure is for creating so called "multilayer devices" where two or more master molds are used to create multiple layers that are aligned and bonded together. This was developed spring 2014 and has allowed for the creation of completely new device geometries. The development of this fabrication procedure is described in detail below. This technique is useful as a rapid prototyping method as, after receiving the transparency mask, it takes less than 1 hour to complete and is much less expensive than the DRIE technique. It is good for mid-range feature sizes over 40 microns and with a 2:1 aspect ratio.

The third and final procedure uses 3D printed structures as the master mold. This technique was a collaborated project and is described in detail below. This is another rapid fabrication technique. It however is only able to create relatively large features.

The above table summarizes the practical minimum feature size and largest aspect ratio I was able to fabricate during my studies.

5.3 Multilayer Microfluidic Device Fabrication Methods using SU-8

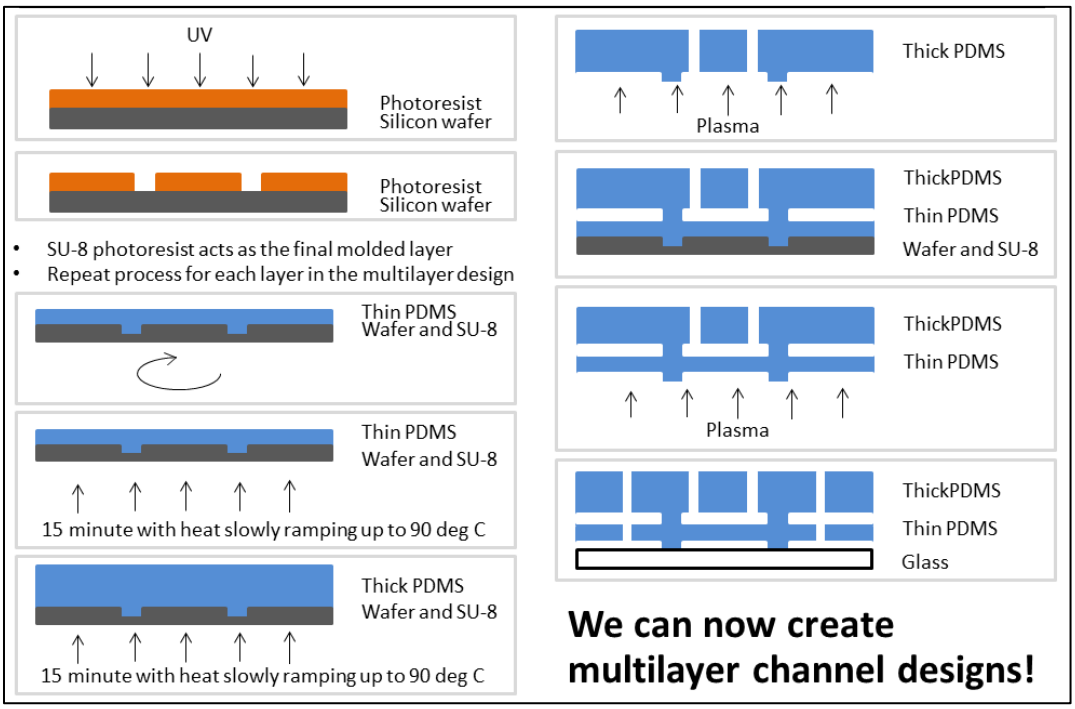

Figure 26: Overview of multilayer fabrication process using SU-8.

A mold is created for each layer in the device design. Silicon wafers are cleaned first with acetone, than isopropyl alcohol, and finally deionized water. SU-8 photoresist is spun and patterned by UV through a mask of laser printed ink on a transparency sheet. Once developed the wafer is inspected visually and silanized to improve PDMS removal and protect the SU-8 from chipping.

PDMS (Sylgard 184, Dow Corning) is mixed at a 10:1 base to curing agent ratio and degassed. ~2 g of PDMS is poured on the mold with the design for the bottom most layer and spun such that above the features only a thin membrane of PDMS exists. It is then cured on a hot plate for 5 minutes at 60 degrees, 5 minutes at 80 degrees, and 10 minutes at 90 degrees C.

PDMS is then poured onto the mold that consists of the topmost layer, using aluminum foil for containment, and cured at 100 degrees C for 45 minutes. The PDMS is peeled off and holes are punched (Howard Electronic Instruments). The cleaned PDMS is treated with air plasma for 6 minutes and then bonded with the top side of the PDMS that was spun and is still on the wafer. The combined PDMS layers are then carefully peeled from the wafer and holes are punched in order to interface with the channels on the bottom most layer. It is again treated with air plasma, for 2 minutes, and bonded to a clean glass slide.

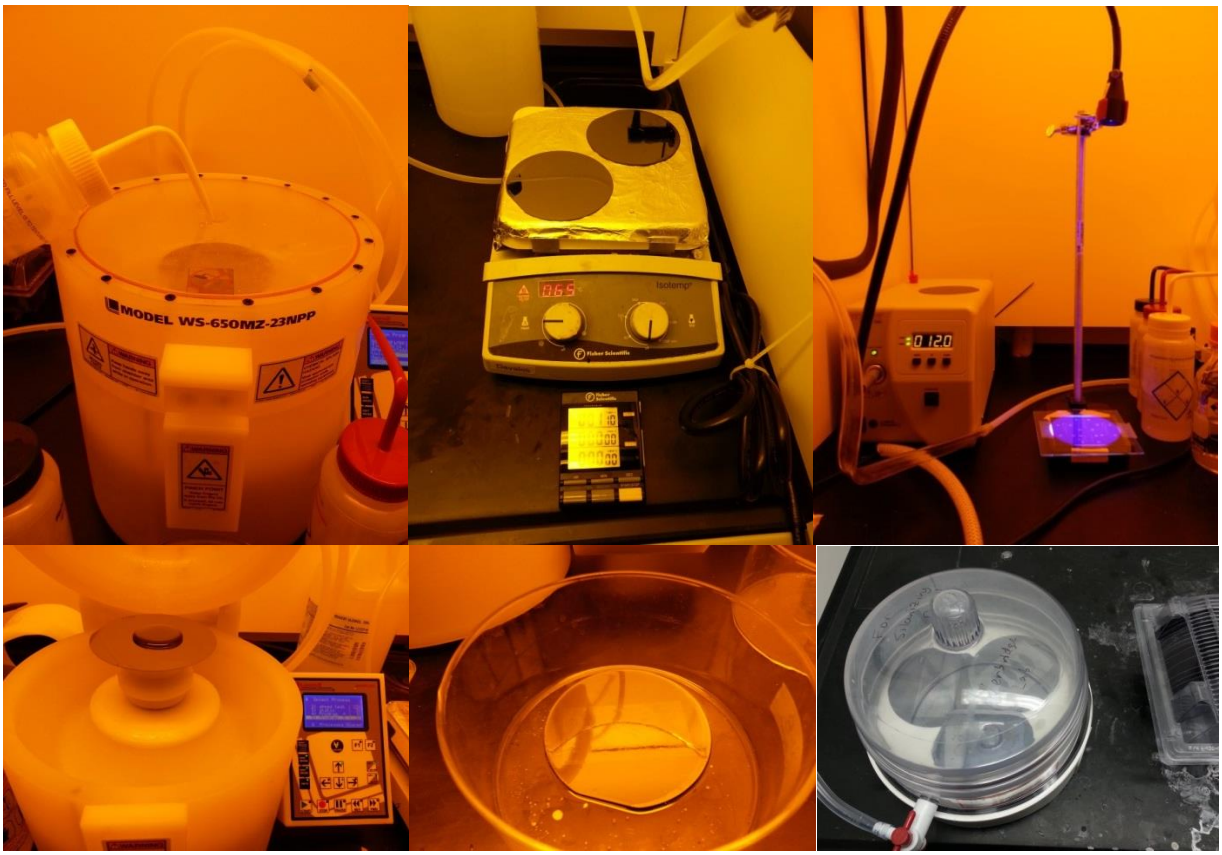

Figure 27: Images from the developed in-house setup.

An in-house setup was developed for greater efficiency and lower cost. The process was optimized. Initially problems were encountered with dimples forming at the interface of the silicon and the photoresist, this was found to be because of microscale debris particles that were present in the smaller bottle that the SU-8 was being transferred to. Using SU-8 directly from the main bottle and cleaning the cap thoroughly after each use solved this problem.

5.4 Methods and Design of 3D Printed Designs as Master Mold

The possibility of using 3D printed master molds was explored as a rapid fabrication technique that would be very user friendly and easy to use.

Most fabrication techniques are time consuming, expensive, have reliability issues, and machine down time is a very big problem. Exploring alternative fabrication techniques is a must, especially fabrication techniques that could bring us from the 2.5 dimension features offered by traditional microfabrication to the promise of truly 3D designs. A conventional stereolithography technique, a form of 3D printing, was tested.

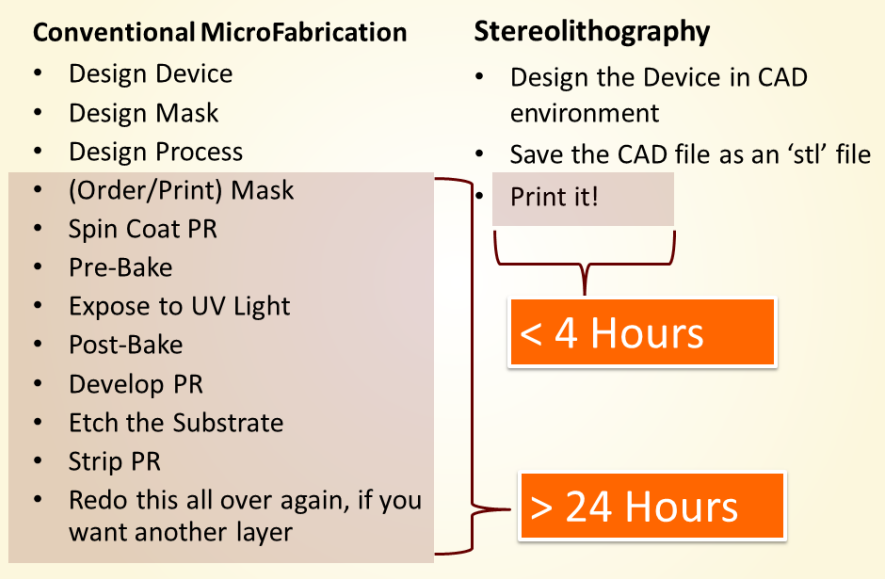

Figure 28: Comparison of traditional microfabrication process flow to the steps involved in stereolithography.

Advances in photopolymer solidification have reduced the minimum printable dimensions of 3-D printers [135]. Minimum feature sizes in micro-stereolithography have also improved, where printed structures with a characteristic dimension of a few microns can ideally be achieved [136]. These advances make it very tempting to substitute conventionally expensive and time consuming microfabrication techniques with the relatively simple stereolithographic process.

Stereolithography is an additive fabrication process where liquid photopolymer "resin" is deposited and solidified using an UV light. The entire fabrication process involves a layer by layer building process. To realize free standing structures a support material is used. The support material at the end of the deposition process can be removed using a water-jet or lye bath. A complete 3-D part is formed by this process [137].

A test board was designed to determine the resolution limits of the printer. Various structures, including 'L' channels, arrays and alignment markers were incorporated. The smallest pixel printed by the Objet Connex 350 measures to 42µm, thus the printer, ideally should generate structures in multiples of 42µm. This was the design parameter for choosing the dimensions of the straight channels and the 'L' channels as shown in figure 5.

Since, the print head moves along one direction, the resolution along the perpendicular axis can be expected to increase, thus two sets perpendicular of straight channels were printed. The features below the straight and 'L' channels are arrays of channels with varying dimensions and spacing. This tests the ability to print small features close to each other. Circular posts, triangular posts, and alignment markers of various dimensions were included to monitor pixilation from the printing process. The final test board incorporated both the positive and negative features with a z-directional extrude of $\pm 250 \mu m$. Figure 7 shows the 3-D. These structures were designed using AutoCAD and the 3-D model was generated using Solidworks.

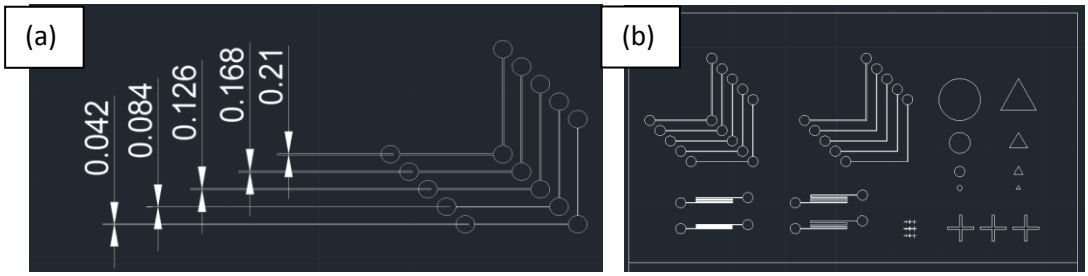

Figure 29: (a) Schematic showing the common dimensions on the test board. All dimensions mentioned in the schematic are in millimeter. (b) Complete design of the test board. This design was printed as a negative and also a positive substrate.

5.5 Exploration into Use of 3D Printed Designs as Master and Current Limitations

Our test board was printed in the highest resolution mode by the Objet Connex 350 3D printer and we were able to use that to create our PDMS structures. Because the test features had a very high aspect ratio it was difficult to actually remove the PDMS from the negative features. Therefore the SEM was used to image the positive features.

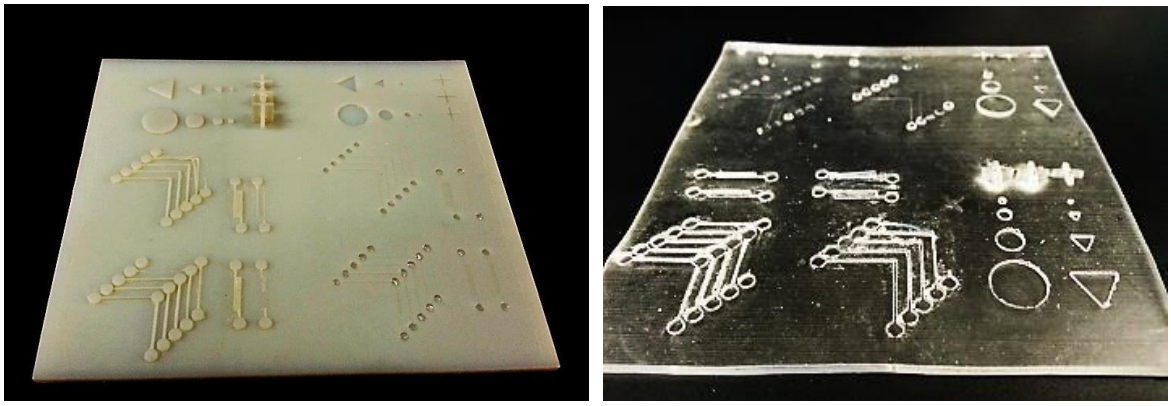

Figure 30: The fabricated test board (left) and resultant PDMS cast (right).

The SEM images reveal many potential challenges that deserve future inspection. Our goal was to explore the point at which features failed during printing. To this end we have been able to establish that in the y direction channels of 250 micron height are successful with widths above between 106.5 microns and 173.6 microns and in the x direction above around 196 microns.

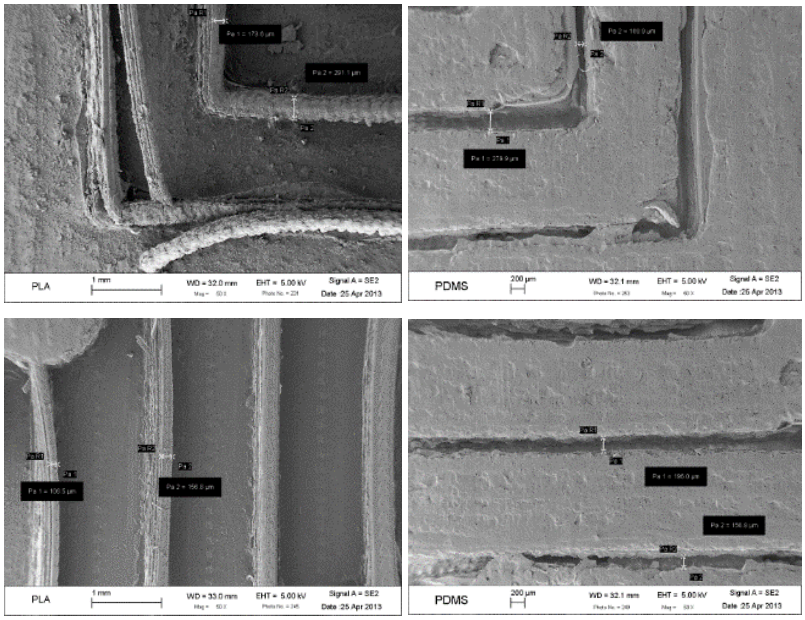

Figure 31: Top left shows the minimum widths for bends in a channel before failure (around 173.6 microns along y and top right 291.1 microns along x). Bottom left shows that in PLA the minimum feature size along the y axis was found to be 106.5 microns in PLA whereas bottom right shows the horizontal channels had a minimum printed width before failure of 196.0 microns.

At very high aspect ratios the layers began to separate, showing a point of failure at around 123 microns. This proved a challenge when curing the PDMS as the PLA layers would become embedded in the PDMS as it solidified and as the PDMS was removed it would detach as well.

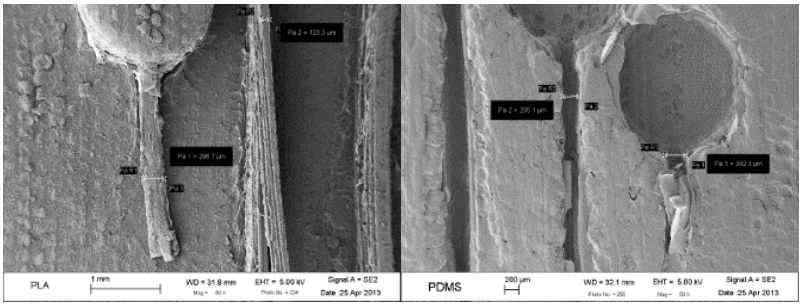

Figure 32: The high aspect ratio features would topple. Loose layers of PLA actually became embedded in the PDMS as it cured.

Lastly there were three main characteristics that were highly noticeable that affected surface roughness. The first is that the dot from the printing process remains as a visible artifact on the substrate. The second is that the surface roughness in the PLA master clearly translates to the PDMS mold. Third and last is that the surface roughness issues are not limited to the top surface but also affect the channel walls.

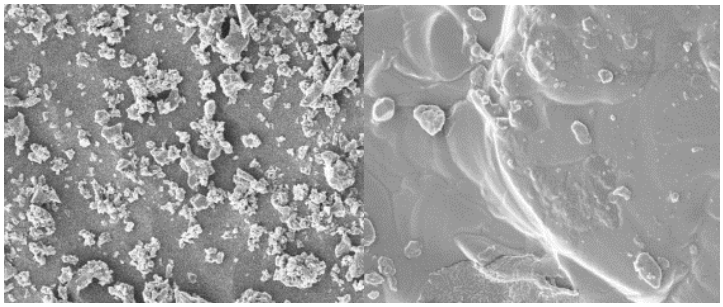

Figure 33: Comparison of the surface roughness on the PLA and the PDMS surface at 3000X magnification. Note how the surface roughness was transferred from the PLA master to the PDMS.

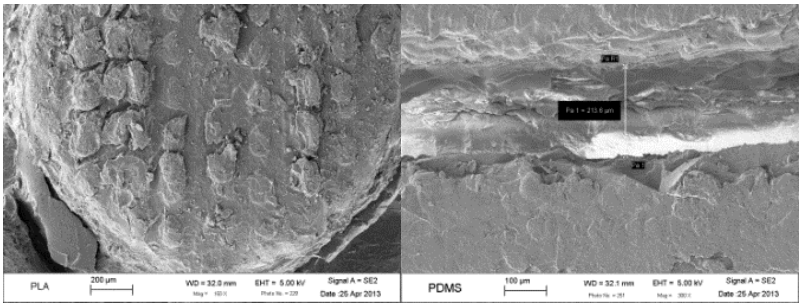

Figure 34: The appearance of the spherical surface features are a remnant from the printing process as shown on left. Each "dot" is one of the 42 micron initial droplets from the stereolithography machine. The surface roughness in a channel is shown at 300X magnification on right.

The most noticeable result from the SEM is the change in dimensions from the designed features to the actual printed dimensions.

Table 9: Change in dimensions from design to printing.

Design Dimension	Dimension in PLA	Dimension in PDMS
84 µm	123/105 µm	N/A
126 µm	156 µm	156 µm
168 µm	274 µm	196 µm
210 µm	319 µm	N/A

A PDMS cast of the positive features is used to test for surface roughness. Plasma bonding the PDMS substrate to a glass slide was found to have issues with leakage as shown in figure 16 (a). From the literature the same machine had between 3.8 microns (glossy) and 5.6 microns (mate) peak-to-valley average surface roughness [138]. This challenge was overcome by spin coating a 20 micron layer of PDMS onto a glass slide as an intermediate layer. The spin-coated PDMS prepolymer was cured at 100 °C for 5 to 7 min. The PDMS cast was applied to the half-cured PDMS intermediate layer and thermally bonded at 100 °C for an additional 5 to 7 min.

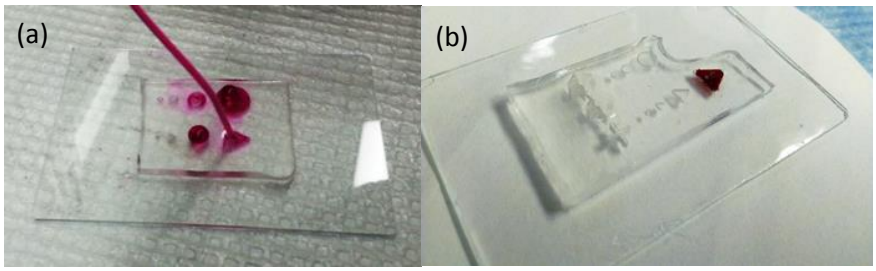

Figure 35: (a) shows the leakage issues with the finished prototype. (b) shows the increased performance after a thin layer of PDMS was added to the slide.

It can be concluded that at this time 3D printed masters are a viable option for devices with features over 156 µm and that issues with surface roughness can be overcome with an additional step where PDMS is spun. There are also chemical treatments that can be used to soften the surface of a 3D printed design and may have a similar effect.

5.6 Device Models Using Finite Element Analysis Software

5.6.1 Theory and Numerical Model Development of Modified Tesla Structures

In our cDEP system, loading the sample and controlling the original position of the cells is crucial in order to measure the motion of the cells in the electric field. One way to address this is to evenly distribute the cells across the entire channel by mixing them in the syringe. Over time, however, the cells will settle to a specific area in the channel and that settling of the cells will bias the system and effect the measurements. A more robust way to approach this problem is to mix the cells at the inlet of the device in order to continuously redistribute all cells across the channel. To this end a micromixer design was explored and modelled.

Micromixers are arguably the most important component of a microfluidic device, their ability to initiate rapid mixing is extremely crucial for chemical reactions to occur at low-Reynolds' number regimes. [139] More-often than not, the efficacy of the micromixer in a device is the biggest design constraint.

Although some of the earlier work on devices that involved mixing at low-Reynolds number regimes was attempted with simple geometries such as T-channels and Y-Channels [140]. Over the last few years several intricate designs including the 'twisted-pipe' configuration [141] and Modified-Tesla configurations [142] have become increasingly popular.

In particular, the modified-tesla structure, has an interesting consequence where the mixing efficiency improves with an increase in flow-rate. These structures promote the 'Coando Effect', the tendency of fluids to follow a surface [142]. This effect builds with an increase in flow-rate, thus improving mixing which is contrary to the intuition developed from T-channel mixers.

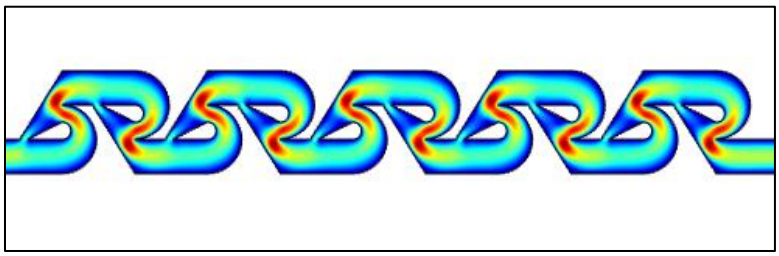

Figure 36: Hong et al. demonstrated an innovative, passive micromixer that uses the "Coanda effect," which produces transverse dispersion with two-dimensional modified Tesla structures. The Coanda effect, named after Henri-Marie Coanda, who first identified the effect in 1910, involves the tendency of fluids to follow a surface.

The modelling is based on a Comsol Multiphysics stationary study to analyze the concentration distribution at steady state. Since the Reynold's number is very small, usually around 1 in the micro channel.

$$\mathbf{Re} = \frac{\rho du}{\mu} = \frac{\textbf{initial forces}}{\textbf{viscous forces}} \cong \mathbf{1} \qquad \textbf{(61)}$$

The laminar flow model is used for velocity analysis along the channel. The transport of diluted species is used to model species diffusion. Physics-controlled meshing is used instead of user controlled meshing due to faster processing speed.

The modelling results show that mixing efficiency in the T channel is very low due to limited diffusion. Velocity change has minimal effect on mixing efficiency, however lower mixing efficiency can still be observed at the end of the T channel as shown in figure 9. At very small velocity about 0.0002m/s, the mixing enhanced and is able to see in Figure 8. But such low velocity is not desirable in a normal microfluidic channel.

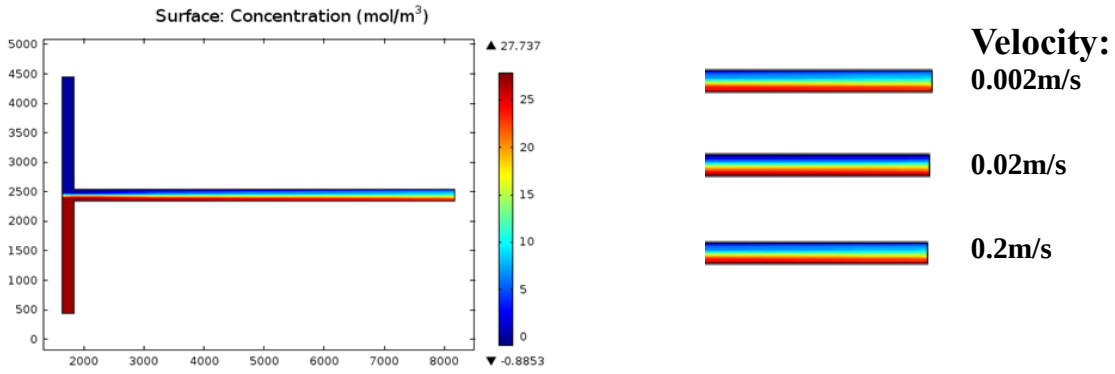

Figure 37: (a) The modelled mixing efficiency of the T-channel device. As the velocity increases, the mixing efficiency decreases a bit along the channel. (b) Zoomed in image of the velocity profile at the end of the T channel mixer.

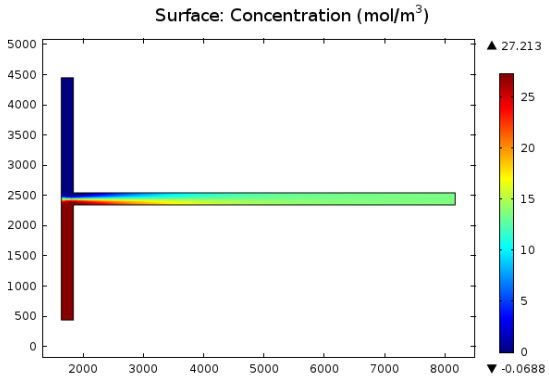

Figure 38: At very low velocities (0.0002m/s), mixing is enhanced significantly.

Compared to the low mixing efficiency of the T channel mixer, the modified Tesla Structure has a much higher efficiency. The mixing completed within three, two, and one Tesla structure units for 0.002m/s, 0.02m/s and 0.2m/s, respectively. This means the modified Tesla structure is more suitable for high velocity microdevices. The results are consistent with the literature [143].

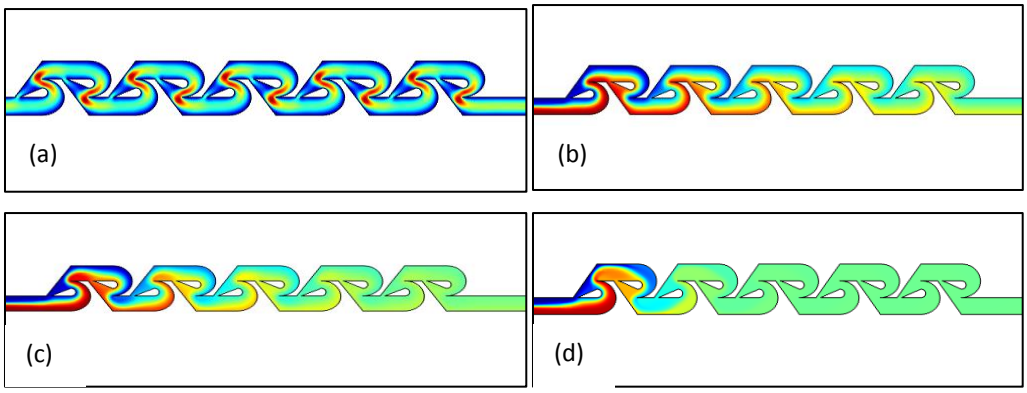

Figure 39: (a) shows the velocity profile of modified Tesla structures. The mixing happens at the narrow gap due to the significant geometry change. (b-d) show the mixing efficiency increasing when the velocity increases which is different from the T channel mixer. The velocities in (b) to (d) are 0.002m/s, 0.02m/s and 0.2m/s, respectively. The solution gets fully mixed with in three, two and one unit, respectively. The mixing efficiency of Tesla structure is much higher than that of T channel mixer.

5.6.2 2D Numerical Model of Electrodynamic Focusing Device

As mentioned above, distributing cells upon entry to the cDEP system is crucial in order to measure their movement from that position. Instead of mixing the cells so that they are evenly distributed across the entire channel another way to redistribute them is to focus them into a narrow band. While using DEP to focus cells has been explored before [116, 117, 129, 130], this is the first cDEP device design to focus cells.

A two dimensional geometry was created in AutoCAD (AutoCAD Mechanical 2010, Autodesk Inc.). The geometry was imported into Comsol Multiphysics (Version 4.3, COMSOL Inc). To model the electric field the AC/DC module was used (electric currents). Edges of the electrode channels were modeled as a uniform potential of 200 V or 0V. The regions of the model were set to represent

poly(dimethylsiloxane) (PDMS) (Sylgard 184, Dow Corning), phosphate buffer solution (PBS), or sample media. PDMS was modeled as having a conductivity of $0.83*10^{-12}$ S/m and a relative permeability of 2.65 as defined by data from the manufacturer. PBS was defined as having a conductivity of 1.4 S/m and a relative permeability of 80 from experimental measurements previously taken. The sample media was modeled as a sugar solution and assigned a conductivity of 100 µS/cm and relative permeability of 80 as found from previous experimental measurements. The flow at the inlet was set to 0.000056 m/s.

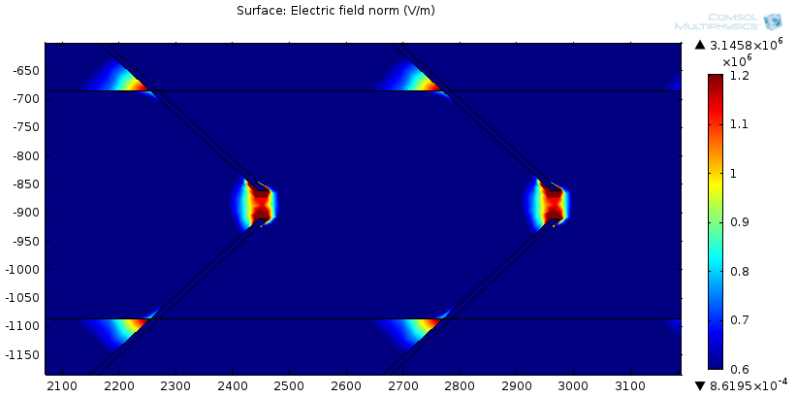

Figure 40: 2D finite element model from Comsol showing the electric field gradients.

The results from the model show that the electric field gradients are densest between the electrodes. In this design, in the frequency range where the CM factor is positive the particles will be attracted to the area between the posts and will be focused. The 2D model however doesn't take into account the height of the channel nor the thin insulating membrane separating the layer and therefore may not accurately reflect device performance.

5.6.3 3D Numerical Model of Electrodynamic Focusing Device

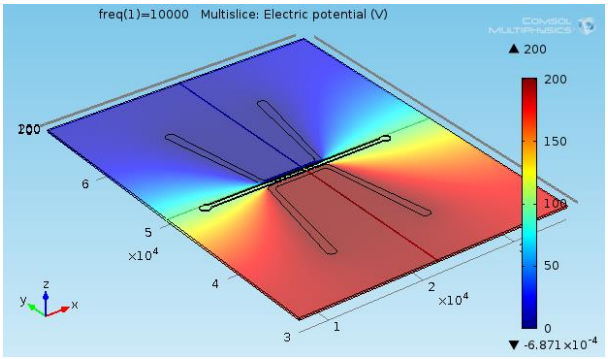

Figure 41: 3D model of the focusing device.

The 2D model was expanded to a 3D model in Comsol using the same modules and same characteristics. Two user defined meshes were compared. A user-defined, very fine tetrahedral mesh was used with the maximum element size of 1330, minimum element size 57, maximum element growth rate of 1.5, 0.2 resolution of curvature, and 0.5 resolution of narrow regions. It was refined until there was less

than a percent change in solution and produces smoother and more accurate results. We can see, again, that the cells will focus to the center of the channel.

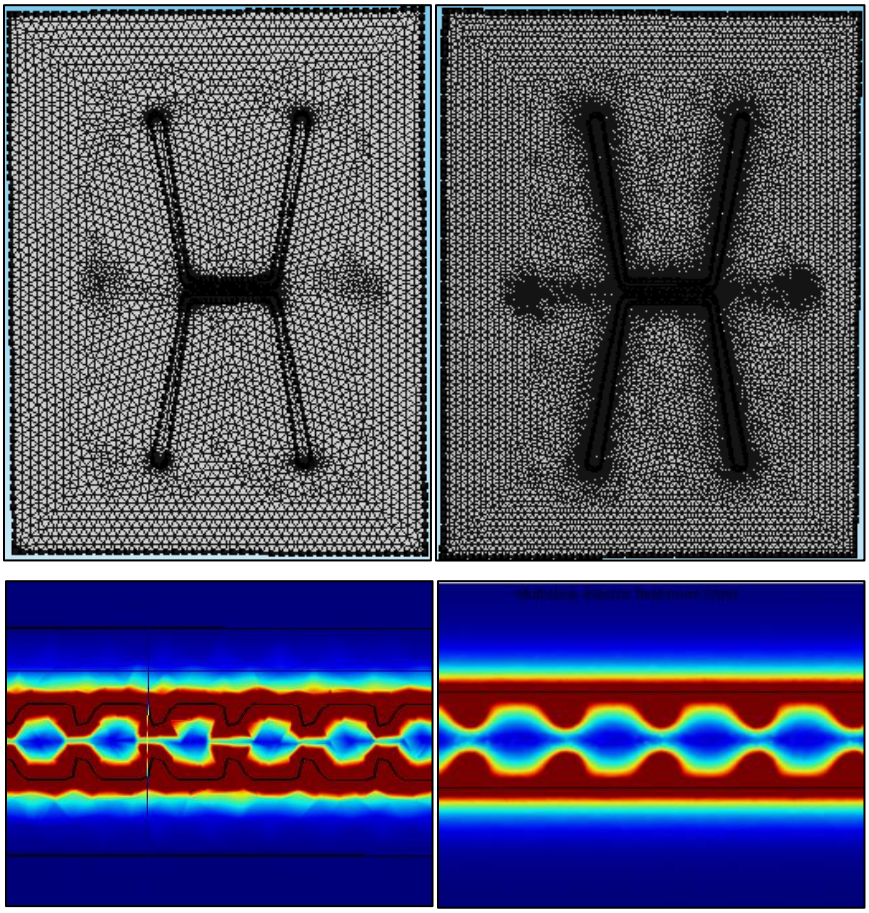

Figure 42: Top shows the mesh and bottom shows the electric field norm. Left shows the lower resolution mesh while right shows the mesh refined until there was less than a percent change in solution and produces smoother and more accurate results.

5.7 Validation of Electrodynamic Focusing Device

The above script was used to determine the efficacy of the electrodynamic focusing device that was modelled above. Mouse OP9 and DC cells were obtained and stained using Calcein-red/orange and Calcein-am respectively.

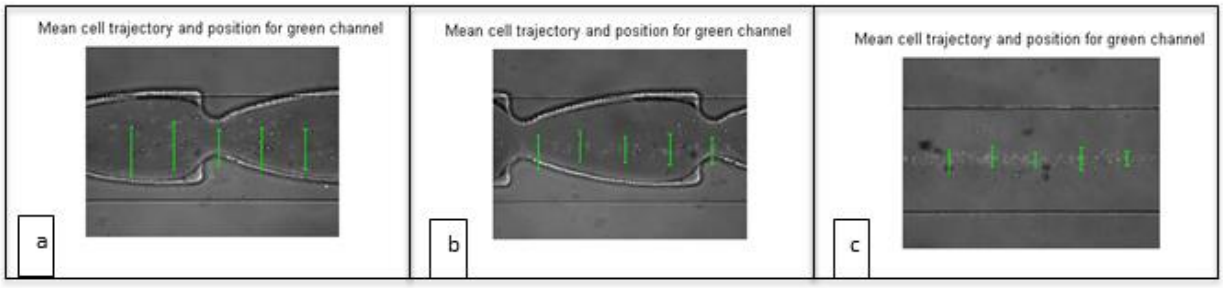

Figure 43: Mean positions in intervals across the microchannel are shown. (a) shows the results when 300VRMS at 300kHz was applied, (b) shows the results when 300VRMS at 600kHz was applied, and (c) shows the downstream results when 300VRMS at 600kHz was applied. Notice how the cells have been focused to the middle of the channel.

As the cells experience positive DEP force they are pushed to the center of the channel. Increasing the frequency tightened the band of cells. This is because at the higher frequency, 600 kHz, the CM factor is maximized and the full DEP force.

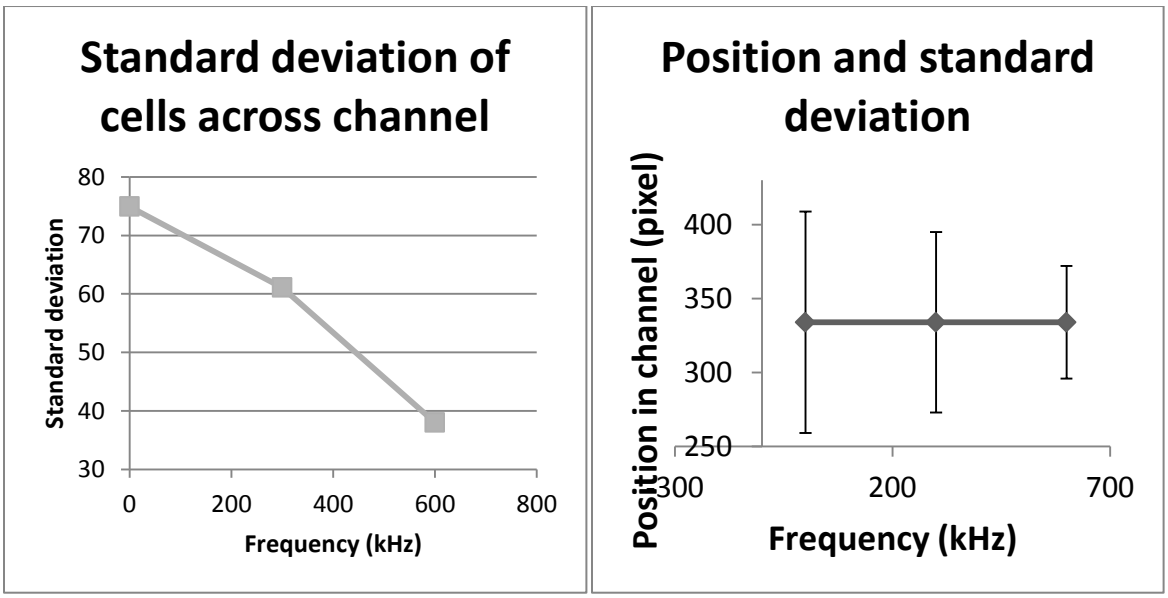

Figure 44: Left shows how the standard deviation decreased, meaning that the cells became more tightly focused, as the frequency was increased. Right shows the standard deviation over the mean cell position and also shows that the cells became more tightly focused as the frequency was increased. Both graphs show that as the frequency is increased the standard deviation of the cell positions in the channel decreased significantly.

As the frequency was increased the standard deviation of the cell positions in the channel has decreased significantly. The mean cell position and standard deviation become more focused as the frequency is increased to the apex of the CM curve. The standard deviation reduced by over half, 51.4%

meaning that the cells have been focused to the middle half of the channel. This outperformed the original goal of focusing cells to the middle 75% of the channel.

The validation of this device shows successful cell focusing using cDEP. This is the first such device using cDEP technology. With the addition of focusing for sample loading the cells can now be manipulated more efficiently and measurements will be more accurate. This can now be incorporated into other devices in lab to provide smart sample handling.

This chapter showed how the development of a new fabrication method opened up new area possibilities for device geometries. In addition to detailing the development of the new multilayer device fabrication method a new smart sample handling device design, one that had not been attempted before using cDEP, was introduced, modelled, and validated.

Chapter 6: Construction and Testing of a Bioinspired Micropump

6.1 Background on Significance and Bioinspiration of Micropumps

One of the largest challenges for lab-on-a-chip technologies are the supplemental tools such as micropumps, electronics, microscopes, etc. While the actual chip technology is, by definition, small and able to fit on a microscope slide the supplemental tools can be very large. This has led to the joke that the field is about developing "chip in a lab" technology rather than true "lab on a chip" (LOC) technology.

The goal of Lab-on-a-chip technology is to integrate all the functions of a normal sized laboratory on a system that is only a few centimeters in size. This would allow it to be used in all sorts of in-the-field applications where size is a limiting factor or in developing countries where the price of a full lab could be prohibitive. Typically these systems rely on microfluidic networks of channels for sample transport with typical dimensions between 10 and 100 μm. One of the biggest advancements, occurring in the 90's, was soft lithography which uses a silicon wafer as a "mold" for holding, and curing, PDMS. This allows for rapid fabrication and higher reliability while also producing bio-compatible devices [144].

In addition to the PDMS microchannels there can be many other elements incorporated onto the chip. It can include pumps, valves, sensors, and electronics that can be much more difficult to incorporate. [144]

One of the biggest challenges is the development of a microscale micropump. It is an area that has emerged as critical for driving the sample through the microfluidic environment while occupying a minimal sized footprint. Two areas in particular where micropumping is a critical element of the device is for polymerase chain reaction (PCR) and micro total analysis systems (μTAS) where a controlled sample flow is critical. Liquid cooling in microelectronic devices is another emerging area. [145]

There are several areas for micropump development. These can be broadly broken down into two main categories – mechanical displacement micropumps where oscillatory or rotational pressure applies a force to the fluid and causes it to move and electro-and magneto- kinetic micropumps where they provide direct energy transfer to manipulate the fluid. One such mechanical micropump is the diaphragm displacement pump. This design consists of a diaphragm like channel in the main channel that is made of a flexible material. The chamber will first expand with fluid which will increase the pressure in the diaphragm cavity. The outlet valve will then open and the diaphragm will compress, causing the pressure to decrease in the diaphragm which will then cause the inlet valve to open. This process is repeated for continual pumping. There are several methods for causing this expansion and compression of the diaphragm chamber. [145]

Electroactive polymers (EAP), polymers that change size or position when exposed to an electric field, are an expanding field and a new area for developments in micropumping. Recent achievements have shown the development of a microactuator built using ion implantation on either side of a polymer substrate to embed the electrically conductive outer layers [146], a thin film coated on each side with a compliant electrode material that when a voltage was applied had strains of greater than 100% [147], successful creation of an EAP pump with flow of 25 μL per hour but a complicated and time consuming fabrication process [148], and an EAP diaphragm with 550 μL per minute but also with an intensive fabrication process, [149].

From reading these papers it becomes obvious what the appeal of EAP micropumps is. They are effective and have a small footprint. However there is still the challenge of developing a reasonable fabrication method, particularly one conducive to mass fabrication processes that would allow for it to be commercializable. Following the work of [150] where they created a micropump using a thin PDMS membrane we will attempt to make a diaphragm based EAP micropump using PDMS as the thin

membrane and PDMS doped with carbon black as the electrode layers in our micropump design. Using PDMS as the bulk material will allow for the process to be inexpensive and repeatable.

Another area that is growing for micropump design is bioinspiration. One particular insect that is very efficient at pumping on the microscale is the female mosquito. Only in recent research efforts has the mechanism for this pumping been established. Mosquitos have two pumping organs located in their head. Kim, Kim et al. 2011 used micro-particle image velocimetry (PIV) and synchotron X-ray micro-imaging to relate the function of the two pumping regions. They were able to establish that the pumps used staggered timing, where the first pump starts to expand and then the second pump will start to expand, to create the desired pressure gradients in order to maximize pumping performance [151].

They found that in female mosquitos there were three phases to the pumping process. The first phase consisted of fluid being sucked into the first pump. Once the first pump has reached a crucial volume the second pump will start to expand. There is flow between the two pumps. In the third and final phase the volume of fluid is pushed toward the female mosquito's body by the second pump while the first pump closes, discharging the remaining fluid in both directions. By carefully staggering the two pumps the female mosquito is able to achieve maximal flow of fluid in one direction. We decided to use the female mosquito as the bioinspiration for our micropump device design due to its efficiency and effectiveness in nature [151].

6.2 Theory of a Microfluidic Pumping Device Based on Capacitive Plates

A Micropump with deformable geometry can be used to induce flow. This was accomplished by layering two conductive deformable thin films on either side of a thin deformable insulative layer. When an electric current is applied to the fixed electrodes the dielectric elastomeric plated are designed to buckle. We can model this system as a capacitive plate (adapted from [152]), where the capacitance C can be described as

$$\boldsymbol{C = \frac{\varepsilon A}{d}} \tag{62}$$

where ε is the permittivity of the dielectric, A is the surface area, and d is the dielectric distance or distance between the plates. The voltage V can be described as (adapted from [152])

$$\boldsymbol{V = \frac{Qd}{\varepsilon A}} \tag{63}$$

where Q is the charge. We can then describe the geometry of the bucking plates as (adapted from [152])

$$\boldsymbol{0 = \nabla^2\left(\nabla^2 w(r,\theta) - \frac{12e_r}{h_{t^2}} w(r,\theta)\right)} \tag{64}$$

where e_r is the radial compressive strain, h_{t^2} is the composite plate thickness, w is the plate deformation in the out-of-pane direction, r is the plate radius, and θ is the angle of deformation.

6.3 Micropump Design

The micropump was designed to buckle when a voltage was applied. This was accomplished by essentially building a capacitor. The micropump consists of two layers of a conductive polymer on either side of an insulative and non-compressible polymer. When a voltage is applied the plates, like in a parallel plate capacitor [153-155], are drawn toward each other. The incompressible material, because it cannot be compressed, must maintain the same volume so it expands. When both ends are fixed and the material is unable to expand horizontally the entire micropump assembly will buckle. When placed over a microchannel the micropump will buckle into the channel displacing fluid and inducing fluid flow. [152]

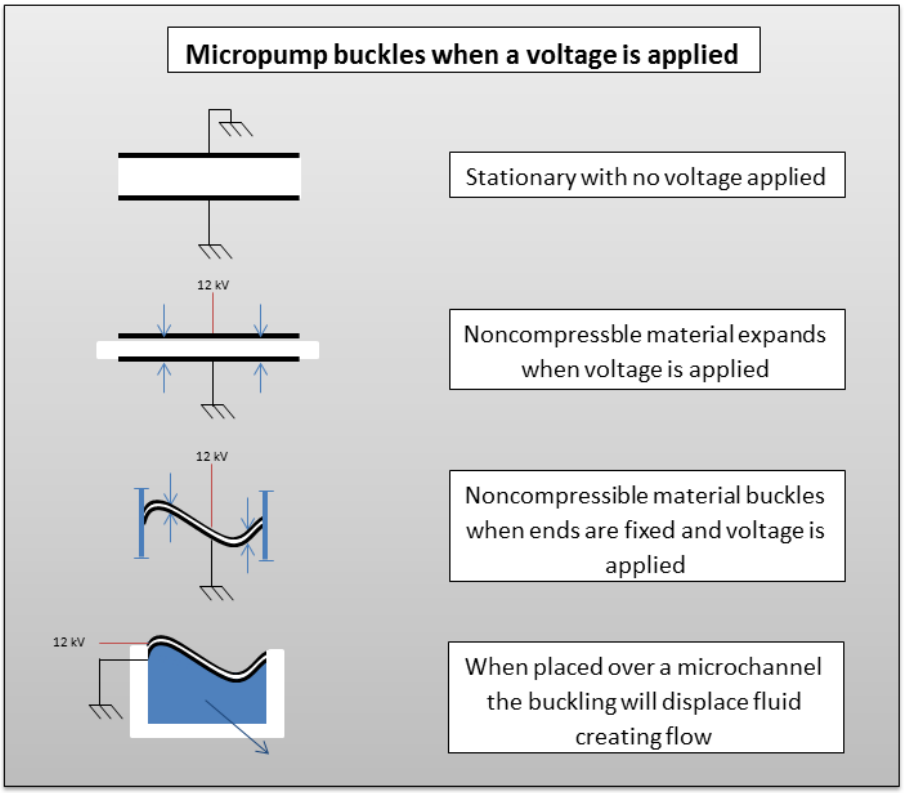

Figure 45: When both plates are attached to ground and no voltage is applied the entire system is stationary. When a voltage is applied and both ends are fixed the polymer will expand and the entire micropump will buckle. When this assembly is placed over a microchannel and a voltage is applied it will buckle into the channel displacing fluid and inducing fluid flow.

The challenge comes from fabricating materials that are very elastic and are therefore willing to deform. This requires the development of a process for creating thin elastic film sheets that are insulative and thin elastic film sheets that are conductive.

6.4 Micropump Fabrication

A process was developed and optimized in-house for doping PDMS in order to create the micropump. The two outside plates consist of conductive layers created by making carbon black slurry and mixing it with PDMS (Gelest) and applying it in layers on both sides of a thin insulating membrane made of non-conductive PDMS (Sylgard). PDMS was ordered from two different companies (Gelest and Sylgard) because it was found that in order to dope the PDMS the silicone particles in the PDMS needed to be very small and spread evenly throughout the mixture. Sylgard PDMS was found to produce a nonconductive PDMS when treated whereas the Gelest PDMS successfully produced a conductive end product.

The carbon black slurry is fabricated by following the following procedure:

1.) Mix 120 milligrams of 3 wt. % Carbon Black particles (Ketjenblack EC-600JD, AkzoNobel) in 40 milliliters of tetrahydrofuran (THF, Sigma-Aldrich).

2.) Sonicate solution for 1 hour using a tip-ultasonicator (VirSonic 100) or Bath Sonicator (FisherScientic). If tip-ultrasonicator is used, solution should be suspended in an ice-bath to prevent overheating.

3.) Transfer suspension to 3.8 grams of uncrosslinked PDMS (vinyl terminated PDMS with 9400 Da Molecular Weight, Gelest Inc.) that was preheated to 70°C.

4.) Continuously stir and heat solution for 4 hours at 70°C to allow the solvent (THF) to evaporate.

5.) Add 22 milligrams of catalyst (Tetrakis(dimethylsiloxy) silane, Gelest Inc.) and 99 milligrams of crosslinker (Platinum-Cyclovinylmethylsiloxane Complex, Gelest Inc.) to solution and manually mix for 10 minutes.

The slurry begins to harden very quickly and the remaining fabrication steps for making the micropump must be completed within 20 minutes.

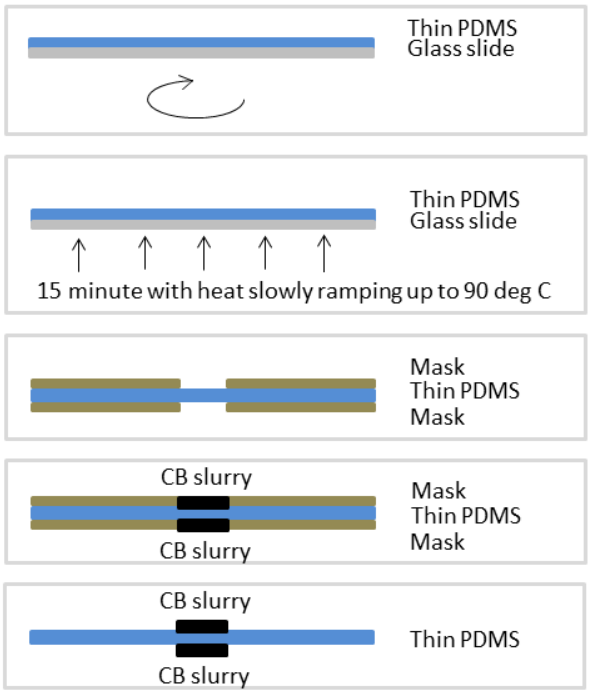

Figure 46: Fabrication procedure for using the carbon black slurry to create conductive layers on the thin PDMS insulating membrane.

6.5 Micropump Validation Experimental Procedures

Once the devices were fabricated they were validated using two different approaches. The first approach was to apply a voltage across the micropump only and observe the deformation of the membrane. The second approach consisted of bonding the micropump over a microchannel, flooding the channel with 7 micron in diameter fluorescent beads in order to visualize movement, applying a voltage in order to deform the membrane, and then observing the resultant flow. For both validation setups a script in Matlab was developed in order to quantify the results.

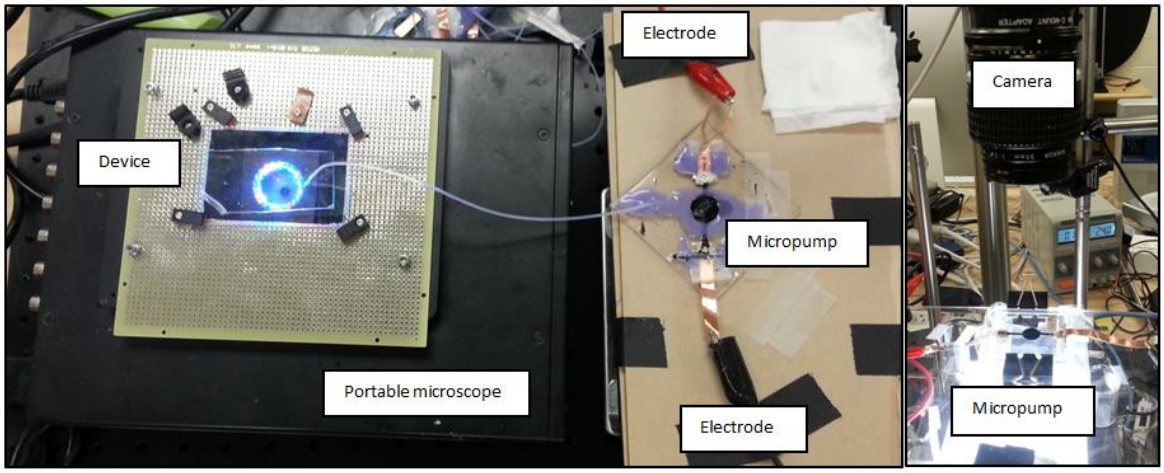

Figure 47: Image of experimental setup for measuring fluid flow on left showing the portable microscope that was used to record movement of fluorescent beads within a microchannel on the left with tubing connecting it to the micropump to the right which was connected to the electronics using the red and black wires shown. Right shows the experimental setup for imaging the expansion of the micropump.

A power supply was used to apply the voltage. A pre-existing script in LabView (National Instruments) was used to ramp the voltage from 0 up to the desired amount at a rate of 100 V/sec.

6.6 Data analysis Methods

A script was created in Matlab in order to quantify the expansion of the elastomer. It begins by reading in a frame in the image, calculating a threshold value, and converting the image to a black and white image. The percentage of the image that is covered in the elastomer is calculated by counting the number of black pixels and the number of white pixels in the image.

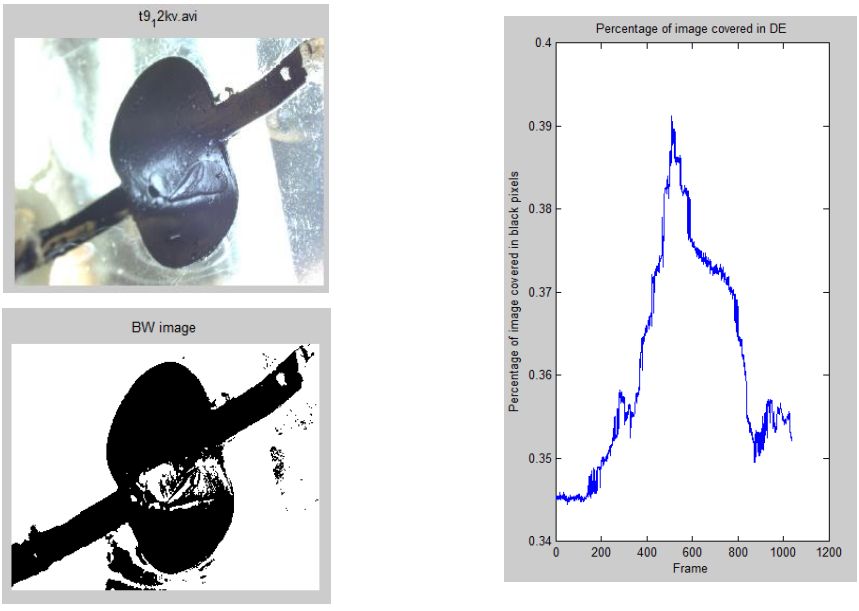

Figure 48: The micropump expanded as a voltage was applied, increasing in size by about 4.5% when increased from 0 V to 12 kV and then back to 0V. Top left shows an input frame, bottom left shows

the image converted to a black and white image after thresholding. Notice that there are some artifacts which contribute error. Right shows the percent area covered as voltage is turned on and ramped to a total of 12 kV at a rate of 100V/sec and then decreased at the same rate back to 0 V.

High resolution images with high contrast are required and the script is sensitive to the threshold level. With consistent lighting, however, artifacts from reflections or shadows are consistent.

6.7 Expansion of the Dielectric Membrane Upon Application of Voltage

The micropump was directly connected to the electronics and imaged as voltage was ramped up at a rate of 100V/sec. Initial electrical testing showed that significant deformation could be observed at 7kV and that the electrodes could withstand up to 14kV without being damaged.

Figure 49: The micropump buckles when voltage is applied. Left shows the micropump when no voltage is applied and there is no buckling. Right shows the amount of buckling that occurs when 12kV are applied.

The experiment was repeated 4 times with a peak expansion of 4.5% when 12 kV was applied on the micropump sample.

The percentage the electrodes covered the entire area being imaged was recorded and measured using a Matlab script developed for this purpose. The percentage of deformation depending upon the peak applied voltage with 12kV providing the greatest amount of deformation.

Table 10: Summary of results optimizing the voltage to apply to a specific sample in order to maximize membrane expansion.

Peak applied voltage (kV)	Starting covered area	Peak covered area	Ending covered area	Percent expansion
10	34.59%	36.52%	34.59%	1.93%
11	34.55%	37.5%	35.25%	2.95%
12	34.50%	39.0%	35.0%	4.5%
14	38.50%	41.2%	38.55%	2.7%

This validates the concept behind the micropump and shows that deformation occurs. It is worth noting that because much of the buckling occurs out of plane it is not images, so the actual expansion of the membrane is greater than what was measured observing only in-plane deformation.

6.8 Preliminary Fluid Flow Results From Bioinspired Micropumping System

In the second setup the micropump was bonded to a microchannel and attached, using Teflon tubing, to a separate microdevice that was flooded with 7 micron diameter fluorescent beads and imaged as a voltage was applied and the fluid membrane deformed using a portable microdevice. Another Matlab script was developed for tracking the fluorescent particles and calculating their velocity.

Table 11: Summary of results from placing pump directly over a microchannel and using it to induce flow. Results are summarized both as average and standard deviation pixels per second and microns per second.

Test	Start (0kV)	Max (5kV)	End (0kV)
1	0.0	0.4	0.0
2	0.0	0.5	0.1
3	0.0	0.3	0.0
4	0.0	0.5	-0.1
5	0.0	0.5	-0.1
Average (microns/sec)	0.00	0.71	-0.03
Stdev(microns/sec)	0.00	0.16	0.09

Originally a 5kV source was used to drive the pump. This was to visualize the minimum flow that could be achieved. Increasing the voltage increases the flow rate. At 5KV a velocity of .71 microns/sec was measured which is about 63.9 nL/hour. Increasing that just to 7KV resulted in a peak flow of 157.5 nL/hours. Driving a small volume of fluid, as demonstrated, is advantageous in such systems where there are small sample volumes, from a patient for example, or in areas where there is delivery of a small volume of a drug such as in implantable drug delivery systems [156].

The developed micropump fills in a much needed gap in achievable flow rate compared to the systems discussed above that were capable of driving 25 µL per hour [148], and 550 µL per minute [149]. Both had an intensive fabrication process whereas the newly developed micropump has a streamlined process that could easily be converted into a mass fabrication method.

This observable flow proves that electroactive polymers are a viable solution to construct on chip low sample volume micropumps.

Chapter 7: Discussion and Future Work

7.1 Conclusion

This work presented solutions to the main challenges faced by the cDEP platform for rare cell isolation. The main challenges were lack of a rigorous analysis script, need for a smart sample loading system that focuses particles initially in the channel, and a large footprint due to supplementary equipment needed to drive the chip. The solutions developed were a powerful analysis script that tracks and analyzes individual cells, a device that uses cDEP to focus cells into a narrow band for sample preloading, and the development of a micropump whose footprint fits on a single oversized glass slide. With these solutions the cDEP platform has been made more robust and new areas of research can be explored.

The capability to efficiently isolate a cell population will lead this technology to a commercial product. This research could lead to the development of personalized treatment plans for patients with cancer, greatly improving their chances at fighting off the disease. Identifying genotypic and phenotypic changes during treatment would allow for treatment monitoring and allow for corrections to the treatment plan when necessary.

7.2 Future Work

The analysis script, while accurate and robust, could be made less computationally intense by restricting analysis to a smaller window in the video and parallelizing the process. Additional morphology measurements would allow for a greater understanding of the relationship between the bioelectrical response of the cell and its actual biophysical properties. Implementation of an edgeless active contour algorithm would measure any surface protrusions, blebs, and other deformations in the cells surface that could affect analysis and behavior.

Improving the device design process so that the finite element analysis models are more accurate would allow for more rapid and targeted devices. Addition of the particle tracing module in Comsol would increase the accuracy of the models created during the device development process. It would increase model accuracy by not only predicting the movement path for a specific cell type but it would also allow for an animation of the path taken by individual particles. The development of clear graphics and animations would help in explaining and communicating how this phenomenon works and how it can be used as a tool.

More sensitive devices are critical to develop in order to maximize the response of cells in the electric field. With the new fabrication protocol, entirely new electrode geometries can be explored. Design areas such as the serpentine channel [116] and the trapezoidal electrode array [157] are now possible to explore due to the new multilayer fabrication system.

While a proof of concept has been demonstrated showing that the micropump is able to induce fluid flow, further work is necessary to bring it to a commercial product. Currently flow is induced when an electric field is applied as the pump deforms into the channel placed below it. When the field is turned off, however, and the pump returns to its original shape the liquid flows backward to the original starting location. Flow rectification needs to be designed into the device in order to restrict the fluid flow to one direction. In addition a method for continuous sample loading needs to be developed. The maximum and minimum flow rates achievable will also need to be established.

With the improved cDEP platform it will be possible to go back to the experimental studies and conclusively isolate TIC and drug resistant cell populations. The next step in isolating TIC's and MDR cells from cancer cell lines is to graft the cells isolated using our method into host animals to assess TIC properties and rigorously establish the properties of the subpopulation that we are able to isolate using our

technique. Once we have firmly connected the biophysical properties of the cells that we have isolated to their bioelectrical fingerprint we can move into patient studies where we use samples from patients to isolate TIC"s and determine what drug treatment plans would be best on an individual basis.

Appendix A: Matlab Code for Calculating Area Expansion of Micropump

```
%Lisa Anders
%BEMS Lab for calculating the percentage a black membrane expands in a video
%5-30-2014

clc;
clear all;
close all;

dire='C:\Users\leesah\Documents\Davalos Lab\EFRI-REM\Expanding pump\';

% whole folder analysis
filelist=dir(dire);

j = 0;

%For each video in the folder
for ii=1:length(filelist)

if strfind(filelist(ii).name,'.avi')>0

   j = j+1; %Increment counter

   obj = VideoReader(filelist(ii).name); %Declare video information (file name)

   disp('Starting reading video obj');
   ims = read(obj);
   nFrames = size(ims,4);

   disp('Finished reading video obj');

   i = 0;
```

```
clear x
clear y
figure,

%for k = 1: (round(nFrames/aFrames)):nFrames %1783 total frames, nFrames
for k = 1: 1 :nFrames %total frames nFrames
   i = i +1;       %initialize counter

   %Read kth image into im and plot
   im = read(obj, k);
   subplot(1,3,1), imshow(im), title(filelist(ii).name);

   %Let's convert to a BW image
   level = graythresh(im);
   BW = im2bw(im,level);
   subplot(1,3,2), imshow(BW), title('BW image')

   %Let's calculate number of black pixels versus white pixels and
   %plot percentage

   %Find all zero values - these are black pixels
   dummy = zeros(size(BW));
   dummy(BW==0) = 1;

   %Convert matrix to vector
   dummy = dummy(:);

   %Remove all zero values and count number of black pixels
   dummy(dummy==0) = [];
   size_dummy = size(dummy,1);
   percent = size_dummy/(size(BW,1) * size(BW,2));

   %Record this as x,y and plot
   y(i) = percent;
   x(i) = i;
```

```
            subplot(1,3,3), plot(x,y), title ('Percentage of image covered in DE'), xlabel('Frame'), ylabel('Percentage of image covered in black pixels')
            pause(.1)
        end

        disp('Video: done!');
    end
    end

    disp('analyze: done!');
```

References

1. Hanahan, D. and R.A. Weinberg, *The hallmarks of cancer.* cell, 2000. **100**(1): p. 57-70.
2. Hanahan, D. and R.A. Weinberg, *Hallmarks of cancer: the next generation.* Cell, 2011. **144**(5): p. 646-674.
3. Christiansen, J.J. and A.K. Rajasekaran, *Reassessing epithelial to mesenchymal transition as a prerequisite for carcinoma invasion and metastasis.* Cancer research, 2006. **66**(17): p. 8319-8326.
4. Gregory, P.A., et al., *The miR-200 family and miR-205 regulate epithelial to mesenchymal transition by targeting ZEB1 and SIP1.* Nature cell biology, 2008. **10**(5): p. 593-601.
5. Hennessy, B.T., et al., *Characterization of a naturally occurring breast cancer subset enriched in epithelial-to-mesenchymal transition and stem cell characteristics.* Cancer research, 2009. **69**(10): p. 4116-4124.
6. Liu, Y., *Epithelial to mesenchymal transition in renal fibrogenesis: pathologic significance, molecular mechanism, and therapeutic intervention.* Journal of the American Society of Nephrology, 2004. **15**(1): p. 1-12.
7. Talmadge, J.E. and I.J. Fidler, *AACR centennial series: the biology of cancer metastasis: historical perspective.* Cancer research, 2010. **70**(14): p. 5649-5669.
8. Adams, A.A., et al., *Highly efficient circulating tumor cell isolation from whole blood and label-free enumeration using polymer-based microfluidics with an integrated conductivity sensor.* Journal of the American Chemical Society, 2008. **130**(27): p. 8633-8641.
9. Reya, T., et al., *A role for Wnt signalling in self-renewal of haematopoietic stem cells.* Nature, 2003. **423**(6938): p. 409-414.
10. Wechsler-Reya, R.J. and M.P. Scott, *Control of neuronal precursor proliferation in the cerebellum by Sonic Hedgehog.* Neuron, 1999. **22**(1): p. 103-114.
11. Pardal, R., M.F. Clarke, and S.J. Morrison, *Applying the principles of stem-cell biology to cancer.* Nature Reviews Cancer, 2003. **3**(12): p. 895-902.
12. Siegel, R., D. Naishadham, and A. Jemal, *Cancer statistics, 2013.* CA: a cancer journal for clinicians, 2013. **63**(1): p. 11-30.
13. Reya, T., et al., *Stem cells, cancer, and cancer stem cells.* nature, 2001. **414**(6859): p. 105-111.
14. Reya, T., et al., *Stem cells, cancer, and cancer stem cells.* Nature, 2001. **414**: p. 105-111.
15. Wicha, M.S., S. Liu, and G. Dontu, *Cancer stem cells: an old idea--a paradigm shift.* Cancer Res, 2006. **66**(4): p. 1883-90; discussion 1895-6.
16. Kulkarni-Datar, K., et al., *Ovarian tumor initiating cell populations persist following paclitaxel and carboplatin chemotherapy treatment< i> in vivo</i>.* Cancer Letters, 2013.
17. Paterlini-Brechot, P. and N.L. Benali, *Circulating tumor cells (CTC) detection: clinical impact and future directions.* Cancer letters, 2007. **253**(2): p. 180-204.
18. Cristofanilli, M., et al., *Circulating tumor cells, disease progression, and survival in metastatic breast cancer.* New England Journal of Medicine, 2004. **351**(8): p. 781-791.
19. Cristofanilli, M., et al., *Circulating tumor cells: a novel prognostic factor for newly diagnosed metastatic breast cancer.* Journal of Clinical Oncology, 2005. **23**(7): p. 1420-1430.
20. Mocellin, S., et al., *The prognostic value of circulating tumor cells in patients with melanoma: a systematic review and meta-analysis.* Clinical cancer research, 2006. **12**(15): p. 4605-4613.
21. Szakács, G., et al., *Targeting multidrug resistance in cancer.* Nature Reviews Drug Discovery, 2006. **5**(3): p. 219-234.
22. Yan, Y., M. Björnmalm, and F. Caruso, *Particle Carriers for Combating Multidrug-Resistant Cancer.* ACS nano, 2013. **7**(11): p. 9512-9517.
23. Sano, M.B., J.L. Caldwell, and R.V. Davalos, *Modeling and development of a low frequency contactless dielectrophoresis (cDEP) platform to sort cancer cells from dilute whole blood samples.* Biosensors and Bioelectronics, 2011. **30**(1): p. 13-20.

24. Yu, C., et al., *ALDH activity indicates increased tumorigenic cells, but not cancer stem cells, in prostate cancer cell lines.* in vivo, 2011. **25**(1): p. 69-76.
25. Pethig, R., et al., *Dielectrophoresis: a review of applications for stem cell research.* BioMed Research International, 2010. **2010**.
26. Yu, S.-c., et al., *Isolation and characterization of cancer stem cells from a human glioblastoma cell line U87.* Cancer letters, 2008. **265**(1): p. 124-134.
27. Collins, A., et al., *Prospective identification of tumorigenic prostate cancer stem cells.* Cancer Res, 2005. **65**: p. 10946-10951.
28. Patrawala, L., et al., *Side population is enriched in tumorigenic, stem-like cancer cells, whereas ABCG2(+) and ABCG2(-) cancer cells are similarly tumorigenic.* Cancer Research, 2005. **65**(14): p. 6207-6219.
29. Patrawala, L., et al., *Hierarchical organization of prostate cancer cells in xenograft tumors: the CD44+alpha2beta1+ cell population is enriched in tumor-initiating cells.* Cancer Res, 2007. **67**(14): p. 6796-805.
30. Pohl, H.A. and H. Pohl, *Dielectrophoresis: the behavior of neutral matter in nonuniform electric fields*. 1978: Cambridge university press Cambridge.
31. Pohl, H., *Dielectrophoresis.* Cambridge University Press: Cambridge, 1978., 1978.
32. Pohl, H.A., *Some Effects of Nonuniform Fields on Dielectrics.* J. Appl. Phys. , 1958. **29**.
33. Gagnon, Z.R., *Cellular dielectrophoresis: applications to the characterization, manipulation, separation and patterning of cells.* Electrophoresis, 2011. **32**(18): p. 2466-2487.
34. Pethig, R., *Review article—dielectrophoresis: status of the theory, technology, and applications.* Biomicrofluidics, 2010. **4**(2): p. 022811.
35. Hughes, M.P., *Strategies for dielectrophoretic separation in laboratory-on-a-chip systems.* Electrophoresis, 2002. **23**(16): p. 2569-2582.
36. Yang, J., et al., *Cell separation on microfabricated electrodes using dielectrophoretic/gravitational field flow fractionation.* Analytical Chemistry, 1999. **71**(5): p. 911-918.
37. Martinez-Duarte, R., *Microfabrication technologies in dielectrophoresis applications—A review.* Electrophoresis, 2012. **33**(21): p. 3110-3132.
38. Jones, T.B., *Electromechanics of Particles*. 1995, USA: Cambridge University Press. 265.
39. Gascoyne, P.R.C. and J. Vykoukal, *Particle separation by dielectrophoresis.* Electrophoresis, 2002. **23**(13): p. 1973-1983.
40. Arnold, W.M. and U. Zimmermann, *Rotating-Field-Induced Rotation and Measurement of the Membrane Capacitance of Single Mesophyll-Cells of Avena-Sativa.* Zeitschrift Fur Naturforschung C-a Journal of Biosciences, 1982. **37**(10): p. 908-915.
41. Wang, X.B., et al., *A Unified Theory of Dielectrophoresis and Traveling-Wave Dielectrophoresis.* Journal of Physics D-Applied Physics, 1994. **27**(7): p. 1571-1574.
42. Arnold, W.M. and U. Zimmermann, *Electro-Rotation - Development of a Technique for Dielectric Measurements on Individual Cells and Particles.* Journal of Electrostatics, 1988. **21**(2-3): p. 151-191.
43. Dussaud, A., *Particle segregation in suspensions subject to high-gradient ac electric fields.* J Appl Phys, 2000. **88**: p. 5463-5473.
44. Pohl, H., *The Motion and Precipitation of Suspensoids in Divergent Electric Fields.* Appl Phys, 1951. **22**: p. 869-871.
45. Pohl, H., *Some Effects of Nonuniform Fields on Dielectrics.* Appl Phys, 1958. **29**: p. 1182-1188.
46. Pohl, H., *Dielectrophoresis*. 1978, Cambridge: Cambridge University Press.
47. Wong, P., *Electrokinetics in micro devices for biotechnology applications.* IEEE/ASME Transactions on Mechatronics, 2004. **9**: p. 366-376.
48. Cemazar, J., et al., *Dielectrophoretic field-flow microchamber for separation of biological cells based on their electrical properties.* NanoBioscience, IEEE Transactions on, 2011. **10**(1): p. 36-43.

49. Masuda, S., T. Itagaki, and M. Kosakada, *DETECTION OF EXTREMELY SMALL PARTICLES IN THE NANOMETER AND IONIC SIZE RANGE.* Ieee Transactions on Industry Applications, 1988. **24**(4): p. 740-744.
50. Cummings, E.B. and A.K. Singh, *Dielectrophoresis in microchips containing arrays of insulating posts: theoretical and experimental results.* Analytical Chemistry, 2003. **75**(18): p. 4724-4731.
51. Hawkins, B.G. and B.J. Kirby, *Electrothermal flow effects in insulating (electrodeless) dielectrophoresis systems.* Electrophoresis, 2010. **31**(22): p. 3622-3633.
52. Lu, Y.-s., et al., *Controllability of non-contact cell manipulation by image dielectrophoresis (iDEP).* Optical and Quantum Electronics, 2005. **37**(13-15): p. 1385-1395.
53. Salmanzadeh, A., et al., *Isolation of prostate tumor initiating cells (TICs) through their dielectrophoretic signature.* Lab on a Chip, 2012. **12**(1): p. 182-189.
54. Srivastava, S.K., A. Gencoglu, and A.R. Minerick, *DC insulator dielectrophoretic applications in microdevice technology: a review.* Analytical and bioanalytical chemistry, 2011. **399**(1): p. 301-321.
55. Gambari, R., et al., *Applications to cancer research of "lab-on-a-chip" devices based on dielectrophoresis (DEP).* Technology in Cancer Research & Treatment, 2003. **2**(1): p. 31-39.
56. Becker, F., et al., *The removal of human leukaemia cells from blood using interdigitated microelectrodes.* J. Phys. D: Appl. Phys, 1994. **27**: p. 2659-2662.
57. Gascoyne, P., et al., *Dielectrophoretic Separation of Cancer Cells from Blood.* IEEE Trans. Industry Applications, 1997. **33**: p. 670-678.
58. Huang, Y., et al., *Dielectrophoretic cell separation and gene expression profiling on microelectronic chip arrays.* Anal Chem, 2002. **74**: p. 3362-3371.
59. Cheng, J., et al., *Preparation and hybridization analysis of DNA/RNA from E. coli on microfabricated bioelectronic chips.* Nat Biotechnol, 1998. **16**: p. 541-546.
60. Stephens, M., et al., *The dielectrophoresis enrichment of CD34+ cells from peripheral blood stem cell harvests.* Bone Marrow TRansplant, 1996. **18**: p. 777-782.
61. Huang, Y., et al., *Introducing dielectrophoresis as a new force field for field-flow fractionation.* Biophys J, 1997. **73**: p. 1118-1129.
62. Kim, U.-J., et al., *Selection of mammalian cells based on their cell-cycle phase using dielectrophoresis.* Proc Natl Acad Sci, 2007. **104**: p. 20708-20712.
63. Flanagan, L.A., et al., *Unique dielectric properties distinguish stem cells and their differentiated progeny.* Stem Cells, 2008. **26**(3): p. 656-665.
64. Huang, Y., et al., *The removal of human breast cancer cells from hematopoietic CD34+ stem cells by dielectrophoretic field-flow-fractionation.* Journal of hematotherapy & stem cell research, 1999. **8**(5): p. 481-490.
65. Talary, M., et al., *Dielectrophoretic separation and enrichment of CD34+ cell subpopulation from bone marrow and peripheral blood stem cells.* Medical and Biological Engineering and Computing, 1995. **33**(2): p. 235-237.
66. Vykoukal, J., et al., *Enrichment of putative stem cells from adipose tissue using dielectrophoretic field-flow fractionation.* Lab on a Chip, 2008. **8**(8): p. 1386-1393.
67. Shafiee, H., et al., *Contactless dielectrophoresis: a new technique for cell manipulation.* Biomedical microdevices, 2009. **11**(5): p. 997-1006.
68. Shafiee, H., et al., *Selective isolation of live/dead cells using contactless dielectrophoresis (cDEP).* Lab on a Chip, 2010. **10**(4): p. 438-445.
69. Sano, M.B., et al., *Contactless dielectrophoretic spectroscopy: examination of the dielectric properties of cells found in blood.* Electrophoresis, 2011. **32**(22): p. 3164-3171.
70. Salmanzadeh, A., et al. *Isolation of rare cancer cells from blood cells using dielectrophoresis*. in *Engineering in Medicine and Biology Society (EMBC), 2012 Annual International Conference of the IEEE*. 2012. IEEE.

71. Salmanzadeh, A., et al. *Mixing Enhancement in Microfluidic Devices Using Contactless Dielectrophoresis (cDEP)*. in *ASME 2011 Summer Bioengineering Conference*. 2011. American Society of Mechanical Engineers.
72. Creekmore, A.L., et al., *Changes in gene expression and cellular architecture in an ovarian cancer progression model.* PloS one, 2011. **6**(3): p. e17676.
73. Roberts, P.C., et al., *Sequential molecular and cellular events during neoplastic progression: a mouse syngeneic ovarian cancer model.* Neoplasia (New York, NY), 2005. **7**(10): p. 944.
74. Salmanzadeh, A., et al., *Dielectrophoretic differentiation of mouse ovarian surface epithelial cells, macrophages, and fibroblasts using contactless dielectrophoresis.* Biomicrofluidics, 2012. **6**(2): p. 024104.
75. Salmanzadeh, A., et al., *Investigating dielectric properties of different stages of syngeneic murine ovarian cancer cells.* Biomicrofluidics, 2013. **7**(1): p. 011809.
76. Salmanzadeh, A., et al., *Sphingolipid metabolites modulate dielectric characteristics of cells in a mouse ovarian cancer progression model.* Integrative Biology, 2013. **5**(6): p. 843-852.
77. Zanetti, M. and N.R. Mahadevan, *Immune Surveillance from Chromosomal Chaos?* Science, 2012. **337**(6102): p. 1616-1617.
78. Chao, M.P., I.L. Weissman, and R. Majeti, *The CD47–SIRPα pathway in cancer immune evasion and potential therapeutic implications.* Current opinion in immunology, 2012. **24**(2): p. 225-232.
79. Chung, C., et al., *Dielectrophoretic characterisation of mammalian cells above 100 MHz.* Journal of Electrical Bioimpedance, 2011. **2**(1): p. 64-71.
80. Coley, H.M., et al., *Biophysical characterization of MDR breast cancer cell lines reveals the cytoplasm is critical in determining drug sensitivity.* Biochimica et Biophysica Acta (BBA)-General Subjects, 2007. **1770**(4): p. 601-608.
81. Labeed, F.H., et al., *Assessment of multidrug resistance reversal using dielectrophoresis and flow cytometry.* Biophysical journal, 2003. **85**(3): p. 2028-2034.
82. Labeed, F.H., et al., *Biophysical characteristics reveal neural stem cell differentiation potential.* PloS one, 2011. **6**(9): p. e25458.
83. Ye, X.-Q., et al., *Heterogeneity of mitochondrial membrane potential: a novel tool to isolate and identify cancer stem cells from a tumor mass?* Stem Cell Reviews and Reports, 2011. **7**(1): p. 153-160.
84. Bhagat, A.A.S., et al., *Pinched flow coupled shear-modulated inertial microfluidics for high-throughput rare blood cell separation.* Lab on a Chip, 2011. **11**(11): p. 1870-1878.
85. Książkiewicz, M., A. Markiewicz, and A.J. Żaczek, *Epithelial-mesenchymal transition: a hallmark in metastasis formation linking circulating tumor cells and cancer stem cells.* Pathobiology, 2012. **79**(4): p. 195-208.
86. Castellanos, A., et al., *Electrohydrodynamics and dielectrophoresis in microsystems: scaling laws.* Journal of Physics D: Applied Physics, 2003. **36**(20): p. 2584.
87. Becker, F.F., et al., *Separation of human breast cancer cells from blood by differential dielectric affinity.* Proceedings of the National Academy of Sciences, 1995. **92**(3): p. 860-864.
88. Jones, T.B. and T.B. Jones, *Electromechanics of particles*. 2005: Cambridge University Press.
89. Seger, U. and P. Renaud, *Electrical cell manipulation in microfluidic systems.* ÉCOLE POLYTECHNIQUE FÉDÉRALE DE LAUSANNE, 2006.
90. Elvington, E.A.S., *Contactless Dielectrophoresis towards Drug Screening and Microdevice Development for Cell Sorting*, 2013, Virginia Polytechnic Institute and State University.
91. Jones, T., *Dielectrophoretic force calculation.* Journal of Electrostatics, 1979. **6**(1): p. 69-82.
92. Wang, X., F.F. Becker, and P.R. Gascoyne, *The fractal dimension of cell membrane correlates with its capacitance: A new fractal single-shell model.* Chaos: An Interdisciplinary Journal of Nonlinear Science, 2010. **20**(4): p. 043133.
93. Wang, X.-B., et al., *Changes in Friend murine erythroleukaemia cell membranes during induced differentiation determined by electrorotation.* Biochimica et Biophysica Acta (BBA)-Biomembranes, 1994. **1193**(2): p. 330-344.

94. Asami, K., T. Hanai, and N. Koizumi, *Dielectric approach to suspensions of ellipsoidal particles covered with a shell in particular reference to biological cells.* Jpn. J. Appl. Phys, 1980. **19**: p. 359-365.
95. Morgan, H. and N.G. Green, *AC electrokinetics: colloids and nanoparticles*. 2003: Research Studies Press.
96. Salmanzadeh, A., et al., *Investigating dielectric properties of different stages of syngeneic murine ovarian cancer cells.* Biomicrofluidics, 2013. **7**: p. 011809.
97. Piccardi, M. *Background subtraction techniques: a review*. in *Systems, man and cybernetics, 2004 IEEE international conference on*. 2004. IEEE.
98. Bao, P., D. Zhang, and X. Wu, *Canny edge detection enhancement by scale multiplication.* Pattern Analysis and Machine Intelligence, IEEE Transactions on, 2005. **27**(9): p. 1485-1490.
99. Canny, J., *A computational approach to edge detection.* Pattern Analysis and Machine Intelligence, IEEE Transactions on, 1986(6): p. 679-698.
100. Canny, J.F., *Finding edges and lines in images.* Massachusetts Inst. of Tech. Report, 1983. **1**.
101. Ballard, D.H., *Generalizing the Hough transform to detect arbitrary shapes.* Pattern recognition, 1981. **13**(2): p. 111-122.
102. Illingworth, J. and J. Kittler, *A survey of the Hough transform.* Computer vision, graphics, and image processing, 1988. **44**(1): p. 87-116.
103. Hough, P.V., *Method and means for recognizing complex patterns.* US patent, 1962. **3**(069): p. 654.
104. Xu, C. and J.L. Prince. *Gradient vector flow: A new external force for snakes*. in *Computer Vision and Pattern Recognition, 1997. Proceedings., 1997 IEEE Computer Society Conference on*. 1997. IEEE.
105. Xu, C. and J.L. Prince, *Generalized gradient vector flow external forces for active contours.* Signal processing, 1998. **71**(2): p. 131-139.
106. Xu, C. and J.L. Prince, *Snakes, shapes, and gradient vector flow.* Image Processing, IEEE Transactions on, 1998. **7**(3): p. 359-369.
107. Zimmer, C., et al. *Improving active contours for segmentation and tracking of motile cells in videomicroscopy*. in *Pattern Recognition, 2002. Proceedings. 16th International Conference on*. 2002. IEEE.
108. Zimmer, C., et al., *Segmentation and tracking of migrating cells in videomicroscopy with parametric active contours: A tool for cell-based drug testing.* Medical Imaging, IEEE Transactions on, 2002. **21**(10): p. 1212-1221.
109. Forney Jr, G.D., *The viterbi algorithm.* Proceedings of the IEEE, 1973. **61**(3): p. 268-278.
110. Rong Li, X. and Y. Bar-Shalom, *Tracking in clutter with nearest neighbor filters: analysis and performance.* Aerospace and Electronic Systems, IEEE Transactions on, 1996. **32**(3): p. 995-1010.
111. Daum, F., *Multitarget-Multisensor Tracking: Principles and Techniques [Book Review]*. Aerospace and Electronic Systems Magazine, IEEE, 1996. **11**(2): p. 41.
112. Blackman, S.S., *Multiple-target tracking with radar applications.* Dedham, MA, Artech House, Inc., 1986, 463 p., 1986. **1**.
113. Welch, G. and G. Bishop, *An introduction to the Kalman filter*, 1995.
114. Salmanzadeh, A., et al., *Microfluidic mixing using contactless dielectrophoresis.* Electrophoresis, 2011. **32**(18): p. 2569-2578.
115. Chan, T.F., B.Y. Sandberg, and L.A. Vese, *Active contours without edges for vector-valued images.* Journal of Visual Communication and Image Representation, 2000. **11**(2): p. 130-141.
116. Zhu, J., et al., *DC dielectrophoretic focusing of particles in a serpentine microchannel.* Microfluidics and nanofluidics, 2009. **7**(6): p. 751-756.
117. Xuan, X., J. Zhu, and C. Church, *Particle focusing in microfluidic devices.* Microfluidics and nanofluidics, 2010. **9**(1): p. 1-16.

118. Huh, D., et al., *Microfluidics for flow cytometric analysis of cells and particles.* Physiological measurement, 2005. **26**(3): p. R73.
119. Pamme, N., *Continuous flow separations in microfluidic devices.* Lab on a Chip, 2007. **7**(12): p. 1644-1659.
120. Chung, T.D. and H.C. Kim, *Recent advances in miniaturized microfluidic flow cytometry for clinical use.* Electrophoresis, 2007. **28**(24): p. 4511-4520.
121. Chang, C.-C., Z.-X. Huang, and R.-J. Yang, *Three-dimensional hydrodynamic focusing in two-layer polydimethylsiloxane (PDMS) microchannels.* Journal of Micromechanics and Microengineering, 2007. **17**(8): p. 1479.
122. Lee, G.-B., et al., *The hydrodynamic focusing effect inside rectangular microchannels.* Journal of Micromechanics and Microengineering, 2006. **16**(5): p. 1024.
123. Simonnet, C. and A. Groisman, *High-throughput and high-resolution flow cytometry in molded microfluidic devices.* Analytical chemistry, 2006. **78**(16): p. 5653-5663.
124. Tsai, C.-H., H.-H. Hou, and L.-M. Fu, *An optimal three-dimensional focusing technique for micro-flow cytometers.* Microfluidics and nanofluidics, 2008. **5**(6): p. 827-836.
125. Fu, L.-M., R.-J. Yang, and G.-B. Lee, *Electrokinetic focusing injection methods on microfluidic devices.* Analytical chemistry, 2003. **75**(8): p. 1905-1910.
126. Kohlheyer, D., et al., *A microfluidic device for array patterning by perpendicular electrokinetic focusing.* Microfluidics and Nanofluidics, 2008. **4**(6): p. 557-564.
127. Xuan, X., S. Raghibizadeh, and D. Li, *Wall effects on electrophoretic motion of spherical polystyrene particles in a rectangular poly (dimethylsiloxane) microchannel.* Journal of colloid and interface science, 2006. **296**(2): p. 743-748.
128. Yang, R.-J., et al., *A new focusing model and switching approach for electrokinetic flow inside microchannels.* Journal of Micromechanics and Microengineering, 2005. **15**(11): p. 2141.
129. Cheng, I.-F., et al., *An integrated dielectrophoretic chip for continuous bioparticle filtering, focusing, sorting, trapping, and detecting.* Biomicrofluidics, 2007. **1**(2): p. 021503.
130. Yu, C., et al., *A three-dimensional dielectrophoretic particle focusing channel for microcytometry applications.* Microelectromechanical Systems, Journal of, 2005. **14**(3): p. 480-487.
131. Zhu, J. and X. Xuan, *Dielectrophoretic focusing of particles in a microchannel constriction using DC-biased AC flectric fields.* Electrophoresis, 2009. **30**(15): p. 2668-2675.
132. Kirby, B.J., *Micro-and nanoscale fluid mechanics: transport in microfluidic devices*. 2010: Cambridge University Press.
133. Beavers, G.S. and D.D. Joseph, *Boundary conditions at a naturally permeable wall.* Journal of fluid mechanics, 1967. **30**(01): p. 197-207.
134. Shafiee, H., J.L. Caldwell, and R.V. Davalos, *A Microfluidic System for Biological Particle Enrichment Using Contactless Dielectrophoresis.* Journal of the Association for Laboratory Automation, 2010. **15**(3): p. 224-232.
135. Lee, I.H. and D.W. Cho, *An investigation on photopolymer solidification considering laser irradiation energy in micro-stereolithography.* Microsystem Technologies, 2004. **10**(8-9): p. 592-598.
136. Bertsch, A., et al., *Microstereolithography: a review*, in *Symposim on Rapid Prototyping Technologies*2003: BOSTON, MASSACHUSETTS. p. 3-15.
137. Suryatal, B. and S. Deshmukh, *LCD based Micro–Stereolithography: A Novel Technique for Rapid Prototyping.*
138. Udroiu, R. and L.A. Mihail, *Experimental determination of surface roughness of parts obtained by rapid prototyping*, in *Proceedings of the 8th WSEAS International Conference on Circuits, systems, electronics, control \& signal processing*2009, World Scientific and Engineering Academy and Society (WSEAS): Puerto De La Cruz, Tenerife, Canary Islands, Spain. p. 283-286.
139. Wong, S.H., M.C.L. Ward, and C.W. Wharton, *Micro T-mixer as a rapid mixing micromixer.* Sensors and Actuators B: Chemical, 2004. **100**(3): p. 359-379.

140. Yi, M. and H.H. Bau, *The kinematics of bend-induced mixing in micro-conduits.* International Journal of Heat and Fluid Flow, 2003. **24**(5): p. 645-656.
141. Liu, R.H., et al., *Passive mixing in a three-dimensional serpentine microchannel.* Microelectromechanical Systems, Journal of, 2000. **9**(2): p. 190-197.
142. Hossain, S., et al., *Analysis and optimization of a micromixer with a modified Tesla structure.* Chemical Engineering Journal, 2010. **158**(2): p. 305-314.
143. Hong, C.-C., J.-W. Choi, and C.H. Ahn, *A novel in-plane passive microfluidic mixer with modified Tesla structures.* Lab on a Chip, 2004. **4**(2): p. 109-113.
144. Abgrall, P. and A. Gue, *Lab-on-chip technologies: making a microfluidic network and coupling it into a complete microsystem—a review.* Journal of Micromechanics and Microengineering, 2007. **17**(5): p. R15.
145. Iverson, B.D. and S.V. Garimella, *Recent advances in microscale pumping technologies: a review and evaluation.* Microfluidics and Nanofluidics, 2008. **5**(2): p. 145-174.
146. Dubois, P., et al., *Microactuators based on ion implanted dielectric electroactive polymer (EAP) membranes.* Sensors and actuators A: Physical, 2006. **130**: p. 147-154.
147. Pelrine, R., et al., *High-speed electrically actuated elastomers with strain greater than 100%.* Science, 2000. **287**(5454): p. 836-839.
148. Xia, F., S. Tadigadapa, and Q. Zhang, *Electroactive polymer based microfluidic pump.* Sensors and Actuators A: Physical, 2006. **125**(2): p. 346-352.
149. Xu, T.-B. and J. Su, *Development, characterization, and theoretical evaluation of electroactive polymer-based micropump diaphragm.* Sensors and Actuators A: Physical, 2005. **121**(1): p. 267-274.
150. Kim, J.H., et al., *Performance characteristics of a polypyrrole modified polydimethylsiloxane (PDMS) membrane based microfluidic pump.* Sensors and Actuators A: Physical, 2008. **148**(1): p. 239-244.
151. Kim, B.H., H.K. Kim, and S.J. Lee, *Experimental analysis of the blood-sucking mechanism of female mosquitoes.* The Journal of experimental biology, 2011. **214**(7): p. 1163-1169.
152. Holmes, D., et al., *Buckling of Dielectric Elastomeric Plates for Electrically Active Microfludic Pumps.* Bulletin of the American Physical Society, 2013. **58**.
153. Carlson, G. and B. Illman, *The circular disk parallel plate capacitor.* American Journal of Physics, 1994. **62**(12): p. 1099-1105.
154. Parker, G., *Electric field outside a parallel plate capacitor.* American Journal of Physics, 2002. **70**(5): p. 502-507.
155. Halliday, D., R. Resnick, and J. Walker, *Fundamentals of physics extended*. 2010: John Wiley & Sons.
156. Maillefer, D., et al. *A high-performance silicon micropump for an implantable drug delivery system*. in *Micro Electro Mechanical Systems, 1999. MEMS'99. Twelfth IEEE International Conference on*. 1999. IEEE.
157. Choi, S. and J.-K. Park, *Microfluidic system for dielectrophoretic separation based on a trapezoidal electrode array.* Lab on a Chip, 2005. **5**(10): p. 1161-1167.